Laser spectroscopy of localized quantum dot states interacting with electron reservoirs

Dissertation der Fakultät für Physik
der Ludwig-Maximilians-Universität München

vorgelegt von
Florian Seilmeier
München, Mai 2013

Erstgutachter: Prof. Dr. A. Högele
Zweitgutachter: Prof. Dr. J. Feldmann
Tag der mündlichen Prüfung: 03.07.2013

Zusammenfassung

Selbst-organisierte Quantenpunkte sind Nanoobjekte, die in eine GaAs-Matrix eingebettet sind. Sie stellen für Ladungsträger natürliche Potentialfallen dar und weisen aufgrund des räumlichen Einschlusspotentials quantisierte Zustände auf. In der vorliegenden Arbeit wurden Quantenpunkte in einer Feldeffekstruktur mittels elektrischem Feld manipuliert und in resonanter Laserspektroskopie studiert. Der Schwerpunkt der Arbeit lag auf der Untersuchung von Wechselwirkungen lokalisierter Quantenpunktzustände mit benachbarten Ladungs- oder Spinreservoirs. Dazu wurden die experimentellen Bedingungen derart eingestellt, dass einzelne Quantenpunkte entweder für Ladungsträgerfluktuationen oder für Reservoirs sensitiv waren.

In der für gewöhnlich in externen elektrischen Feldern linearen Dispersionsrelation eines ladungsneutralen Quantenpunktes wurden eine Reihe von Sprüngen beobachtet. Als Grund für diese Sprünge wurden Ladungsfluktuationen von Fremdatomen in der Kristallmatrix identifiziert. Bei charakteristischen Bedingungen führen Ladungs- und Entladungsereignisse zu einer abrupten Änderung der elektrostatischen Umgebung, die sich in einer Energieverschiebung der optischen Resonanz manifestiert. Für die quantitative Analyse der Ladungsfluktuationen und ihrer Signaturen wurde ein elektrostatisches Modell entwickelt. Mittels einer umfassenden Studie nahe beieinander liegender Quantenpunkte auf Basis des erarbeiteten Modells konnten die relativen räumlichen Positionen von Quantenpunkten und Fremdatomen bestimmt werden. Im Gegensatz zu früheren Arbeiten deuten die Ergebnisse darauf hin, dass Fremdatome als Volumendefekt in der Matrix die Hauptquelle für Ladungsfluktuationen sind.

In der Dispersion des neutralen Exzitons wurde ein Knick mit kontinuierlicher Energieverschiebung mittels resonanter Laserspektroskopie beobachtet. Dieser Knick war charakteristisch für das Regime schwacher Tunnelkopplung zwischen dem Quantenpunkt und dem zwei-dimensionalen Elektronenreservoir. Die Tunnelkopplung wechselwirkender Zustände führt durch Hybridisierung zur Ausbildung neuer Superpositionszustände. Dadurch kommt es zu einer Renormalisierung der Energie des optischen Überganges, die den Knick in der Dispersion bedingt. Ein auf dem Anderson-Fano-Modell basierendes Hybridisierungsmodell mit quantitativer Übereinstimmung mit den experimentellen Beobachtungen wurde dazu verwendet die Kopplungsstärke zwischen Reservoir und lokalisierten Zustand zu bestimmen. Der Hybridisierungseffekt konnte ebenfalls auf dem geladenen Exziton nachgewiesen werden.

Für die Untersuchung optischer Signaturen von Vielteilcheneffekten wurde ein Aufbau für sub-Kelvin-Laserspektroskopie realisiert und mit optischen Studien an Quantenpunkten im Pauli-Blockade Regime charakterisiert. Die experimentell bestimmte und theoretisch berechnete Besetzung der elektronischen Spinzustände in Abhängigkeit von Magnetfeld und Temperatur wurde benutzt, um die Temperatur des Elektronenbades zu bestimmen. Das Experiment erlaubte den Zugriff auf alle Parameter außer der Badtemperatur und mit den optischen Blochgleichungen wurde die Besetzung der Spinzustände unter Berücksichtigung aller relevanten externen Parameter errechnet. Die Analyse der Besetzung im Magnetfeld mit der Spinbadtemperatur als freiem Parameter ergab eine Temperatur von 380 mK, die nicht ganz der nominellen Basistemperatur von 250 mK entspricht. Damit wurde gezeigt, dass der Aufbau für subK-Laserspektroskopie für die geforderten Temperaturen erfolgreich implementiert wurde.

Abstract

Self-assembled InGaAs quantum dots are nano-objects embedded in the solid-state matrix of GaAs. They act as natural potential traps for charge carriers and feature a number of quantized states due to the quantum confinement. When incorporated in a field effect structure the quantum dot states can be conveniently manipulated with an electric field and probed by resonant laser spectroscopy. In this thesis self-assembled quantum dots were investigated with an emphasis on the study of interactions between localized quantum dot states and charge or spin reservoirs in the environment. Experimentally the quantum dots were addressed in distinct regimes where the quantum dot spectrum was sensitive to individual charge fluctuations or mesoscopic reservoirs.

The fundamental transition of a neutral quantum dot was found to exhibit a number of discontinuities in the usually linear dispersion of the exciton energy in external electrostatic fields. The discontinuities were identified to arise from charge fluctuations in the surrounding crystalline matrix in which impurity atoms can capture or release electrons. At characteristic conditions charging and discharging events lead to discrete changes of the electrostatic environment which in turn gives rise to an energy shift of the optical resonance condition. An electrostatic model was developed for a quantitative analysis of charging events and their signatures. On the basis of the model a comprehensive study of nearby quantum dots allowed to map out the relative spatial positions of quantum dots and impurities. In contrast to previous reports our results provide evidence for bulk impurities as the main source of charge fluctuations.

By means of resonant laser spectroscopy in the energy dispersion of the neutral exciton a kink with a continuous energy shift has been observed which only occurs close to the regime where an electron is tunneling between the quantum dot and a 2D electron reservoir. The tunneling induces a weak coupling between the localized electron state of the quantum dot and the continuum of states in the reservoir. The tunnel coupling between the interacting states leads to hybridization into a new superposition state. In consequence the energy of the transition is renormalized which explains the kink in the energy dispersion. The hybridization model based on an Anderson-Fano approach quantitatively agrees with the experimental data and allows to extract the coupling strength between the reservoir and the localized state. In addition to the neutral exciton hybridization effects were also observed on the charged exciton.

To study optical signatures of many-body effects sub-K laser spectroscopy was established and the setup performance was characterized with optical studies of a quantum dot in the Pauli-blockade regime. The electron bath temperature was determined using experimental and calculated electron spin populations as a function of magnetic field and temperature. The experiment provided quantitative access to all parameters except the electron bath temperature. With the optical Bloch equations the electron spin populations were modeled taking into account all relevant external parameters. An analysis of the evolution of the spin population in magnetic fields with the electron bath temperature as the only free fitting parameter was performed. An electron bath temperature of 380 mK was derived being slightly offset to the nominal base temperature of 250 mK. This proves the successful implementation of the sub-K laser spectroscopy setup.

Contents

Chapter 1

Introduction

Semiconductor devices are part of our every day life. They are used in electronic equipment like computers, cell phones, optoelectronic devices etc. The demand for faster, smaller and more efficient devices for commercial applications drives the current research and development. With more and more technological progress the exploitation of classical effects becomes more difficult. Therefore the current research starts to explore quantum effects for technical applications.
One method to improve the performance of semiconductor devices with a quantum effect is to reduce spatial degrees of freedom of charge carriers. This means electrons and holes are trapped in a defined area. The ultimate device, which can be obtained by reducing the dimensions, are 0D-structures i.e. they are confined in all spatial directions. The concept of such a device was presented in 1982 by Arakawa et al. [1]. As these structures have typically sizes in the nano-scale regime classical models are not sufficient any more to explain the properties. Quantum mechanics determines now the physical properties which offers a large variety of new effects that can be explored and exploited for fundamental research and for new commercial applications.
One prominent example of zero-dimensional nano-structures are self-assembled InGaAs quantum dots which are the device of choice in this thesis. The growth of self-assembled InGaAs quantum dots has been pioneered in Pierre Petroff's group in 1993 [2, 3, 4]. Self-assembly or self-organization allows to create structures which have sizes that are not directly accessible by conventional nano-fabrication techniques. As quantum dots are self-organized structures they do not have exactly defined sizes and geometries. Nonetheless the quantum dot properties follow a distribution which can be modified by tuning the growth parameters. Different groups are also working on methods to achieve a higher yield of quantum dots with defined location and sizes [5]. With increasing control over the fabrication of quantum dots the application in commercial products becomes more and more interesting. Since the early 90s quantum dots have become an important material system for studies

in fundamental physics and are employed as quantum dot lasers [6, 7], optical amplifiers [8], single photon sources [9, 10]and flash memories [11].
MBE-grown quantum dots are embedded in a semiconductor matrix. This matrix is not perfectly pure and hosts defects [12, 13] and unwanted doping atoms [14]. Additionally for the application of an electric field a quasi-metallic back contact with a reservoir of free electrons is integrated in the sample. All these electronic states close to the quantum dot can interact with it.
The optical resonance of an interacting quantum dot is strongly affected by fluctuations in the solid state material [15]. Random jumps in the quantum dot signal have been observed by several groups [16, 17, 18]. In self-assembled InGaAs quantum dots the linewidths are in the range of 2 - 3 μeV although their spontaneous recombination rate is in the sub-μeV range [19]. Spectral fluctuations induced by fluctuations in the host material are one reason for the linewidth broadening. The main sources are nuclear spins [20] and charges [21, 22]. The strong sensitivity on the environment is an disadvantage for experiments where strongly isolated and unperturbed systems are necessary as it is required for spin state preparation [23, 24] and readout [25]. On the other hand it offers an opportunity to exploit the electric field sensitivity as a charge detection technique [26, 27]. In this case the quantum dot is coupled via the Coulomb interaction to electronic states which acquire charges by tunneling.
Coupling a many-body system to localized states in a quantum dot is another working regime. For electric-field-tunable samples a two-dimensional reservoir with free electrons is established in the back contact. The exchange of charges through a barrier is mediated by tunneling and for spin flips cotunneling is responsible [28, 29]. It has been demonstrated that in quantum dot-Fermi reservoir hybrid systems, whose interaction is in the strong coupling regime, many-body phenomena can be studied. Dalgarno et al. shows that in the quantum dot ground state the single electron state is hybridized with the continuum states of the Fermi reservoir [30]. Likewise the Mahan exciton forms between a hole in the quantum dot and an electron which has tunneled into the Fermi reservoir [31]. These two experiments have been performed at 4.2 K so that the coupling between the reservoir states and the localized state can still be treated as perturbations. At mK temperatures the signal strength of many-body effects increases as the correlations of the Fermi electrons with the localized quantum dot states are not destroyed by thermal fluctuations. In that case the quantum dot acts as a local scattering site comparable to the magnetic impurity in the classic Kondo effect in metals [32]. Therefore in quantum dot systems Fermi edge singularity has recently been demonstrated [33, 34] and if the spin is addressed the regime of the Kondo effect has been achieved [35, 36, 37].
Within this context the present work concentrates on how the electronic environment of the quantum dot affects its optical response. Practical applications as a sensor for charges and temperature are also discussed. Different interaction regimes encompassing Coulomb, tunneling and cotunneling interactions are investigated. The reservoirs participating in the interactions range from impurities with single charges to highly doped quantum wells that form reservoirs for free electrons. Three topics

are treated here. The thesis is organized in the following way.
In chapter 2 fundamental properties of quantum dots are presented. The growth and the preparation in the clean room is introduced and the general structure of the quantum dot samples. The concepts of excitons, confinement in semiconductors, optical selection rules and the properties of quantum dots in electric and magnetic fields are discussed briefly. For all experiments differential transmission spectroscopy is used in combination with different cryostat systems. The experimental techniques and the setup are described and explained in chapter 3. In the chapter 4 the Coulomb blockade model is presented which allows to extract important parameters like the confinement energies or the interaction energies. The optical Bloch equations deal with a two-level system in an electric field and can be applied onto quantum dot exciton transitions. With this model the optical contrast and the linewidth as well as the power dependance of a quantum dot can be derived.
Electronic states of impurities in the solid state matrix surrounding the quantum dot can be occupied or unoccupied. Depending on the type of electronic state the impurity is then charged or electrically neutral. If the charging occurs the local electric field at the quantum dot changes which can be detected in form of an energy shift of the resonance. In chapter 5 several quantum dots are analyzed and it is demonstrated that their characteristic exciton dispersions are affected by charging events.
In chapter 6 hybridization effects in the neutral and charged exciton are investigated. The coupling between the electron continuum of states in the back contact and the quantum dot requires that the excited state (ground state) of the neutral exciton (charged exciton) is substituted by a superposition of the electron state of the quantum dot with the Fermi sea of electrons. This results into an energy shift of the optical resonance. An Anderson model based simulation confirms the physical picture.
Quantum dot spectroscopy is usually performed at 4.2 K. If the temperature is lowered to the mK-regime the absorption contrast of a charged exciton shows in magnetic fields a spin-splitting which is covered by thermal effects at higher temperatures. In chapter 7 a technique is presented with which the bath temperature of the sample can be measured. For this the optical Bloch equations need to be applied onto a four-level system and the results of simulation and experiment are compared.

List of Publications

- K. Kowalik-Seidl, X. P. Vögele, F. Seilmeier, D. Schuh, W. Wegscheider, A. W. Holleitner, and J. P. Kotthaus. Forming and confining of dipolar excitons by quantizing magnetic fields. *Phys. Rev. B* **83**, 081307 (2011).

- F. Seilmeier, M. Hauck, A. Badolato, P. M. Petroff, and A. Högele. Residual dopants as sources of charge fluctuations identified with resonant spectroscopy of individual InGaAs quantum dots. in preparation.

- F. Seilmeier, E. Schubert, G. J. Schinner, A. Badolato, P. M. Petroff, and A. Högele. Temperature dependence of spin state preparation in a negatively charged quantum dot under resonant excitaton. in preparation.

Chapter 2

Self-assembled quantum dots

Self-assembly of semiconductor materials is a standard method to grow quantum dots. Colloidal quantum dots are spherical nanocrystals in a solution. They are in most cases compounds of II-VI-semiconductors and can consist of a single core or have a core-shell structure. Examples for this type of quantum dots are CdTe nanocrystals [38]. Another type of quantum dots are epitaxially grown samples with III-V-semiconductor compositions. The most commonly used and extensively investigated species are InAs-based semiconductor compounds. By adjusting the temperature and concentrations of the ingredients the optical and electronic properties of these crystals can be tailored. In this thesis self-assembled InGaAs quantum dots were studied. The InGaAs quantum dots were embedded in a field effect device. Therefore the optical response of the quantum dot is tunable by means of an external electric field.

2.1 InGaAs quantum dots

Self-assembled InGaAs quantum dots were grown with molecular beam epitaxy (MBE) on GaAs. The employment of MBE growth allows to deposit single atomic layers of semiconductor materials on a substrate [39]. The different semiconductors components which are supposed to form the sample are in effusion cells. The substrate is mounted rotatably above the cells in a ultra-high vacuum. The effusion cells are heated and thus the single semiconductors settle on the substrate forming chemical bonds. Interdiffusion and surface diffusion leads to energetically favorable configurations of the resulting compound [2]. An alternative technique to grow semiconductor quantum dots is metal-organic chemical vapour deposition (MOCVD) which is not relevant in the context of this thesis [39].
The growth of InAs quantum dots in the Stranski-Krastanov mode [40] is carried out layer by layer on GaAs. Below a critical thickness of 1.5 monolayers of InAs a thin

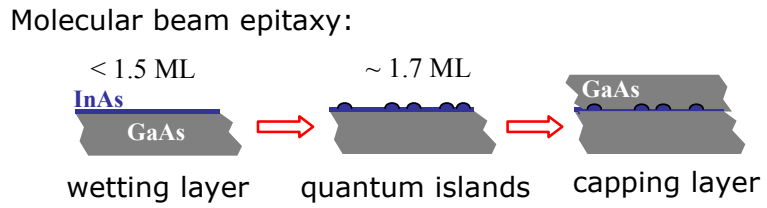

Figure 2.1: *Stranski-Krastanov growth mode of self-assembled InGaAs quantum dots. Due to strain the 2D-growth of InAs below* 1.5 *monolayers is substituted by the formation of quantum islands. The growth is stopped by depositing a GaAs capping layer on top.*

film is deposited on the substrate. This film is called wetting layer. In the range of 1.5 to 1.7 lens-shaped quantum dots are formed on the wetting layer which are free of defects. The reason for the formation of quantum dots is the lattice mismatch between the different semiconductor compounds. GaAs has a lattice constant of 5.65 Å and InAs has one of 6.06 Å respectively [41]. If InAs grows on GaAs it starts with the same lattice constant as GaAs and with every layer the interatomic distance conforms to the actual value. Therefore strain plays an important role in the thin wetting layer and to relax the system (lowering the overall free energy) quantum dots and eventually dislocations (if growth is not interrupted) evolve. Further deposition of InAs leads to dislocations and defects as well as a merging of quantum dots eventually resulting in an InAs film. To obtain single quantum dots the growth is stopped as long as there are only defect-free InAs islands and a GaAs capping layer is grown on top. This capping layer prevents further chemical reactions and increases the distance between surface states and dots (Fig. 2.1).
In Fig. 2.2 an atomic force micrograph (AFM) of several quantum dots is shown. The height can be up to 10 nm and the mean diameter is $20 - 30$ nm [42]. The density of dots on a sample is in the range of 10^9 to $10^{11}\,\mathrm{cm}^{-2}$ and one dot consists of 10^4 to 10^5 atoms [2]. From AFM measurements like in Fig. 2.2 it is known that InAs-quantum dots are lens-shaped. Their spectral emission is above 1000 nm [2] which is inconvenient as standard silicon photodetectors have a low efficiency in this wavelength regime. An annealing step after the growth of the quantum dots can change their size and structure [4]. The heating of the sample leads to diffusion of indium which migrates into the surrounding GaAs. This process creates partially covered islands with a volcano-like structure [43, 31]. Due to this the size is changed and therefore the emission energy can be tuned below 1000 nm. The heating causes diffusion of both indium and gallium. Therefore the composition of the quantum dot changes from InAs to InGaAs as gallium diffuses into the island.
The quantum dots form a spatial confinement potential for electrons and holes as the available states within the island are lower in energy than the band gap of the surrounding GaAs.

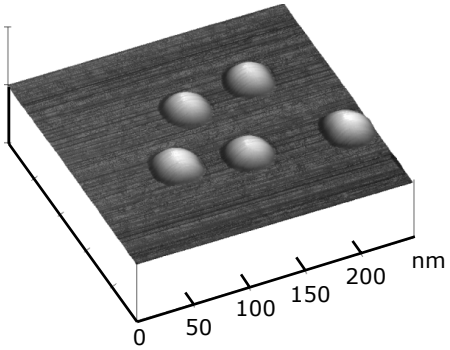

Figure 2.2: *Atomic force micrograph of a quantum dot sample. InGaAs quantum dots have typical diameters of* 30 nm *and heights of* 5 nm.

2.2 Field effect structure

The samples employed in this thesis consist of a heterostructure of different semiconductor materials. The quantum dot layer is embedded in a field effect structure to allow the application of an electric field [3]. The general structure of all samples is identical (see Fig. 2.3). The thicknesses of blocking barriers and the kind of doping in the back contact were each adapted to the experimental requirements.
The growth of the heterostructure starts with a single crystalline GaAs substrate which is several μm thick. On the substrate a highly n-doped GaAs-layer (also called back contact) is deposited in which the excess electrons are delivered by silicon atoms substituting gallium atoms. The typical free electron density is $4 * 10^{18}\,\mathrm{cm}^{-2}$. A tunnel barrier consisting of undoped GaAs separates the InGaAs layer with the quantum dots from the back contact. The quantum dots are followed by a a GaAs capping layer and a very thick AlAs/GaAs superlattice which is supposed to prevent any current through the structure. A 14 nm GaAs capping layer is grown on top of the semiconductor heterostructure. This is necessary as GaAs is more stable at ambient conditions than AlAs. On top of the semiconductor a Ni/Cr metal gate is deposited. To achieve an Ohmic contact to the back contact indium has been diffused into the heterostructure opening a metallic channel to the surface.
In Fig. 2.3 the band structure with the Fermi level is depicted. The Fermi energy $E_F = 0$ is defined by the electron occupation in the back contact due to Fermi level pinning. Any voltage applied between back contact and top gate tilts the band structure (in all experiments the back contact is grounded). However if no voltage is applied the structure is still tilted due to the internal bias voltage caused by the metal on top of the sample. At a metal-semiconductor interface a Schottky barrier forms due to the equilibration of charge carriers [41]. Therefore a Schottky voltage V_S needs to be applied to bring the heterostructure into flat-band configuration. In good approximation it can be assumed that the voltage drops linearly over the sample and the energy change due to a change in externally applied voltage can be

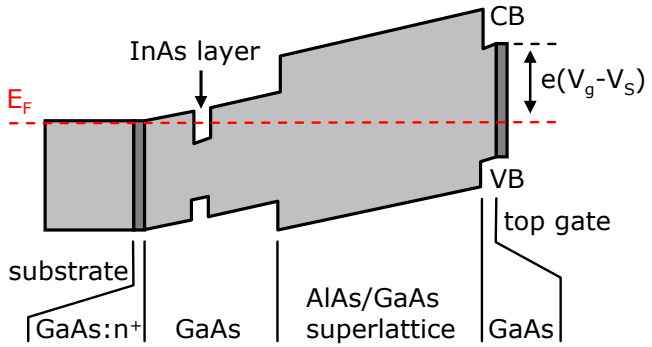

Figure 2.3: *General structure of the quantum dot samples. The quantum dot layer is embedded in a field effect structure which is modeled as a capacitor with a metallic top gate and a highly-doped back contact. An AlAs/GaAs superlattice prevents vertical currents flowing through the sample and a GaAs tunneling barrier between back contact and InAs layer suppresses also tunneling of electrons.*

calculated as

$$E_\lambda(V_g) = e(V_S + V_g)\lambda. \tag{2.1}$$

The lever arm λ is given by the distance from top gate to back contact divided by the thickness of the tunnel barrier. By changing the gate voltage it is possible to tune the energy of the quantum dot [44].
Three samples were used for the experiments presented in chapters 5 to 7. Only the important barrier thicknesses and types of the Fermi reservoir are listed here: MCV1-7 has a tunnel barrier with 25 nm and the capping layer at the quantum dots is 30 nm. The lever arm is $\lambda = 7$. MCV13-2 has a modulation-doped back contact (i.e. the ionized donors and the donor electrons are spatially separated by 10 nm). The tunnel barrier is 25 nm, the quantum dot capping layer is 30 nm and the lever arm is 12. MCV10-5 is identical to MCV1-7 except that the capping layer on the quantum dots is only 10 nm thick instead of 30 nm. Thus λ is 12. MCV1-7 is used for the hybridization experiments (chapter 6) and for the charge sensing project (chapter 5), data from MCV13-2 are shown in chapter 5.4 and Fig. 7.3 and chapter 7 is based on MCV10-5.

2.3 Electronic and optical properties of quantum dots

Quantum dots are quantum islands consisting of InAs with a certain admixture of gallium atoms. The gallium content influences the the energy spectrum of the

dot substantially as the band gap of the semiconductor compound moves towards the typical GaAs band gap with increasing number of Ga atoms. Also the local distribution of Ga and In within the quantum dot influences the properties. Holes are strongly trapped at the apex of the quantum dot as the indium concentration is higher there [45]. The electron wave function is spread over the whole quantum dot.
Optical excitations of the quantum dot create electron-hole pairs by absorption of photons. As the electron and hole have opposite charges they attract each other via the Coulomb interaction. This leads to a bound state of the electron-hole pair meaning the energy of the system is lowered by the binding energy. A Coulomb-bound electron-hole pair is called an exciton with typical binding energies in the meV-range.
In this chapter basic properties of InGaAs quantum dots are discussed. The spatial confinement of quantum dots is such that it becomes a zero-dimensional system which fundamentally changes the optical and electrical response of the system. A discrete energy spectrum evolves similar to atomic systems. The behavior in electric and magnetic field is presented as it is used in the following chapters.

2.3.1 Confinement and energy spectrum

The confinement of electrons and holes in the quantum dot is based on the fact that InAs has a smaller band gap than GaAs. The confinement along the growth axis depends on the height of the quantum dot (see Fig. 2.3) and increases/ decreases the energies of the electron/ hole states. The confinement energy E_c^z can be approximated as a quantum well and is in the range of several hundred meV. The confinement in x-y plane can be described mathematically as a spherical harmonic potential. Its energy is in the range of tens of meV. The combination of both contributions from the confinement and the smaller InAs band gap gives the overall confinement energy of electron and hole in a quantum dot. As the energies arising from the vertical confinement are fairly large there is only one confined level in a quantum dot. Therefore it is sufficient to consider only the harmonic potential for the experiments. Fig. 2.4(a) depicts the model of a self-assembled quantum dot. In a harmonic potential $V = 1/2m\omega^2 r^2$ with radial distance r the levels are equidistant in energy with $\Delta E = \hbar\omega$. For this potential an analytical solution can be derived for the wave functions and energies [46, 47].
The different levels of the quantum dot are called s-, p-, d-orbitals similar to atoms. The filling of these states by means of laser excitation can be directly observed in photoluminescence experiments [48, 49]. If several electrons and holes occupy states in the quantum dot the electron-hole, electron-electron and hole-hole interaction contribute to the overall energy of the quantum dot states. By changing the energies of the different states relative to the Fermi energy with an external electric field (chapter 2.2) it is also possible to load additional electrons or holes into the dot,

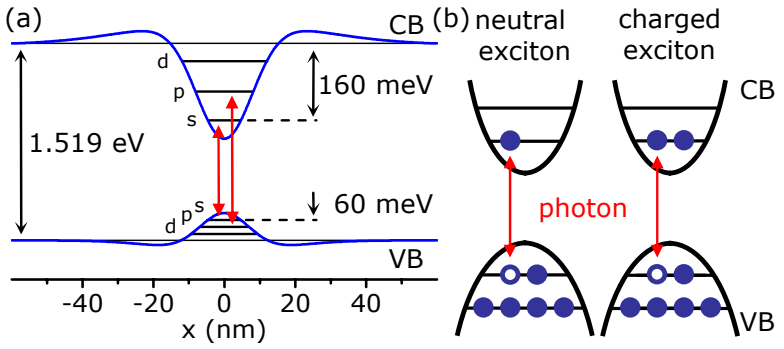

Figure 2.4: *(a) Semiconductor band structure at the position of a quantum dot. The in-plane confinement potential is spherical and accordingly forms a discrete energy spectrum with equidistant level spacings. The lowest levels are called s-, p- and d-levels. The optical selection rules only allow s-s-transitions , p-p-transitions, etc. (b) Simplified harmonic model of a quantum dot with the fundamental excitations: neutral (left hand side) and singly charged (right hand side) exciton.*

so that the number of electrons and holes in the quantum dot is not equal. The Hamiltonian of the system taking into account all interactions between the charges can be written according to [49] as:

$$H_{int} = \sum_i E_c^e c_i^\dagger c_i + E_c^h d_i^\dagger d_i - \sum_{ijkl} E_{eh} c_i^\dagger d_j^\dagger d_k c_l \qquad (2.2)$$
$$+ \frac{1}{2} \sum_{ijkl} E_{ee} c_i^\dagger c_j^\dagger c_k c_l + \frac{1}{2} \sum_{ijkl} E_{hh} d_i^\dagger d_j^\dagger d_k d_l$$

E_c^e and E_c^h are the energies of the electrons and holes including also the confinement energies arising from their vertical and lateral spatial confinement. $c_i^\dagger$/ c_i and $d_i^\dagger$/ d_i are the respective creation/ annihilation operators for electrons and holes. E_{eh}, E_{ee} and E_{hh} are the interaction energies.
In Fig. 2.4(b) simplified quantum dot potentials are depicted. The easiest case of excitation in the system is the generation of an electron-hole pair known as an exciton (left case). If one electron is already resident in the quantum dot a photon creates a charged exciton state, which is in this case singly negative (right case) but can be in principle negative or positive with several excess charges [44].

2.3.2 Optical transitions in a quantum dot

Self-assembled quantum dots have discrete energy levels with a finite density of states. With each state a spin- or angular momentum is associated (in the following pseudospin or spin). The electron states of the s-level have spin $\pm 1/2$ depending

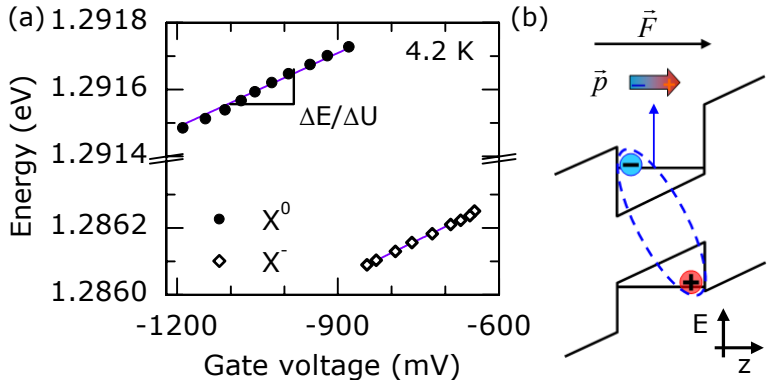

Figure 2.5: *Plateaus of the neutral exciton X^0 and the charged exciton X^- at 4.2 K. The slope is given by the Stark effect $\Delta E/\Delta U$. The extent of the plateaus and the energy spacing between X^0 and X^- are given by the interaction energies of the electrons and holes residing in the quantum dot. (b) Quantum confined Stark effect: the external electric field tilts the band structure and pulls apart the electron and hole leading to a polarization parallel to the electric field. The Stark shift is given by the dipole moment $\vec{p}$ and the electric field $\cdot\vec{F}$.*

on whether they have spin ↑ or ↓. The four p-states in the conduction band have total pseudospin (z-projections) of $J_z = \pm 3/2$ and $J_z = \pm 1/2$. Optical excitations occur at momenta $k \approx 0$ [50]. The normally degenerate heavy-hole and light-hole bands are split due to the strain in the system [51]. The heavy-hole band has a pseudospin of $J_z = \pm 3/2$ and is higher in energy than the light-hole band with $J_z = \pm 1/2$. Therefore only the heavy-hole states contribute to optical excitations. A photon has a pseudospin of $J_z = 1$ so that first order optical transitions in the dipole approximation require a change in angular momentum of $|\Delta J_z| = 1$. In the case of the neutral exciton (Fig. 2.4(b) left diagram) the electrons have $J_z = \pm 1/2$ and the holes have $J_z = \pm 3/2$. In principle four transitions exist with $\Delta J_z = \pm 1$ and $\Delta J_z = \pm 2$. As the photon provides only $\Delta J_z = \pm 1$ the $\Delta J_z = \pm 2$ transitions are optically not active (dark states). For the case of a charged exciton (Fig. 2.4(b) right diagram) the transition takes place between a single electron state with $J_z = \pm 1/2$ and the exciton state with $J_z = \pm 3/2$ (the two electrons in the exciton state form a singlet with $J_z = 0$ so that only the hole contributes its angular momentum).
The exciton binding energy is smaller than the confinement energy. Due to this fact the Coulomb interactions can be treated as perturbations. Therefore the overlap of the electron and hole wave function $|\langle\Psi_e|\Psi_h\rangle|^2$ determines the oscillator strength of the transition and also the radiative lifetime of a quantum dot exciton. Typical lifetimes of excitons are of the order of 1 ns and below [30].
In Fig. 2.5(a) the plateaus of the neutral exciton X^0 and of the charged exciton X^- are depicted. They are measured on a single quantum dot at 4.2 K and are about 5.4 meV apart from each other in energy which stems from the sum of the different

interaction energies E_{eh}, E_{ee} and E_{hh}.
The plateaus in the graph in Fig. 2.5(a) shift almost linearly in energy. This behavior is a consequence of the quantum confined Stark effect of the exciton. The exciton is an electron-hole pair localized in the quantum dot. Fig. 2.5(b) illustrates the situation in the dot. Perpendicular to the quantum dot plane an electric field is applied which pulls apart the oppositely charged electron and hole. Due to the strong confinement they are trapped but nonetheless the wavefunction center of masses of the electron and hole are spatially separated. By this a dipole moment $\vec{p}$ is created which interacts with the external electric field. The electric field also induces a polarization $\beta\vec{F}^2$ (β is the polarizability) leading to a second-order term in the electric field. The overall energy of the quantum dot exciton in the external electric field is:

$$E = E_0 - \vec{p}\cdot\vec{F} + \beta|\vec{F}|^2 \tag{2.3}$$

E_0 is the energy without electric fields. The first-order term dominates as can be seen in the graph. Typically values for the dipole moments are $|\vec{p}| = e \times 0.25\,\text{nm}$ to $e \times 2.5\,\text{nm}$ and the polarizability ranges from $\beta = 0.25\,\mu\text{eV}/(\text{kV/cm})^2$ to $3\,\mu\text{eV}/(\text{kV/cm})^2$ [45]. The Stark shift is typically $\Delta E/\Delta U = 1\,\mu\text{eV/mV}$.

2.3.3 Fine structure and magnetic fields

In this chapter two properties of excitons are presented as they are explicitly used in the course of the experiments in chapters 5 to 7. The fine structure splitting of the neutral exciton is well-known and is caused by the electron-hole exchange interaction. The magnetic field dependence is discussed for the charged exciton as it is exploited in the last chapter.

Fine structure of the neutral exciton

Ideally quantum dots are lens-shaped and have a perfect rotational symmetry. In this case the bright excitons ($J_z = \pm 1$) and the dark excitons ($J_z = \pm 2$) are split by an energy $\Delta \approx 150\,\mu\text{eV}$ [52]. If the rotational symmetry is broken the bright excitons show a fine structure splitting into two resonances as it is depicted in Fig. 2.6(a) [52, 53]. Depending on the ellipticity of the quantum dot the fine structure splitting is between $0\,\mu\text{eV}$ and $50\,\mu\text{eV}$ [54]. The exchange interaction Hamiltonian is [55]:

$$H_{ex} = 2\Delta J_z S_z + \Delta_1(J_x S_x - J_y S_y) + \Delta_2(J_x S_x + J_y S_y) \tag{2.4}$$

For the bright exciton states the electron spin and the hole spin are opposite to each other and for the dark states they have the same orientation. The first term

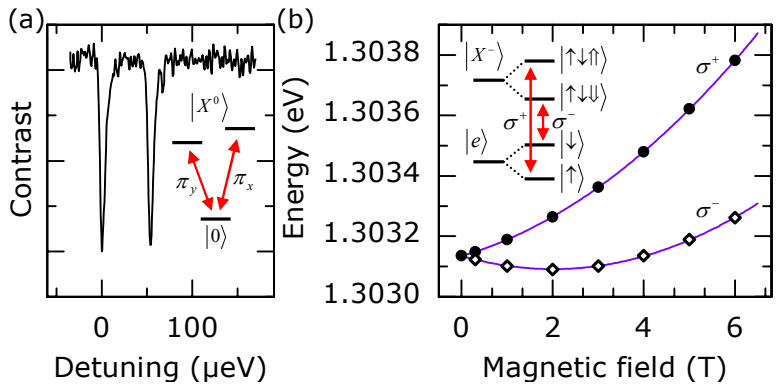

Figure 2.6: *(a) Fine structure splitting of the neutral exciton. The two resonances can be addressed independently with linearly polarized light. This happens due to the geometric asymmetry of the quantum dot lifting the degeneracy of the the two bright exciton states (compare inset) and requiring a new basis consisting of the superposition of the pure states. (b) Magnetic field dependance of the charged exciton. The exciton and ground states split each into two levels with different angular momenta (inset). This Zeeman splitting and the diamagnetic shift lead to parabolic curves of the resonance energies in magnetic fields.*

in equation 2.4 accounts for the z-projections of the electron and hole spins. Due to their different orientations of the spins bright and dark states are split by Δ. The second term splits the bright states by Δ_1 and the third term removes the degeneracy of the dark states. Δ_1 is zero if the quantum dot has rotational symmetry. The Hamiltonian mixes the bright states so that a new basis of eigenfunctions has to be chosen for the case of elliptic quantum dots [56]: $|B_1\rangle = 1/\sqrt{2}(|+1\rangle + |-1\rangle)$ and $|B_2\rangle = 1/\sqrt{2}(|+1\rangle - |-1\rangle)$ ($|+1\rangle$ and $|-1\rangle$ are the eigenstates of the perfectly symmetric system). The inset in Fig. 2.6(a) shows the new bright exciton system with the states $|B_1\rangle$ and $|B_2\rangle$ split by the fine structure constant Δ_1. Due to the new basis the polarization of the transitions has changed from circularly to linearly polarized light.

Charged exciton in a magnetic field

A singly charged exciton consists of two electrons and one hole and the ground state is a single electron state. Both the ground and the excited states are degenerate in absence of a magnetic field as depicted in the inset in Fig. 2.6(b). In a finite magnetic field (in Faraday geometry/ B-field parallel to the growth axis) the degeneracy is lifted and the X^--system consists of four energetically different states. Only two optical transitions are possible as the change of the pseudospin must be ± 1. Transitions from $|\uparrow\rangle$ ($J_z = 1/2$) to $|\uparrow\downarrow, \Uparrow\rangle$ ($J_z = 3/2$) with σ^+-light and from

$|\downarrow\rangle$ ($J_z = -1/2$) to $|\uparrow\downarrow, \Downarrow\rangle$ ($J_z = -3/2$) with σ^--light are possible. The splitting is governed by the Zeeman energy $E_Z = g\mu_B B$ with the g-factor of the electron or hole and Bohr's magneton μ_B [56, 29]. The Zeeman term of the electron causes the ground state splitting and the term of the hole causes the splitting of the exciton state.
In Fig. 2.6(b) resonance energies of the X^- at different magnetic fields is shown. For the fit the exciton g-factor $g_X = g_e + g_h$ needs to be used, so one cannot directly extract the electron and hole g-factors from the fit. Another effect quadratic in B also contributes to the energy as is depicted in Fig. 2.6(b). This is the diamagnetic shift [57]. The overall energy of a quantum dot in a magnetic field can be written as [57]:

$$E = E_0 \pm \frac{1}{2} g_X \mu_B B + \alpha B^2 \tag{2.5}$$

The diamagnetic interaction includes the wave functions of the initial and final states and the coefficient can be rewritten as $\alpha = e^2/8(l_e^2/m_e + l_h^2/m_h)$ with $l_{e/h}$ being the extent of the wave functions. As l_h is much smaller than l_e and m_h is much larger than m_e α is approximately $(e^2 l_e^2)/(8m_e)$ so that the size of the electron wave function can be calculated.

Chapter 3

Experimental setup

In the present thesis single self-assembled quantum dots were studied at temperatures between 4.2 K and 250 mK by means of photoluminescence (PL) and differential transmission (DT) spectroscopy. A confocal microscope has been used which has a high spatial resolution to access single dots. In order to achieve low temperatures the confocal microscope is operated in a helium bath cryostat or in a ^{3}He-system.
Two versions of confocal microscopes for low-temperature applications are available: In a free-space microscope the incoming light is sent through an optical window into the tube where it is focused on the sample by an objective. A fiber-based confocal microscope uses glass fibers to direct the light to the objective. All experiments in chapters 6 and 5 were performed with a free-space confocal microscope in a helium bath cryostat. The experiments in chapter 7 were carried out with a ^{3}He-system which was modified into a fiber-based confocal microscope by Georg Schinner [58]. In both systems magnetic fields up to 9 T are available provided by superconducting magnets.
Photoluminescence spectroscopy allows easy access to elementary excitations of a quantum dot. Therefore this technique is mainly used as a supporting method to find quantum dots and to supplement experimental data obtained with differential transmission spectroscopy. Contrarily to PL, differential transmission uses resonant excitation of the investigated transition and offers a spectral resolution on the order of the laser linewidth. Transmission spectroscopy was applied to quantum dots for the first time by Alen et al. [59] in 2003. Most of the data presented in this work has been obtained with DT.

3.1 Confocal microscopy

In ordinary optical microscopy structures with sizes of 10 μm can be resolved in the ocular [60]. By means of a trick the spatial resolution can be increased substantially.

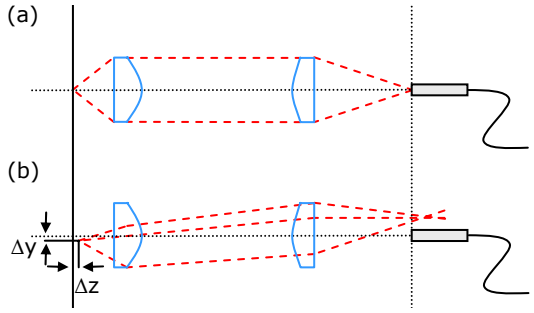

Figure 3.1: *Confocal principle adapted to a fiber-based microscope. The two lenses form the objective and the fiber acts as a pin hole since its core is only* $5.6\,\mu$m *in diameter. (a) Light leaving the fiber is directed to the focal spot of the objective. (b) Light originating from areas other than the focal spot are not mapped onto the core of the fiber. So a spatial image can only be obtained by moving the sample relative to the focal spot.*

This is the confocal principle introduced in 1955 [61]. In Fig. 3.1(a) a schematic shows the functionality of a confocal microscope. It requires a pin-hole from which the light has to pass, an ocular and an objective. In the case of a fiber-based microscope the single-mode fiber acts as a pin-hole with a diameter of $5.6\,\mu$m (size of the core of the fiber). The NA of the fibers optimized for operation at 850 nm is 0.12. The light from the fiber ideally fully illuminates the objective lens which focus the light onto the sample positioned in the focal plane of the objective. This optical setup has two advantages: Firstly the light is focused on the sample, which is necessary to obtain sufficient excitation powers. Secondly light emerging from areas which are not in focus are effectively suppressed. This fact is depicted in Fig. 3.1(b). Any light source shifted by Δz along the optical axis, in-plane (Δy or Δx) or both is not collected in the core of the fiber after having passed the two objective lenses. The image focal point on the side of the fiber is shifted for example by $f^2/\Delta z$ with $f = (1/f_1 + 1/f_2 - d/(f_1 f_2))^{-1}$ (d is the distance between objective and ocular lens) in the case of a deviation of Δz. On the contrary light from the focal point is always refocused on the fiber ending. As only one point is accessible by the confocal microscope the system demands to scan the sample relatively to the objective to obtain a 2D-image of the sample surface.
The spatial resolution is defined by the spot size of the focused laser beam which has an almost Gaussian profile [62]. According to [63, 64] the diffraction limited spot size of a focused Gaussian beam is approximately $1.22\lambda/(2NA)$ with the numerical aperture $NA = n\,sin\alpha$ (n is the refractive index and α is the half of the angle of the light cone). This formula requires that the objective lens is fully illuminated. In case that the lens is only partially illuminated a correction factor K is introduced [65]: $d_{spot} = K\lambda/(2NA)$. The resolution can be measured by means of a SiO_2-sample with a metallic checkered pattern. Underneath the pattern a transmission detector is mounted. Scanning over the chessboard leads to a smeared out Heaviside

function whose derivative has peaks to negative and positive values for falling and rising slopes (compare [66]). The width of these Gaussian functions corresponds to the spot size as it images how the focal spot moves over a metallic edge.

3.1.1 Free-space microscope

The design of a low-temperature free-space confocal microscope is well-established as a tool for quantum dot spectroscopy (as can be seen in [46, 67]) and is commercially available from *Attocube Systems*. The microscope used for this work has been originally a fiber-based version which was configurated as a free-space version in the course of this work. The microscope can be separated in two parts. The optical head, which is the upper part at room temperature (Fig. 3.2), allows to control and manipulate the laser light which is sent through the optical window in the second part is located in a vacuum tube at liquid helium temperature of 4.2 K. A schematics of the free-space confocal microscope is depicted in Fig. 3.2(a).
The optical head (upper part Fig. 3.2(a)) consists of two beam sampler (BS) *BSF05-B1* from *Thorlabs* with a maximum reflection of 10 % and a minimum transmission of 90 % depending on the wavelength. At each beam sampler one fiber coupling unit is attached consisting of a lens collimating the laser light which exits from the fiber and a fiber coupler from *Thorlabs*. The fiber coupling unit at the upper BS (top arm) has a *Geltech C280TM-B* lens with an $NA = 0.15$ and the one at the lower BS (side arm) uses a *Geltech C220TM-B* ($NA = 0.25$). The lens design is optimized in such a way that the *NA*s match the glass fibers. The microscope is adjusted for maximum performance of the top arm at 960 nm (laser beam perpendicular to the sample and focused) and the side arm is adjusted for 850 nm light and such that the laser beam lies perfectly on the beam from the top arm and is also focused onto the sample. In the side arm a bandpass filter (*Thorlabs FB850-10*) is mounted to suppress light other than 850 ± 5 nm. At the upper BS a CCD-camera is attached to check the image quality of the focal spot. With the photodetector at the lower BS linear polarization can be chosen for the light hitting the optical window. Underneath the two BSs a switchable half-wave plate and a switchable quarter-wave plate are installed which allow to define any polarization desired.
The low temperature part of the microscope is in a vacuum tube and contains the aspheric objective lense (*Geltech C330TM-B*) with an $NA = 0.68$ (Fig. 3.2(a)). The working distance of the objective is 1.68 mm and the focal length is 3.1 mm. The objective is 116 cm apart from the optical window. The collimated laser beam from the top arm is focused on the sample underneath. The sample is glued onto a chip carrier and mounted on the transmission detector (*Siemens BPW34*) and low temperature piezo positioner with slip stick mode [68] for x, y and z (*Attocube*). The spatial resolution in the system is measured to be 1.0 μm according to the procedure described in chapter 3.1. In Fig. 3.2(b) a photograph of the sample with detector, positioner and objective is shown. The transmission laser is focused onto the plane

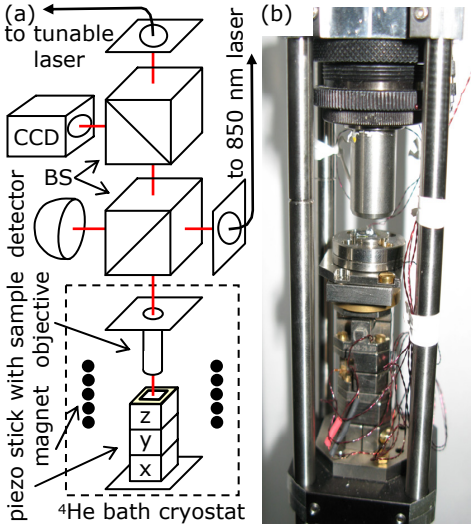

Figure 3.2: *(a) Schematics of the free-space microscope. The optical head consists of two beam sampler which direct light coming from the fibers into the objective. With the CCD and the photo detector the spot and the polarization is monitored. In the vacuum tube the sample can be moved with a piezo positioner under the objective. (b) Photograph of the positioner with the sample and transmission detector on top. The objective has a* $NA = 0.68$ *and a working distance of* 1.68 mm.

of the quantum dots and is transmitted mainly through the sample as the laser is transparent for GaAs. The detector collects the incoming photons and transforms it into a current.
The vacuum tube is during the experiment in a liquid ^{4}He bath cryostat with a superconducting magnet providing magnetic fields up to 9 T at 4.2 K.

3.1.2 ^{3}He-system

The lowest temperature achievable with a helium bath cryostat is 1.5 K if at the helium bath is pumped. To go down to temperatures of hundreds of mK a helium-3 cryostat is necessary. For this work a *Janis Research He-3-SVSD* insert incorporated in a helium-4 dewar with a superconducting magnet was used. It is a single-shot version with a hold time of 80 h at a nominal base temperature of 250 mK. The cooling unit consists of three parts: the sorption pump (sorb), the 1 K pot and the ^{3}He pot (see Fig. 3.3(a)). These three parts form one common space which is hermetically isolated as it contains the helium-3. The base temperature is obtained by pumping with the sorption pump at liquid helium-3 in the ^{3}He pot. Liquid helium-3 has 1.2 K and if the vapor pressure is reduced it can cool down below 300 mK. The sorption pump contains charcoal at which the gaseous helium-3 is absorbed at temperatures

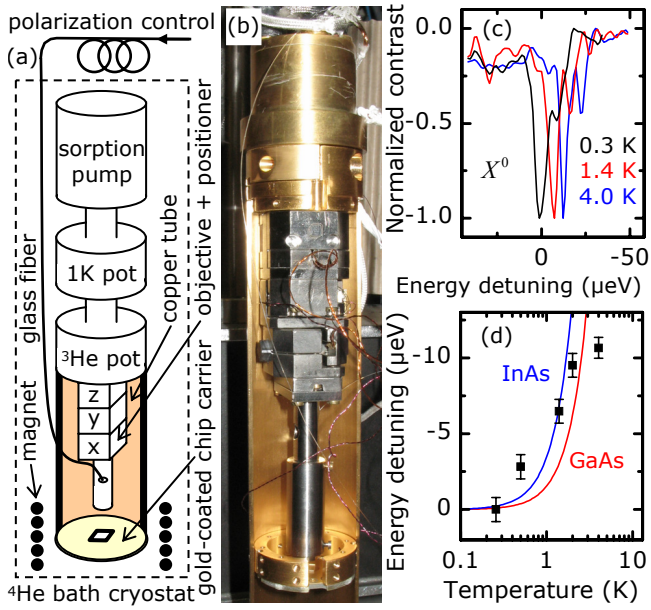

Figure 3.3: *(a) Sketch of the essential part of the ^{3}He-system. The sorption pump, the 1 K pot and the ^{3}He pot cool down the system to sub-Kelvin temperatures. The sample is glued on a gold-coated chip-carrier which is thermally coupled to the ^{3}He pot via a copper tube. The fiber-based microscope objective is mounted on a piezo positioners. (b) Picture of the microscope part with the ^{3}He pot. (c) Resonances of a neutral exciton measured at different temperatures. (d) Temperature tuning of the resonance energy in comparison with the band gap tuning behavior of bulk InAs or GaAs.*

between 4 K and 40 K. The sorption pump can be cooled by pumping at a capillary fed by the helium-4 bath and has also a heater. If all helium-3 is absorbed by the sorption pump it is heated above 40 K and the again evaporated ^{3}He condenses in the 1 K pot (cooled by a capillary) and runs back as a liquid into the ^{3}He pot. As soon as the temperature of the sorption pump is lowered below 40 K it starts to pump and cool the helium-3 again. The amount of absorption and therefore the temperature of the He pot is determined by the temperature of the sorb. Therefore by setting the temperature of the sorb by means of cooling or heating the temperature at the ^{3}He pot can be adjusted within an accuracy of 1 mK [69]. To control and maintain the different temperatures thermometers are fixed at the sorption pump, the 1 K pot and the ^{3}He pot.

The *Janis* ^{3}He system is a commercially available system without optical access. The insert was prepared for optics experiments using the concept of a fiber-based confocal microscope. At the helium-3 pot an *Attocube* slip-stick positioner with axis x, y and z is attached on which the objective is mounted. A glass fiber conveys the laser light to the objective and collects also the emitted light. The base temperature

is achieved at the ^{3}He pot at which a copper tube consisting of two halfs is fixed. A gold coated chip carrier with the sample is attached to the lower end of the copper tube. The sample which is glued onto the carrier with conductive silver is thermally coupled to the ^{3}He pot via the gold area and the copper tube. To ensure optimal thermal conduction between the sample and the ^{3}He pot only metallic components are used which are mechanically linked to the each other. A photo of the optical part of the ^{3}He system is depicted in Fig. 3.3(b).
In Fig. 3.3(c) three spectra of the neutral exciton of a quantum dot are shown. They were measured at different temperatures between 250 mK and 4.2 K under identical conditions by scanning the tunable laser. A clear red-shift with increasing temperature is visible demonstrating the temperature tuning in the helium-3 cryostat. Fig. 3.3(d) summarizes the shift which matches qualitatively with the expected red-shift due to the change of the band gap with temperature [70].

3.2 Optical and electrical setup

In Fig. 3.4 the setup used is shown. There are three units: the modulation unit, the excitation unit and the detection unit. In the course of this thesis the setup was build up and optimized for quantum dot spectroscopy.
The electrical unit is connected to the electrical contacts of the sample and provides the externally applied gate voltage (chapter 2.2). Additionally to the DC bias voltage an AC voltage with a typical modulation amplitude of 200 mV is added. The function generator (*Keithley 3390*) supplies a rectangular voltage at a modulation frequency of 77.137 Hz which is in a frequency range with low noise for this setup. The DC voltage is taken from a *Knick S252* voltage meter. DC and AC voltage are mixed via a home-built active coupler which is connected to the electrical contacts of the sample.
The central equipment of the excitation unit is the wavelength-tunable external cavity laser diode from *Sacher Laser*. Two models were used: *Sacher LION NL-960-0907-0111* in combination with the *Pilot PZ500* and the *Sacher TEC-500P-960-30* with the *MD1000* box. Both can be operated in the range of 990 nm to 910 nm, have a typical mode-hop free range of about 200 pm and the spectral linewidth of the laser is considerably below one pm. A Faraday isolator (FI) *Linos FI960-5SI* at the optical output guarantees that now back reflection from optical elements cannot enter the laser to prevent oscillations of the laser. The laser light is power stabilized to reduce the noise in the experiment (factor of 4 better than without stabilization). A detailed schematics and explanation of the power stabilization can be found in [71]. A small part of the laser light enters a scanning Fabry-Perot interferometer (SFP) to monitor single-mode operation of the wavelength-tunable laser. Another part is sent to a *High Finesse Ångstrom WS/7* wavemeter which measures the wavelength of the laser emission. Via a PID-loop of the wavemeter the laser can

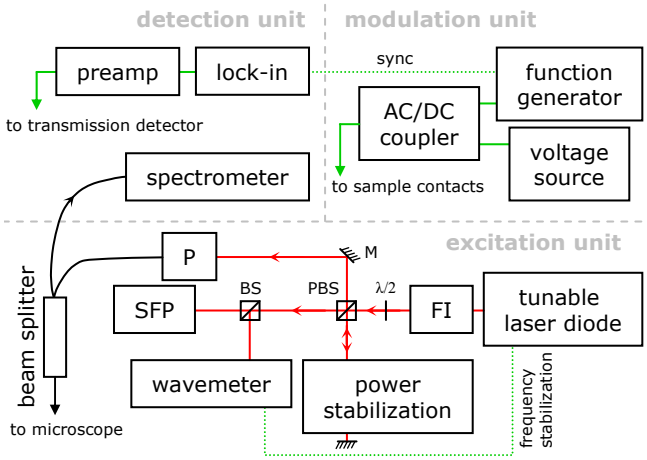

Figure 3.4: *The gates of the sample are connected to a function generator and a DC voltage source via an AC/DC mixer. The modulation with a rectangular voltage allows to use a lock-in technique. The transmission signal from the detector is pre-amplified and sent to the lock-in. For the resonant excitation a wavelength-tunable laser is employed which is power- and frequency stabilized. The laser light is monitored with a scanning Fabry-Perot interferometer (SFP) and a wavemeter. The polarization unit (P) allows to define any polarization state (BS = beam splitter; PBS = polarizing beam splitter; M = mirror).*

be frequency-locked. The main part of the laser light which is transmitted through the PBS passes polarization paddles and neutral density filters allowing to adjust polarization and laser power in the microscope.
For photoluminescence experiments a spectrometer (*Horiba JobinYvon Spex500M*) with a focal length of 500 mm and a CCD camera from *Princeton Instruments Spec-10* with a spectral resolution of 42 μeV is used. The transmission detector underneath the sample is connected to the preamplifier *DL Instruments 1211* which also transforms the current into a voltage. Typically an amplification of 10^9 V/A is set whose bandwidth of 4 kHz is well above the used $f_{mod} = 77.137$ Hz. A lock-in amplifier *EG&G 7260* multiplies the incoming signal with the reference signal and the product passes a low pass filter with a bandwidth f_{BW} which depends on the integration time. By this only signals with frequencies in the interval $[f_{mod} - f_{BW}; f_{mod} + f_{BW}]$ are obtained.

3.3 Spectroscopy techniques

Quantum dots have been investigated with capacitance spectroscopy (CV) [72], FTIR spectroscopy [73], photoluminescence (PL) [74, 49, 44] and differential trans-

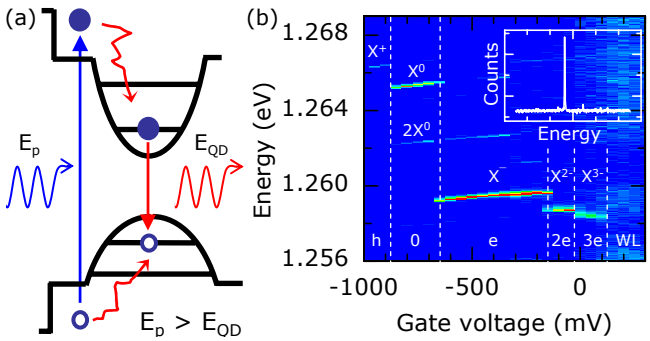

Figure 3.5: *(a) Principle of photoluminescence spectroscopy: The laser photons are absorbed in the wetting layer and create electron-hole-pairs. Electrons and holes relax non-radiatively into the lowest energy levels of the quantum dot and recombine optically under emission of photons. (b) Photoluminescence map of a single InGaAs quantum dot. The inset shows a single spectrum of which the 2D map consists of. Depending on the external gate voltage different exciton states are favored like the neutral and charged excitons.*

mission spectroscopy (DT) [59, 53]. The latest development in the field of quantum dot spectroscopy is resonant fluorescence [19]. In this thesis CV spectroscopy, photoluminescence and transmission spectroscopy were employed with a strong focus on DT.
With photoluminescence spectroscopy the different neutral and charged excitons and biexcitons can be easily found and identified. This is exploited to find optical resonances in DT. Due to the small linewidth of the transmission laser and its limited mode-hop free scan range it is difficult and time-consuming to directly search the resonance. Therefore the quantum dot of interest is measured in PL and for instance the neutral exciton line is chosen. Now the attenuated resonant laser is sent into the spectrometer and the laser is tuned on resonance. Then DT is applied on the quantum dot resonance by scanning the gate voltage. As the resolution of the spectrometer is two orders of magnitude larger than the laser linewidth it can be necessary to repeat the procedure by slightly detuning the laser to obtain the resonance.

3.3.1 Photoluminescence spectroscopy

Photoluminescence spectroscopy generates electron-hole pairs far off resonance in the semiconductor material. The charge carriers relax non-radiative into the energetically lowest unoccupied states and recombine optically by emitting a photon. PL is the most common spectroscopy method for self-assembled quantum dots.
In the case of the free-space microscope an 850 nm diode laser (*Roithner QL8536SA-*

L) with an output power of 40 mW is coupled into the side arm of the microscope (schematics in Fig. 3.2(a)). The laser beam is deflected by the BS and focused on the quantum dot. Its emission is collected by the objective and enters the glass fiber at the top arm which is connected with the spectrometer. In the ^{3}He system only one glass fiber is available so that it is used for both excitation and emission. A 830 nm excitation laser (*Roithner RLT8340MG*) is coupled into a 90:10 fiber beam splitter (*Thorlabs FC980*) which is connected to the microscope. The emitted photons are directed through the objective and the 90% arm of the fiber beam splitter into the spectrometer.
Fig. 3.3.1(a) shows schematically the processes involved in photoluminescence. The laser excites electron-hole pairs by absorption of a photon with energy E_p in the wetting layer and is transparent for GaAs. The amount of charges created depends on the laser power. The electrons and the hole relax by non-radiative relaxation mechanisms into the quantum dot and then into the lowest (highest) available electron (hole) states. These non-radiative relaxation processes occur in the ps range [75]. Typically after hundreds of ps [30] the electron-hole pair recombines optically. Since PL is a non-resonant technique with several processes involved the spin and phase are not conserved. If the pumping rate of the excitation laser is high enough also biexcitons and other multiexcitons can be generated.
The emission emerging from a quantum dot is spectrally resolved in the spectrometer. By measuring at different gate voltages one obtains a typical 2D PL map like in Fig. 3.3.1(b). A single spectrum is shown in the inset of the figure. In the graph six exciton lines for the neutral (bi)excitons X^0 and $2X^0$ and the charged excitons X^+, X^-, X^{2-} and X^{3-} can be identified. The difference in the energies is a consequence of the interactions between the charges of the exciton states. The ground state occupations before excitation is shown at the lower edge of the graph.

3.3.2 Differential transmission spectroscopy

The differential transmission spectroscopy is a resonant technique and uses the absorption of photons by the quantum dot. It offers a high spectral resolution since the linewidth of the laser is considerably smaller than the natural linewidth of the quantum dot ($\approx 1\,\mu$eV [19]). It makes possible to select single optical transitions and to investigate them. As it offers access on the quantum dot dressed states [76] and the Mollow triplet [77] can be generated. In order to selectively excite one distinct transition of a degenerate state control of the polarization of the laser light is sufficient.
A transmission detector is mounted underneath the sample. Laser light arriving at the sample is transmitted through it as the laser energy is smaller than the band gap of GaAs. The transmitted light is then absorbed by the detector and transformed into a photocurrent signal. This photocurrent has a constant background which is caused by the laser photons. If the laser is tuned into resonance with a

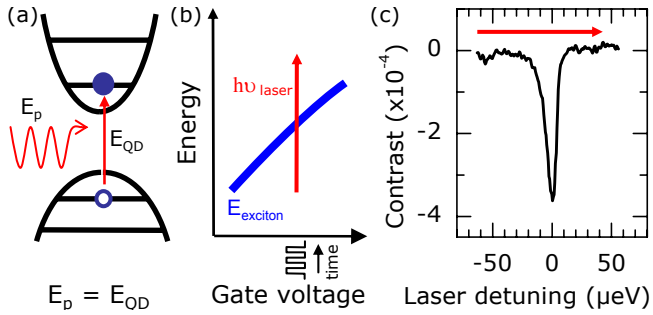

Figure 3.6: *(a) Resonant transmission spectroscopy exploits the absorption of laser photons by the quantum dot. The photocurrent at the detector (underneath the sample) is diminished if the laser is resonant with the quantum dot. (b) The transmission signal is recorded by tuning the laser energy over the exciton resonance. (c) In the transmission spectrum a dip occurs giving a measure for the number of absorbed photons.*

quantum dot transition a small part of the photons is absorbed (Fig. 3.6(a)). This decreases the number of photons arriving at the detector and appears as a dip in the photocurrent. The current is amplified and transformed into a voltage which is sent to the lock-in. The absorption contrast α features also the dip as depicted in Fig. 3.6(c). Theoretically a maximum absorption of 1.8% can be calculated [78]. The absorption curve is obtained by tuning a laser over the exciton resonance (compare Fig. 3.6(b)) and recording the corresponding transmission signal. As the absorption signal is less than 2% of the background current a lock-in technique is used to improve the signal-to-noise ratio. A rectangular-shaped voltage with a frequency of $f_{mod} = 77.137\,\mathrm{Hz}$ is superimposed on the bias gate voltage and an integration time of 1 s is typically used. The lock-in returns only signals with frequencies $f_{mod} \pm f_{BW}$ so the noise contributions from frequencies other than $f_{mod} \pm f_{BW}$ are neglected and the noise in the measurement signal is diminished.

Chapter 4

Theoretical concepts

In this chapter concepts are discussed which are used for the analysis of the experimental data in chapters 4 to 6. Characteristic properties of a quantum dot are for example confinement energies, interaction energies between electrons and holes, Rabi frequencies, spontaneous relaxation rates, coupling rates to reservoirs etc.
The comparison of resonance energies (vs. gate voltages) measured with differential transmission and photoluminescence allows to calculate the energies of the electron-electron-, hole-hole- and electron-hole interactions. Furthermore the confinement energies of the occupied states in conduction and valence band can be extracted [79]. The derivation of the optical Bloch equations for two-level systems is a semi-classical approach and describes the optical transition from ground to excited state. This model can be applied on an isolated quantum dot and the absorption and the lineshape can be derived. The calculations give a fairly good agreement with the experimental observations and allow to extract Rabi frequencies and relaxation rates from experimental data [80, 81].

4.1 Coulomb blockade model

In the quantum dot samples used in this thesis different excitonic states can be addressed by choosing a gate voltage V_g. As it is known from Fig. 2.5 the transition from one stable state to another one is characterized by a jump in the spectral energy. This behavior can be modeled in a Coulomb blockade model considering the interaction energies between electrons and holes. If one assumes to be in the ground state, which means for example that one has an empty quantum dot, no electron will tunnel in the dot as long as the lowest electron state is above the Fermi level (corresponding to $E_F = 0\,\mathrm{eV}$). If there is one electron in the dot the Coulomb repulsion between two identical charges prevents the charging with an additional electron as long as the additional energy due to the interaction of the electrons is

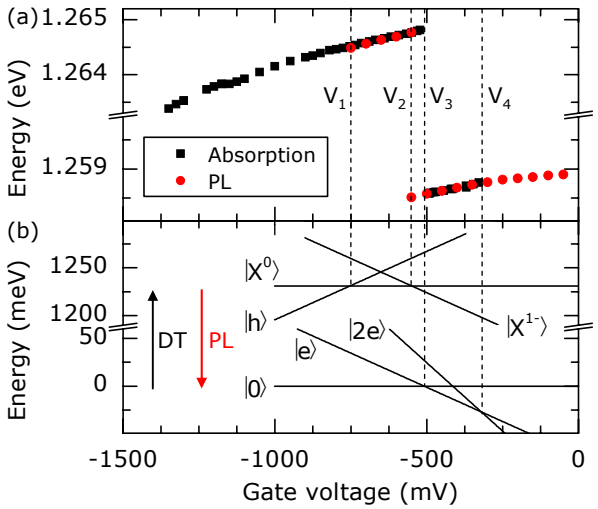

Figure 4.1: *Charging model for a quantum dot. (a) Neutral exciton and charged exciton measured with DT and PL. The gate voltages V_i label the ends of the plateaus or the transition from X^0 to X^-. (b) Energy diagram of the states involved in optical transitions. For absorption the states below* 50 meV *are the ground states and the ones above* 1200 meV *are the excited states. The energetically lowest state is stable and the gate voltages V_i correspond to the transition points between two states.*

not compensated. Only states which are lower in energy compared to the other states are stable.

In chapter 3.3 photoluminescence and differential transmission spectroscopy are introduced. The two techniques use the emission from excited states (PL) and the resonant absorption of photons by the ground states (DT). Therefore a comparison of PL and DT data shows that transitions between different types of excitons take place at different gate voltages and that the plateaus have different voltage ranges. This is a consequence of the non-resonant excitation in the photoluminescence which creates an effective electric field which can be calculated and with which the experimental data are corrected (see [79]. Differential transmission does not have such an effect as photons are either exciting the quantum dot or are not affected by the dot. In Fig. 4.1(a) the differential transmission (black) and the gate-voltage corrected photoluminescence (red) data of the neutral exciton X^0 and the charged exciton X^- are depicted (similar to [79]). From the photoluminescence and differential transmission data the electron-electron and electron-hole interaction in the investigated quantum dot can be obtained.

The gate voltages at which the X^0- and X^--plateaus end and at which one electron is loaded in the quantum dot (transition from X^0 to X^-) are different for photoluminescence and differential transmission. The characteristic voltages are marked as V_1 to V_4. In PL the neutral exciton is between V_1 to V_2 and the charged exciton is at

gate voltages above V_2 and does not end at V_4. On the other hand the X^--plateau measured in DT only appears between V_3 and V_4 while the neutral exciton can be also observed far beyond V_1. For the PL the exciton states define the optical behavior and in the case of DT the ground states are responsible for the behavior.
In Fig. 4.1(b) the ground states and the exciton states versus the gate voltage are plotted. The Stark shift is neglected as it is in the μeV-range and the typical shifts here are in meV. If two states cross each other a transition is possible as the one state with lower energy is favored over all the higher ones. Absorption is sensitive to the ground states therefore optical transitions increase the energy in the system (black arrow in Fig. 4.1(b)) and can occur even if the final state is not stable any more. The initial states for PL are the lowest states of the exciton states and relaxation reduces the energy of the quantum dot (red arrow in Fig. 4.1(b)). According to [79] the energies of the states can be expressed in terms of the electron-electron energy E_{ee}, the electron-hole energy E_{eh}, the confinement energy of the electron E_C and the energy of the mirror charge in the back contact $E_m = 1.1\,\text{meV}$. The energies E_{eh}^{11}, E_{eh}^{21}, E_{ee}^{11} and E_{ee}^{21} arise from the attractive (electron-hole) and repulsive (electron-electron or hole-hole) Coulomb interactions between the charges in the dot. In $E_i^{\varepsilon\eta}$ the index i defines the kind of interaction, ε stands for the number of electrons and η identifies the number of holes. $E_0 = 1.266231\,\text{eV}$ is the optical transition energy without the Stark shift and the electrostatic energy is defined by $E_\lambda(V_g) = e(V_S + V_g)/\lambda$ with the Schottky voltage $V_S = 620\,\text{mV}$ and the lever arm $\lambda = 7$.

QD state	Energy
$\|0\rangle$	0
$\|\text{e}\rangle$	$-E_\lambda(V_g) - E_C - E_m$
$\|2\text{e}\rangle$	$-2E_\lambda(V_g) - 2E_C - 4E_m + E_{ee}^{20}$
$\|\text{h}\rangle$	$E_0 + E_\lambda(V_g) + E_C + E_m$
$\|X^0\rangle$	$E_0 - E_{eh}^{11}$
$\|X^-\rangle$	$E_0 - E_\lambda(V_g) - E_C - E_m + E_{ee}^{21} - E_{eh}^{21}$

(4.1)

In the limit of strong confinement, i.e. with the assumption that the electron-electron Coulomb energy is independent of the occupation of holes in the valence band ($E_{ee}^{20} = E_{ee}^{21}$), the Coulomb energies and the confinement energy can be calculated. [82] shows that the electron-hole energies for the X^0 and X^- differ by about 5% so that $E_{eh}^{11} \approx E_{eh}^{21}$ is justified. Using equations 4.1 for the dot in Fig. 4.1 the following values were evaluated: $E_C = 160\,\text{meV}$, $E_{ee} = 29\,\text{meV}$ and $E_{eh} = 35\,\text{meV}$. The confinement energy of the hole E_C^h can be calculated by means of the known GaAs band gap $E_g = 1.519\,\text{eV}$, the confinement energy of the electron E_C, the transition energy E_0 and the electron-hole energy E_{eh}. In this case $E_C^h = E_g - E_0 - E_C - E_{eh}$ gives 58 meV.
A closer look at the ground states shows that the empty state $|0\rangle$ is stable up to gate

voltage V_3 that means absorption of photons can take place driving the quantum dot in state $|\mathrm{X}^0\rangle$. The reason for this is that the lowest electron state is above the Fermi energy and therefore the unperturbed quantum dot is in the empty state. At gate voltages below V_1 $|\mathrm{h}\rangle$ is stable instead of $|\mathrm{X}^0\rangle$. Nonetheless absorption still works but the linewidth of the resonance is broadened due to the tunneling of the electrons into the back contact. The linewidth can be approximated by $\Gamma = \Gamma_0 + 2\hbar\gamma_t$ where Γ_0 is the linewidth of the optical transition and γ_t are the tunneling rates involved. At V_3 the empty and the one-electron state cross and therefore $|\mathrm{e}\rangle$ becomes stable as it is populated. The now unoccupied state $|0\rangle$ cannot absorb photons any more. At the intersection of $|\mathrm{e}\rangle$ and $|2\mathrm{e}\rangle$ which lies at gate voltage V_4 the dot is charged with a second electron. This implies that all s-states are occupied and absorption is Pauli-blocked. Absorption of a photon generates another electron for which there is no empty state in the s-shell but only in the p-levels which are energetically far apart.
The photoluminescence addresses stable exciton states. Between V_1 and V_2 $|\mathrm{X}^0\rangle$ is stable and therefore a resonance is observed. At the left edge of the neutral exciton plateau the hole state intersects and becomes the dominant state in this voltage regime. As this state has no electron-hole pair it cannot recombine like an exciton and is rather the ground state for the $|\mathrm{X}^+\rangle$. Therefore PL from the neutral exciton is quenched and the positively charged exciton shows an optical signature as can be seen in Fig. 3.3.1(b). At gate voltages above V_2 the negatively charged exciton dominates as it represents the energetically lowest state. The extent of the plateau reaches far beyond the equivalent X^- signal in differential transmission as the X^{2-} luminescence stems from the electronic p-levels of the quantum dot. As the p-levels are far detuned in energy the $|\mathrm{X}^{2-}\rangle$ to $|2\mathrm{e}\rangle$ transition is blocked and the $|\mathrm{X}^-\rangle$ to $|\mathrm{e}\rangle$ transition is favored.
Two characteristic values which can be easily read from the PL-graph are the energy shift between the X^0- and the X^--plateau on additional charging of the quantum dot ($\Delta E_{PL}\left(\mathrm{X}^0 - \mathrm{X}^-\right)$) and the extent in gate voltage of the X^0-plateau $\Delta V_{PL}\left(\mathrm{X}^0\right)$. The equations are according to [82]:

$$\Delta E_{PL}\left(\mathrm{X}^0 - \mathrm{X}^-\right) = 2E_{eh}^{21} - E_{eh}^{11} - E_{ee}^{21} \tag{4.2}$$

$$\Delta V_{PL}\left(\mathrm{X}^0\right) = (\lambda/e)\left(2E_{eh}^{11} - 2E_{eh}^{21} + E_{ee}^{11} - 2E_m\right) \tag{4.3}$$

In photoluminescence experiments the exciton states determine the behavior. A simple consideration of the energy reduction of X^0 and X^- due to interactions between electrons and holes leads to equation 4.2. The X^- has two electrons and one hole. Therefore the charged exciton state is lowered by twice the electron-hole energy E_{eh}^{21} and increased by E_{ee}^{21} as the two electrons repel each other. However the neutral exciton is also lowered by an energy E_{eh}^{11} which needs also to be taken into account. The voltage extent of the neutral exciton can be derived from the equations in 4.1. The X^0-plateau in PL goes from V_1 to V_2 so that the equations for the crossing points of $|h\rangle$ with $|\mathrm{X}^0\rangle$ and of $|\mathrm{X}^0\rangle$ with $|\mathrm{X}^-\rangle$ can be rearranged in

such a way that one gets the formula for the voltage extent of the neutral exciton. If the assumption that $E_{ee}^{11} = E_{ee}^{21}$ is applied again and equations 4.2 and 4.3 are combined an expression can be found using only experimentally accessible quantities: $E_{eh}^{11} = \Delta E_{PL} + e\Delta V_{PL}/\lambda + 2E_m$. With the equations derived in this chapter the interaction and confinement energies of any quantum dot can be calculated from the experimental data.

4.2 Optical Bloch equations

The quantum dots are modeled as a quasi-atomic two-level system which describes the optical response of a quantum dot measured in absorption. The optical Bloch equations are semi-classical equations for atoms and can be extended to the multi-level case. For the description of the atom the corresponding quantum mechanical Schrödinger equation is used and the photons interacting with the atom are treated as a classical light field. With the rotating-wave approximation and in the rotating frame the response of the system undergoing optical excitation can be evaluated analytically.
From the optical Bloch equations the absorption coefficient $\alpha = \Delta T/T$ and the linewidth Γ can be calculated which are directly linked to the experimental observations. The absorption curve has a Lorentzian lineshape. The derivation of the Bloch equations and the corresponding α can be found in greater detail in reference [80].

4.2.1 The quantum dot as a two-level system

A two-level system with the ground state $|1\rangle$ and the excited state $|2\rangle$ is addressed with a coherent laser field $\vec{E} = \vec{E}_0 \cos(\omega t)$ (ω is the frequency of the laser). The wave function of the system is:

$$\begin{aligned} |\Psi\rangle &= c_1(t)\,|1\rangle + c_2(t)\,|2\rangle \\ |m\rangle &= \Psi_m \exp(-iE_m t/\hbar) \end{aligned} \tag{4.4}$$

with the eigenenergies E_m for the states $|m\rangle$ and the transition energy $\hbar\omega_0 = E_2 - E_1$. The Hamiltonian in the interaction picture is given by the atomic dipole moment $e\vec{D}$ and reads as $H_I = e\vec{D}\vec{E}_0 \cos(\omega t)$. Putting all this into the Schrödinger equation

$$H_I\,|\Psi\rangle = i\hbar\partial/\partial t\,|\Psi\rangle \tag{4.5}$$

leads to two coupled equations for the coefficients c_1 and c_2:

$$\Omega \cos(\omega t) \exp(-i\omega_0 t) c_2 = i \frac{dc_1}{dt} \tag{4.6}$$

$$\Omega \cos(\omega t) \exp(i\omega_0 t) c_1 = i \frac{dc_2}{dt} \tag{4.7}$$

$\Omega = e\mu_{12}E_0/\hbar$ is the Rabi frequency of the system and $\mu_{12} = \langle 1|D|2\rangle$ is the optical dipole matrix element.
A quantum system in a mixed state can be represented with the density matrix $\hat{\rho}$. Here the diagonal matrix elements correspond to physical quantities like the population of the states which are given by the diagonal elements. The off-diagonal elements are the so-called coherence terms. The equations 4.6 and 4.7 for the coefficients c_i can be transformed into an equation for the density matrix elements ρ_{ij} by:

$$\frac{d\rho_{ij}}{dt} = c_i \frac{dc_j^*}{dt} + \frac{dc_i}{dt} c_j^* \tag{4.8}$$

The resulting analytical equations

$$\frac{d\rho_{22}}{dt} = -\frac{d\rho_{11}}{dt} = -i\Omega \cos(\omega t) \left(\exp(i\omega_0 t)\rho_{12} - \exp(-i\omega t)\rho_{21}\right) \tag{4.9}$$

$$\frac{d\rho_{12}}{dt} = \frac{d\rho_{21}^*}{dt} = i\Omega \cos(\omega t) \exp(-i\omega_0 t) \left(\rho_{11} - \rho_{22}\right) \tag{4.10}$$

can be simplified by the rotating-wave approximation. By expanding the cosine into its exponential form two oscillatory parts with frequencies $\omega_0 - \omega$ and $\omega_0 + \omega$ can be distinguished. The fast-oscillating terms with $exp(\pm i(\omega_0 + \omega)t)$ can be neglected in rotating wave approximation as the transition frequency of the two-level system is typically many orders of magnitudes slower than $\omega_0 + \omega$. With the transformation of the equations of motion for the density matrix elements into a rotating frame by means of

$$\tilde{\rho}_{ii} = \rho_{ii}, \quad \tilde{\rho}_{12} = \rho_{12} \exp(i(\omega_0 - \omega)t), \quad \tilde{\rho}_{21} = \rho_{12} \exp(-i(\omega_0 - \omega)t) \tag{4.11}$$

the optical Bloch equations are obtained.
The Bloch equations are supposed to describe a two-level system with spontaneous relaxation from state $|2\rangle$ to $|1\rangle$. This is not yet included in the derivation and requires a modification of equation 4.7 in such a way that in absence of a laser field the population ρ_{22} and thus c_2 vanishes. The physical reason for this effect is the spontaneous emission governed by the rate γ_{sp}. The following substitute for 4.7 implements a decay term in the set of equations:

$$\Omega cos(\omega t) exp(i\omega_0 t) c_1 - i\gamma_{sp} c_2 = i \frac{dc_2}{dt} \tag{4.12}$$

To consider also other relaxation mechanisms (like e.g. collision broadening) an extended decay coefficient $\gamma = \gamma_{sp} + \gamma_{coll}$ is introduced. The general optical Bloch equations accounting for an atomic two-level system excited with photons in the visible or infrared spectrum are as follows:

$$\frac{d\tilde{\rho}_{22}}{dt} = -\frac{d\tilde{\rho}_{11}}{dt} = -\frac{1}{2}i\Omega\left(\tilde{\rho}_{12} - \tilde{\rho}_{21}\right) - 2\gamma_{sp}\tilde{\rho}_{22} \tag{4.13}$$

$$\frac{d\tilde{\rho}_{12}}{dt} = \frac{d\tilde{\rho}^*_{21}}{dt} = \frac{1}{2}i\Omega\left(\tilde{\rho}_{11} - \tilde{\rho}_{22}\right) + \left(i(\omega_0 - \omega) - \gamma\right)\tilde{\rho}_{12} \tag{4.14}$$

4.2.2 Differential transmission and the density operator

The Bloch equations 4.13 and 4.14 can be solved analytically for the steady-state case, $d\tilde{\rho}/dt = 0$. Their solutions are

$$\tilde{\rho}_{22}(\infty) = 1 - \tilde{\rho}_{11}(\infty) = \frac{(\gamma/4\gamma_{sp})\Omega^2}{(\omega_0 - \omega)^2 + \gamma^2 + (\gamma/2\gamma_{sp})\Omega^2} \tag{4.15}$$

$$\tilde{\rho}_{12}(\infty) = \tilde{\rho}^*_{21}(\infty) = -\frac{(\Omega/2)(\omega_0 - \omega - i\gamma)}{(\omega_0 - \omega)^2 + \gamma^2 + (\gamma/2\gamma_{sp})\Omega^2} \tag{4.16}$$

The diagonal elements are related to the relative occupation N_i/N of the state $|i\rangle$ and the off-diagonal elements can be linked to the absorption coefficient α and the linewidth of the measured Lorentzian resonance which is obtained for instance in transmission experiments. For this a relation between the absorption coefficient and $\tilde{\rho}_{21}$ is developed. The polarization created by an electric field $E(t) = 1/2E_0(exp(-i\omega t) + exp(i\omega t))$ is

$$P(t) = \frac{1}{2}\epsilon_0 E_0(\chi(\omega)exp(-i\omega t) + \chi(-\omega)exp(i\omega t)) \tag{4.17}$$

with the linear susceptibility χ and the dielectric constant ϵ_0. If a quantum mechanical picture is used the polarization can be computed using the induced dipole moment $\hat{d} = e\hat{X}$ ($\hat{X}$ is the dipole moment along the x-axis, V is the volume) and reads as

$$P(t) = -\frac{1}{V}\langle\Psi|\hat{d}|\Psi\rangle = -\frac{e}{V}\left(\mu_{12}\tilde{\rho}_{21}exp(-i\omega t) + \mu_{21}\tilde{\rho}_{12}exp(i\omega t)\right) \tag{4.18}$$

Comparison of both equations 4.17 and 4.18 for the polarization yields for the susceptibility

$$\chi(\omega) = -\frac{2e^2\mu_{12}^2}{\epsilon_0 V\hbar\Omega}\tilde{\rho}_{21} \tag{4.19}$$

This results in the relation between the absorption coefficient and the density matrix element $\tilde{\rho}_{12}$:

$$\alpha = \frac{\omega_0}{cn}\,\mathrm{Im}[\chi(\omega)] = \alpha_0 \frac{\gamma}{\Omega}\,\mathrm{Im}[\tilde{\rho}_{12}] \tag{4.20}$$
$$\text{with} \quad \alpha_0 = \frac{6\Pi c^2}{\mathrm{Vn}\omega_0^2}$$

The experimentally accessible quantities contrast α and linewidth Γ can then be expressed as:

$$\alpha = \frac{\Delta T}{T} = \alpha_0 \frac{\gamma^2/2}{(\omega_0-\omega)^2 + \gamma^2 + (\gamma/2\gamma_{sp})\Omega^2} \tag{4.21}$$

$$\Gamma = 2\left(\gamma^2 + \frac{\gamma}{2\gamma_{sp}}\Omega^2\right)^{1/2} \tag{4.22}$$

Here ΔT is the change of the transmission which is normalized to the overall transmission T in α. Both equations are functions of the externally tunable parameters laser detuning $\delta = \omega_0 - \omega$ and Rabi frequency Ω.

4.3 Saturation of the quantum dot transition

Equations 4.21 and 4.22 given in the previous chapter depend on the Rabi frequency Ω which is for a given dipole matrix element a measure for the electric field of the excitation laser. Therefore Ω can be also written in terms of the laser power $P \propto \Omega$. By means of measuring α and γ for different laser powers the Rabi frequency can be extracted from fitting.
Similarly to atomic transitions a quantum dot transition shows saturation at high laser powers or strong electric fields, respectively [80, 78] . There are primarily two consequences: the contrast α decreases and the linewidth Γ increases above a certain saturation power. These phenomena is also described by equations 4.21 and 4.22 and can be easily seen if they are written in terms of the laser power.
Saturation of the optical transition of a two-level system occurs only on resonance. At low laser powers the recombination from $|2\rangle$ to $|1\rangle$ is determined by the spontaneous emission rate γ_{sp}. This implies the quantum dot relaxes in its ground state after an exciton lifetime $\tau = 1/\gamma_{sp}$. The probability that within this time τ a second photon is scattered at the quantum dot is very low. If γ_{sp} and the time between two scattered photons are similar the absorption starts to saturate as the quantum dot is still in the excited state and cannot absorp another photon. At high laser powers the probability of stimulated emission is increased. That means that the quantum dot interacts with an incoming photon though it is already in the excited state. The second photon depopulates $|2\rangle$ and two identical photons are emitted which do not

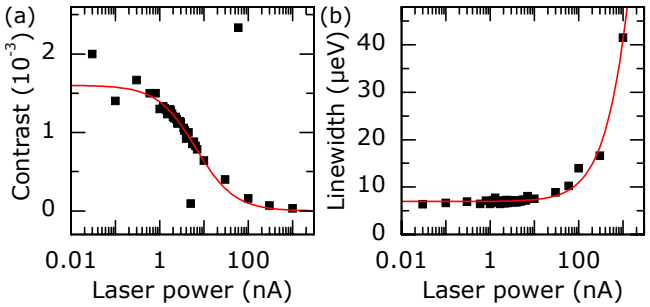

Figure 4.2: *Contrast (a) and linewidth (b) of a quantum dot at different powers of the wavelength-tunable laser. The contrast $\alpha = \Delta T/T$ decreases as soon as the quantum dot is driven into saturation. Accordingly the linewidth of the resonance peak broadens due to stimulated emission. The fit (red curve) coincides very well with the data (black squares) and allows to extract the Rabi frequency and the spontaneous relaxation rate.*

contribute to the absorption of the system. Due to that the absorption coefficient α diminishes with laser power. The stimulated emission enforces a relaxation even if the the time between absorption event and stimulated emission is shorter than the lifetime of state $|2\rangle$. This leads to the experimentally supported observation of a power broadening of the linewidth.
In Fig. 4.2 experimental data of a quantum dot emitting at a resonance energy 1.2915 eV is shown as a function of laser power. In Fig. 4.2(a) the contrast is depicted which reduces substantially starting with 0.0015 towards higher laser powers. Fig. 4.2(b) shows the corresponding power-dependent broadening of the linewidth with 7 μeV at very low laser powers.

To link the quantities α, Γ and the signal-to-noise ratio SNR with the laser powers it is necessary to deduce a relation for the Rabi frequency Ω and P. The absolute value of the Poynting vector $\vec{S}$ is the intensity which can be written as $I = |\vec{S}| = 1/2cn\epsilon_0 E_0^2 = P/A$ with the speed of light c, the electric field E_0 and the area of the laser spot A. The Rabi frequency converts then into ($\alpha_0\gamma$ from [78]):

$$\Omega^2 = \frac{e^2\mu_{12}^2 E_0^2}{\hbar^2} = \frac{2\alpha_0\gamma}{\hbar\omega_0}P \qquad (4.23)$$
$$\text{with} \quad \alpha_0\gamma = \frac{\mathrm{e}^2\mu_{12}^2\hbar\omega_0}{\mathrm{A}\hbar^2\epsilon_0\mathrm{nc}}$$

Inserting equation 4.23 into 4.21 and 4.22 and choosing resonant conditions ($\delta = 0$)

gives then the power-dependent formulas:

$$\alpha = \frac{\alpha_0}{1 + \frac{P}{\hbar\omega_0\gamma_{sp}\alpha_0}} \tag{4.24}$$

$$\Gamma = 2\gamma\left(1 + \frac{\alpha_0}{\hbar\omega_0\gamma_{sp}}P\right)^{1/2} \tag{4.25}$$

These two equations are fitted to the data in Fig. 4.2. A good agreement between the fit curves and the experiment is achieved.
The signal-to-noise ratio gives the optimal working conditions for differential transmission spectroscopy as it has an global maximum which is typically around 2 nW. The signal is α and the dominant noise source in these experiments is shot noise of the laser [81]. From photon statistics it is known that shot noise for coherent light is $\sqrt{\Delta n} = \sqrt{dN/dt} = \sqrt{P/(\hbar\omega_0)}$ where Δn is the variance of the photon number and dN/dt represents photons of the laser per unit time [83]. Hence the SNR is as follows:

$$SNR = \frac{\alpha}{noise} = \frac{\sqrt{P/\hbar\omega}}{1/\alpha_0 + P/\hbar\omega_0\gamma_{sp}} \tag{4.26}$$

Chapter 5

Coulomb interaction of quantum dots with single charges

Self-assembled InGaAs quantum dots have been introduced as isolated systems embedded in a solid-state matrix [49]. However quantum dots are affected by nuclear spins [84], defects [22] and charges [85] which are intrinsic in the surrounding solid state matrix and can cause fluctuations of the optical resonance of a quantum dot. Quantum dots in the context of charge fluctuations have been explored by several groups [85, 86]. Recently Houel et al. have analyzed the neutral exciton resonance as a function of pump laser power. They have observed jumps in the power dependence and argue that this is caused by local charging events which are located at the interface between GaAs and the superlattice (compare Fig. 2.3) [21].
In this chapter the interaction between a quantum dot and single or few charges trapped in the vicinity of the quantum dot is investigated. The usually linear exciton energy dispersion exhibits discontinuities with energy shifts up to $38\,\mu$eV which are attributed to charging or discharging events in the vicinity of the quantum dot. The energy shift and the gate voltage at which the charging takes place allows to model the effect and to draw a conclusion about the type of impurity involved in the charging.

5.1 Fluctuating quantum dot resonances

Charge fluctuations close to a quantum dot can have two implications on a quantum dot resonance. In general the charge changes the local electric field at the quantum dot site which shifts its optical resonance. If this charge fluctuates on a time scale much faster than the measurement time several coexisting peaks can be measured. If the impact of a fluctuating charge on the quantum dot is very small (i.e. on the order of the linewidth), for instance because it is far away from the quantum dot,

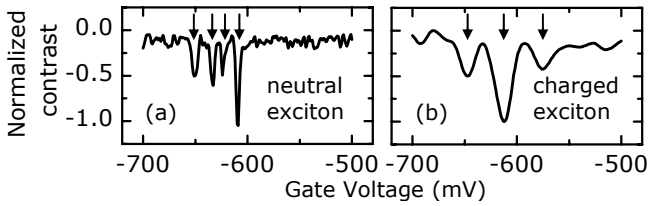

Figure 5.1: *Quantum dots with fluctuations leading to additional resonances. (a) Neutral exciton at* 1.27691 eV *with optical polarization of the laser in such a way that both fine structure components are detected. The fluctuations in the environment lead to four peaks. (b) DT of a charged exciton at* 1.28697 eV *with three resonances. The* X^- *exhibits only one resonance and the other two stem from fluctuations.*

then the linewidth of the resonance broadens. On the other hand if the energy shift is large coexisting resonances can be observed.
Quantum dots in different samples were characterized and a certain amount show several coexisting resonances. The neutral exciton is characterized by a fine structure splitting (chapter 2.3.1) so that it exhibits two resonances. In Fig. 5.1(a) the laser is linearly polarized in such a way that both fine structure components are excited. However four peaks appear in the spectrum, i.e. twice as many as expected. This can be interpreted as an abrupt shift of the resonance energy due to fluctuations. It requires that the fluctuation source has a bistable characteristic which means it switches between two different states with respective changes of the quantum dot electrostatic environment.
The observation of two or more resonances violating the two level picture is rather common in InGaAs samples and not only restricted to the neutral exciton. Fig. 5.1(b) depicts the resonance of a negatively charged exciton. The observation of two weak and one strong peak contradicts the expectation of only one resonance. In this case two charging events occur in the scanned voltage range. The charges occupy their lattice sites close to the quantum dot as a function of the gate voltage and lead to a Coulomb interaction with the quantum dot. While scanning the gate voltage at V_1 the first charging event shifts the resonance energy by $36\,\mu$eV and at the second charging voltage $V_2 > V_1$ the shift is $37\,\mu$eV.

5.2 Impurity charging model

The neutral exciton dispersion relation has typically an almost linear behavior with a Stark shift of roughly $1\,\mu$eV/mV as it is shown in Fig. 6.1. The neutral exciton is sensitive to an external electric field which is applied via the field effect structure (compare chapter 2.2). Any local change of the electric field at the quantum dot site is translated in an energy shift of the quantum dot state. The strength of the

interaction and the minimum field detectable is determined by the exciton dipole moment. The single charge is treated as a point charge.
The quantum dot exciton is treated as a dipole which is in the electric field of the point charge. With electrostatics the distances between quantum dot and charge can be calculated from the energy shifts. The calculations define boundary conditions for the maximal and minimal values of the distance. A second set of boundary conditions can be extracted from the simulation of the charging event which makes it possible to determine the relative position of the point charge taking into account the gate voltages at which the jumps occur. In this chapter three quantum dots and four charging sites are analyzed and the combination of both models (energy shift and gate voltage versus distance) allow to calculate the positions of quantum dots and charging sites.

5.2.1 Dot-impurity interaction

A comprehensive plateau of a neutral exciton is shown in Fig. 5.2(a). The basically linear dispersion curve features several jumps in energy and partially two or three coexisting resonances. The four jumps at gate voltages of $-557\,\mathrm{mV}$, $-526\,\mathrm{mV}$, $-485\,\mathrm{mV}$ and $-400\,\mathrm{mV}$ show a blue shift in exciton energy. The energy shifts are in the range of 7 to $38\,\mu\mathrm{eV}$.
In a line cut along the gate voltage axis at $1.274404\,\mathrm{eV}$ two resonances can be discriminated (5.2 (b) left panel). In this particular case the optical polarization of the resonant laser is chosen in such a way that only one fine structure component is detected. Instead of a single resonance two resonances are observed with one being weak and one being more pronounced in the spectrum. That means that two charging events are accessible within the gate voltage range of $150\,\mathrm{mV}$. In the laser scan only one resonance was found at certain gate voltages (5.2 (b) right panel). The fact that in the gate scan two resonances are present and in the laser scan there is only one in this region suggests that the charging event must be governed by the externally applied gate voltage. The quantum dot, and thus the characteristics of the exciton dispersion, is highly sensitive for charges. If a charge is trapped in the vicinity of the quantum dot for all parameters such as gate voltage, magnetic field etc. the whole energy plateau is shifted in gate voltage. If a charge tunnels into or out of an electronic state close to the quantum dot at a certain gate voltage V_c a discontinuity should be observable. This implies that the shift in gate voltage which is associated with a jump in energy takes place at V_c. Such a charging event can be detected as an abrupt change in the optical resonance energy of the quantum dot. Every event changes the overall local electric field seen by the quantum dot so that n jumps correspond to n charging events. The jump in exciton energy ΔE can be expressed in terms of the fixed dipole moment of the exciton $\vec{p} = e\vec{r}$ and the electric

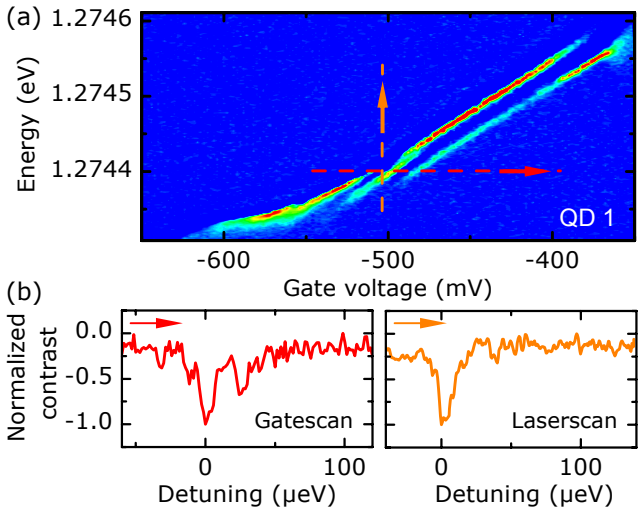

Figure 5.2: *(a) Dispersion of the neutral exciton at* 4.2 K. *Besides the linear Quantum Confined Stark effect several abrupt changes in the exciton dispersion are observed. (b) Linecuts along the dashed lines shown in the colorplot in (a): the gate-scan (left panel) at a laser energy* $E_L = 1.274404\,\mathrm{eV}$ *shows two resonances although only one fine structure component of the neutral exciton is addressed (by the light polarization). On the other hand in the laser-scan (right panel) at a gate voltage of* $-503\,\mathrm{mV}$ *only a single resonance appears.*

field of the charge at the location of the quantum dot $\Delta\vec{F}$:

$$\Delta E = -\vec{p} \cdot \Delta\vec{F} \tag{5.1}$$

The only free paramter in equation 5.1 is the distance $\vec{r}$. $\vec{p}$ is calculated from the Stark effect and ΔE is the energy shift of the discontinuity. From the energy shifts one can calculate boundary values within which the charging site needs to be situated.

In a semiconductor matrix there are different types of impurities such as dislocations, doping atoms etc. The jumps show a blue shift which requires that either an acceptor is between quantum dot layer and top gate or that a donator is located between back contact and quantum dot layer. Here only electron or hole charging is taken into account. Candidates for impurities in the GaAs layers around the quantum dots are primarily carbon and silicon. A carbon background is always present in these samples as a contamination of the semiconductor during growth in the MBE is inevitable. On the other hand Silicon atoms are deliberately inserted in high concentration underneath the quantum dot layer (in the back contact). As Kleemans et al. [31] have shown in X-STM measurements single silicon atoms can diffuse towards the quantum dot layer and could be close enough to be detected.

Both impurities are in the band gap of GaAs with silicon being $E_{Si} = 5.8\,\mathrm{meV}$

below the conduction band [41] and carbon being offset by $E_C = 26\,\text{meV}$ from the valence band [14, 41]. Tunneling of a charge which induces a jump in the exciton dispersion takes place if the electronic state of the impurity is in resonance with a charge reservoir. For silicon the electron reservoir is the Fermi sea in the back contact and carbon is coupled to the 2-dimensional hole gas at the interface with the superlattice (see chapter 6.3 [79]). The Fermi level is pinned at the top of the Fermi sea and doesn't change with the externally applied electric field while the silicon state is tunable with the electric field. If the silicon impurity is below the Fermi level it is neutral and above it is charged. Thus the charging event occurs when the impurity state hits the Fermi level. In a similar way the carbon state is neutral as long as it is below the highest band of the triangular quantum well for the hole gas. If the impurity and the highest hole band are energetically identical a hole tunnels into the impurity. The energy of the states of the hole gas are modified with the electric field in two ways: firstly it changes energy according to the lever arm and secondly the confinement is changed so that the level separation in the quantum well increases with increasing field.

5.2.2 Capacitor model and discharging of the impurity

The electrostatic environment of a quantum dot significantly affects its resonance energy. If the environment changes at a gate voltage V_c which is within the range of the exciton plateau this change can be detected as a shift in energy. As the minimal linewidth in this case is on the order of $5\,\mu\text{eV}$ only energy shifts larger than $5\,\mu\text{eV}$ can be resolved. In the model the electrostatic conditions at the quantum dot need to be simulated. In this model only perturbations of the system like a charging event are taken into account. The simulation of the quantum dot and the impurities in a simple plate capacitor is justified by the sample geometry.

Capacitor model

The electrostatics in the sample is modeled in a capacitor picture where the metal plates represent the quasi-metallic back contact of the sample and the Ni-Cr top gate as it is depicted in Fig. 5.3(a). A dipole and a single point charge are placed within the capacitor plates. The dipole represents the exciton with dipole moment $\vec{p}$ which varies from quantum dot to quantum dot. The impurity charge can be placed anywhere in the capacitor both on the axis of the dipole and off-axis. To ensure zero electric field at the metal plates two mirror charges on both sides outside of the capacitor are taken into account. The capacitor model can be mathematically written in the following formula:

$$\Delta E = -\vec{p}\cdot\vec{F_1} + \vec{p}\cdot\vec{F_2} + \vec{p}\cdot\vec{F_3} \tag{5.2}$$

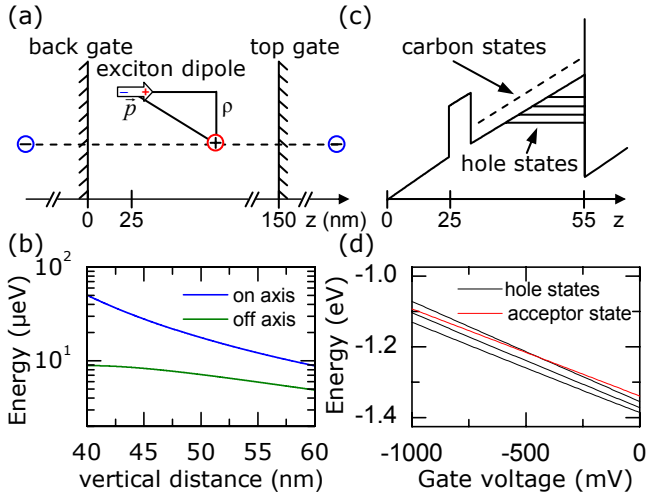

Figure 5.3: *(a) Capacitor model for the electric fields within the heterostructure. (b) The capacitor model allows to estimate distances along the growth axis between the impurity and the affected quantum dot. The "off axis" curve depicts the energy shifts if the impurity is shifted radially by* 20 nm. *(c) Model taking into account the tunneling between hole states in the triangular well at the interface to the superlattice and impurity states in the GaAs capping layer. (d) Energies of the hole states and of the carbon states are computed. At the gate voltages at which the curves cross tunneling has a high probability and a change of the electric field is detected.*

Here $\vec{F}_1$ represents the electric field of the impurity charge at the location of the quantum dot. $\vec{F}_2$ and $\vec{F}_3$ are the electric fields of the mirror charges on the back contact side and on the side of the top gate, respectively. F_i is given by

$$F_i = \frac{1}{4\pi\epsilon_0\epsilon}\frac{e}{\vec{r_i}^2} \tag{5.3}$$

with $\vec{r_i} = (\vec{r} - \vec{a})$ and $\vec{a} = a\hat{e_z}$ being the location of the charge. The Stark shifts are extracted from the exciton dispersion relations and translated into the corresponding dipole moments $\vec{p} = e\vec{r}$. In Fig. 5.3(b) the expected energy shifts relative to the distance along the growth axis (blue line) z are computed. The origin of the vertical axis is fixed at the back contact so the distance between the quantum dot and the impurity along the growth axis is then $z - 25\,\text{nm}$. In Fig. 5.3(a) a lateral displacement from the quantum dot axis is considered which results in the green curve in Fig. 5.3(b). In this case 20 nm were chosen as an example. Any radial deviation from the axis leads to a decrease of the energy shift so that the on-axis curve provides an upper boundary for the energy shift.

Charging events

As the discontinuities only occur at distinct gate voltages a tunneling mechanism between impurity states and the respective reservoir is necessary. The cases for silicon and carbon are discussed in terms of the charging voltage V_c and the position of the impurity along the growth axis z.
In order to calculate the charging voltages V_c for silicon impurities the lever arm of the field effect structure is used. As the Fermi energy is pinned the relative energy of the impurity state is given by the applied field which translates into the gate voltage V_g and the position z ($z = 0\,\mathrm{nm}$ at the back contact):

$$V_c = \frac{175\,\mathrm{nm}}{ez} E_{Si} + V_S \tag{5.4}$$

$V_S = 620\,\mathrm{mV}$ is the Schottky voltage of the sample and E_{Si} is the energy of the silicon donor.
In the case of carbon impurities a tunneling between the impurity states and the states in the triangular quantum well at the interface to the superlattice is considered. Whenever a Carbon state comes into resonance with the energetically highest level of the 2D hole gas tunneling of charges is possible. This implies that at a distinct gate voltage charging occurs and thus a jump in the exciton dispersion can be detected. The energies of the hole states and of the carbon states relative to the gate voltage is calculated. From the intersection points of these two curves the vertical distance in z between the quantum dot and the impurity are deduced.The highest level of a 2D hole gas at the interface of the superlattice is responsible for the jumping. Holes which tunnel out of the quantum dot populate the highest level in the 2D hole gas. If this level is tuned (by the gate voltage) into resonance with a carbon state the tunneling probability is dramatically enhanced. Depending on whether the carbon state is higher or lower in energy after detuning the impurity is either populated with a single charge or depopulated. The carbon state is given by

$$E_{carbon} = E_{gap} + E_C - \frac{e(V + V_S)}{\eta} \tag{5.5}$$

where E_{gap} is the band gap, E_C represents the energy how deep the impurity is in the band gap relative to the valence band and $\eta = 175\,\mathrm{nm/z}$ is the lever arm of the impurity. The energy of the n-th subband of the 2D hole gas in the triangular potential well can be approximated by the following formula:

$$E^n_{hole} = E_{gap} + \frac{e(V + V_S)}{\eta_{SL}} - c_n[\frac{(e\hbar)^2}{2m} F^2_{SL}]^{1/3} \tag{5.6}$$

$\eta_{SL} = \eta(z = 55\,\mathrm{nm})$ is the lever arm of the 2D hole gas, c_n is an Airy coefficient and $F_{SL} = (V - V_S)/175\,\mathrm{nm}$ is the electric field at the hole gas. In Fig. 5.3(d) the curves for the first three hole states (in black) and an exemplary carbon state are shown. At the intersection of the curves tunneling takes place.

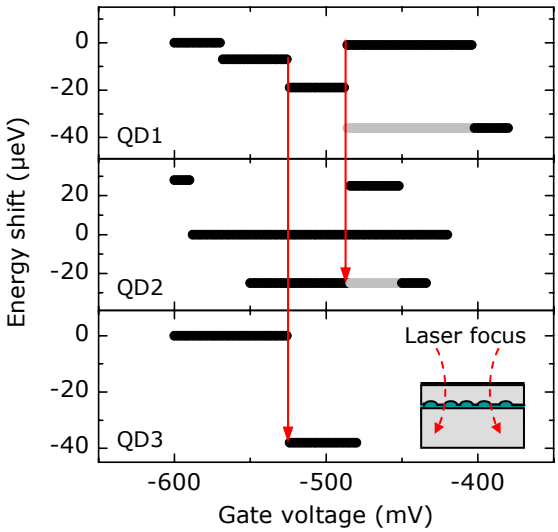

Figure 5.4: *Plateau of the neutral exciton for three different quantum dots. The linear Stark shift is subtracted for clarity. All three quantum dots are situated within one common laser spot (inset lowest panel). QD 1 shows three distinct jumps in the exciton dispersion, QD2 has two and QD3 features one discontinuity. QD1 and QD2 have one jump in common which is at a gate voltage of* $-485\,\mathrm{mV}$ *and for QD1 and QD3 a joint discontinuity at* $-526\,\mathrm{mV}$ *is observed.*

5.2.3 3D-Model for three quantum dots

A set of three quantum dots is analyzed and the model developed in chapter 5.2.2 is applied. One can extract the energy shifts ΔE, the corresponding gate voltages V_c and the dipole moments $\vec{p}$ of the three quantum dots depicted in Fig. 5.4. By puting V_c in the charging event model (subchapter 2 in 5.2.2) the vertical distances between quantum dot and impurity are computed. With the z as input parameter and the energy shift caused by the impurity the lateral displacement is obtained. These calculations are performed for every impurity so that only one degree of freedom per impurity remains unknown which is the angle ϕ. In summery it is possible to derive a set of three-dimensional pictures of how quantum dots and impurities are located relative to each other. The model was tested for variations of the thicknesses of the sample taken from the growth protocol: for the quantum dot position $z = 25\,\mathrm{nm}$ to $25.5\,\mathrm{nm}$ is assumed and the interface can be at $z = 54\,\mathrm{nm}$ to $55\,\mathrm{nm}$ (for this the wave function center of mass in a triangular potential is evaluated).
In Fig. 5.4 the exciton dispersion curves of three quantum dots are shown. The Stark shift, which is different for all three quantum dots, is subtracted for better legibility. All three quantum dots are observed in one photoluminescence experiment at the same time, meaning that they are within one common laser focus (inset of

Fig. 5.4). By this it is guaranteed that dots 2 and 3 are within a radius of $\approx 500\,\mathrm{nm}$ from the central quantum dot 1. This implies that there should be impurities which affect at least two or even all three quantum dots. For the InGaAs quantum dots in the wavelength regime shown here typical dipole moments are around $-e \times 0.25\,\mathrm{nm}$ [45]. They are $-e \times 0.180\,\mathrm{nm}$ (QD1), $-e \times 0.252\,\mathrm{nm}$ (QD2) and $-e \times 0.208\,\mathrm{nm}$ (QD3). With this we can extract from the data energy shifts in the range of $7\,\mu\mathrm{eV}$ - $38\,\mu\mathrm{eV}$ (compare table below).
Firstly it is investigated how carbon impurities affect the behavior of the excitonic dispersion relation of a neutral exciton and the model is tested quantitatively. Impurities could be located in the superlattice which forms the blocking barrier of the sample, at the interface of the superlattice or within the 30 nm GaAs-tunneling barrier above the quantum dot layer. Carbon forms an acceptor state within the band gap of GaAs being about 26 meV offset from the valence band. Applying the model for the $38\,\mu\mathrm{eV}$ energy shift (QD3) a maximum distance (on axis) of 24 nm between the quantum dots and the impurity is calculated. This value is an upper bound as any radial displacement from the axis of the quantum dot dipole diminishes the interaction between the charge and the dipole. The distance between the quantum dot layer and the superlattice is 30 nm according to the growth protocol. Therefore the results of this simple estimate of energy shifts in terms of the distance between quantum dot and impurity clearly contradicts any model ascribing the position of the impurities either to positions within the superlattice or at the interface of the superlattice.
The basic assumption is now that carbon impurities are embedded in the 30 nm thick GaAs layer which is above the quantum dot layer (along the growth direction). For all jumps observed in Fig. 5.4 the vertical and lateral distances between quantum dot and impurity are computed:
The z-values are extracted from the hole-2DHG-resonances and are independent from the electric field. ρ is then unambiguously computed from the energy shift and the vertical distance. Coincidences of discontinuities in the exciton dispersion of the three quantum dots can be found. Two impurities (at $-525\,\mathrm{mV}$ and $-488\,\mathrm{mV}$) interact with two quantum dots. That means that the quantum dots need to be very close to each other: QD1 and QD2 are 37 nm apart from each other and between QD1 and QD3 there is a distance of 35 nm. Both values are fairly low as typical radiuses are $10\,\mathrm{nm} - 15\,\mathrm{nm}$ for this kind of quantum dots. Nonetheless smaller quantum dot diameters are also observed in [42]. From the information in the table spatial configurations can be generated how the quantum dots and impurities are located relative to each other as it is depicted in Fig. 5.8. The gate voltage range $-600\,\mathrm{mV}$ to $-380\,\mathrm{mV}$ of the quantum dots defines two planes perpendicular to the growth axis within which impurities can be detected due to a charging event. The boundaries in the lateral detection range is set by the linewidth of the exciton resonance. Any energy shift below $5\,\mu\mathrm{eV}$ cannot be detected. Impurities which are in a cylinder whose plains are defined by $z = 40.8\,\mathrm{nm}$ and $z = 42.3\,\mathrm{nm}$ and whose radius is 30 nm are detected by the quantum dot. The maximal energy shifts the

	V_c	ΔE	z	ρ
QD1	−570 mV	7 μeV	42.1 nm	27 nm
QD1	−525 mV	12 μeV	41.9 nm	22 nm
QD1	−488 mV	17 μeV	41.6 nm	19 nm
QD2	−588 mV	28 μeV	42.2 nm	17 nm
QD2	−488 mV	25 μeV	41.6 nm	18 nm
QD3	−525 mV	38 μeV	41.9 nm	13 nm

Table 5.1: *Coordinates of the impurities relative to the quantum dots from Fig. 5.4. The ones with identical V_c refer to one common impurity for two quantum dots. The calculation is implemented for charging events of carbon atoms.*

quantum dots can show are 80 μeV (QD1), 113 μeV (QD2) and 94 μeV (QD3) corresponding to their different dipole moments. In order to check whether silicon can be made responsible for the observed jumps the boundaries for the 38 μeV jump are tested. Assuming positions only on axis with the quantum dot the charging model requires that the impurity is 24 nm to 24.15 nm apart from the quantum dot which corresponds to an maximum energy shift of 7 μeV. All observed discontinuities have larger energy shifts and therefore silicon can be excluded as a charging site.

5.3 Extensions of the model

In chapter 5.2 two simple models are combined and applied to a set of three quantum dots in sample 1. The model give a fairly good agreement with the experimental observations. Nonetheless some features can not be explained by them and require an extension. The additional application of a non-resonant laser can "switch off" the charging characteristics in the exciton dispersion curve. In this chapter it is also shown that lateral charge sensing between different quantum dots can be excluded as a mechanism causing the jumps.

5.3.1 Charge sensing under non-resonant excitation

In Fig. 5.5(a) the plateau of the neutral exciton is shown which is measured in differential transmission. In contrast in Fig. 5.5(b) and (c) an additional non-resonant laser with $\lambda = 850$ nm is applied. The excitation energy is below the band gap of GaAs and therefore electron-hole pairs are only generated in the wetting layer. In 5.5(b) the non-resonant laser has a power of 0.002 nW. The discontinuities are dramatically altered in energy and the contrast is almost fully recovered on the

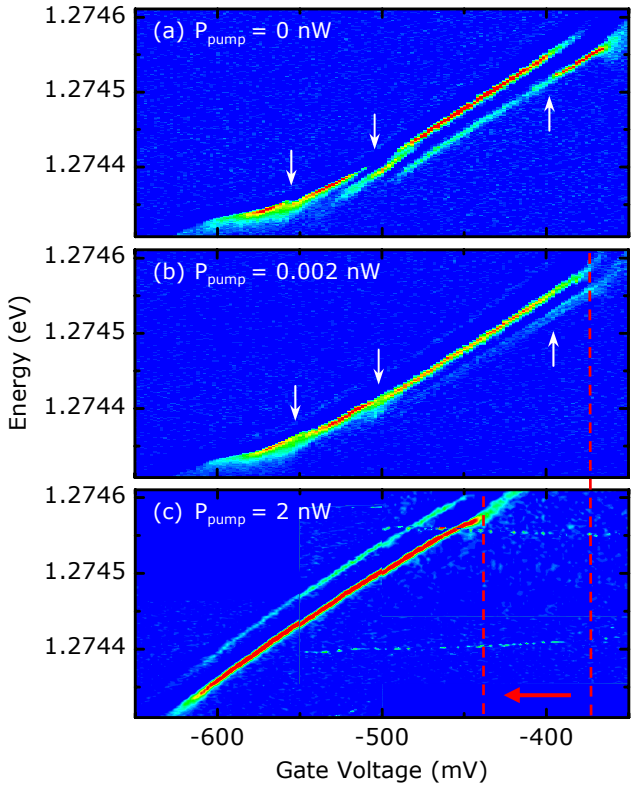

Figure 5.5: *(a) Exciton plateau of quantum dot 1 (Fig. 5.2). (b) Additionally to the resonant laser a non-resonant pump laser with a low laser power $P_{pump} = 0.002\,\mathrm{nW}$ is applied. The jumps are still visible but the energy displacements are diminished. (c) For high pumping powers ($P_{pump} = 2\,\mathrm{nW}$) the expected linearly shifted exciton dispersion is fully recovered. The photo-generated charges saturate the impurities and create a screening field leading to a shift of the plateau in gate voltage (indicated with red dashed lines).*

unperturbed resonance. If the laser power is further increased up to 2 nW no jumps can be observed any more in the exciton dispersion. It features the usual Stark shift and hybridization at the edges of the plateau (chapter 6). This behavior can be explained by considering the band diagram of the sample. Both electrons and holes which are created in the wetting layer can tunnel out of the layer. Due to the present electric field the electrons tunnel out of the quantum dot and are absorbed in the fermi sea of the back contact. On the other hand the holes are pulled towards the opposite direction and are trapped at the interface to the superlattice occupying states in the 2D hole gas. Due to the enhanced population of states in the hole gas tunneling of holes into the impurity states is favored over tunneling out of it. At large laser powers this leads to an entire saturation of carbon states in the GaAs capping layer which are responsible for charging events detectable by the quantum

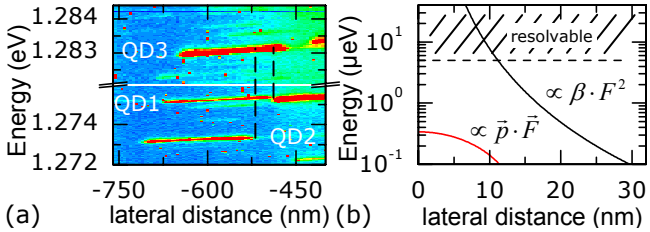

Figure 5.6: *(a) Photoluminescence map of QD1, QD2 and QD3. The neutral exciton lines of the three quantum dots are labeled. For lateral charge sensing one would expect that a discontinuity in QD3 is visible where the transition from the neutral to the charged exciton takes place for QD1 and QD2. (b) Model calculations taking into account a polarizable quantum dot in the electric field of a point charge. Distances of less than* 11 nm *between quantum dots are required to achieve energy shifts which are detectable with the available system (dashed line identifies detection resolution).*

dot. Therefore impurity effects cannot be observed any more at $P_{nr} = 2\,\mathrm{nW}$ - they are switched off. Besides in Fig. 5.5(c) the whole plateau is shifted in gate voltage by about 60 mV (compare red dashed lines in Fig. 5.5). Since holes accumulate at the interface and electrons are withdrawn from the sample an additional electric field is induced with opposite direction. The induced field hence acts as a screening field for the quantum dot leading to a reduced overall electric field. In consequence the whole exciton dispersion curve is shifted in gate voltage and not in energy.

5.3.2 Lateral dot-dot sensing

The models used up to now are based on the interaction between the quantum dot exciton and charges mainly being apart from each other along the growth axis. Nonetheless there is a second spatial configuration which allows charge sensing. If charging occurs in the quantum dot layer an effect on the exciton energy should also be visible. One could also think of a situation in which a quantum dot can detect the charging event of a second quantum dot close by. This happens at the transition point from the neutral exciton to the charged exciton as one electron tunnels into the second quantum dot and changes the overall electric field at the first quantum dot. Fig. 5.6 (a) shows that the neutral exciton plateaus (and therefore the X^0 to X^- transition) shift in photoluminescence to higher gate voltages with increasing energies. So for example QD1 should have a jump at the gate voltage at which the plateau of QD2 ends. The spectra obtained from differential transmission (the spectral resolution of it is orders of magnitude higher) are compared in Fig. 5.4 and neither for the case mentioned nor for any other quantum dot evidence for such an effect can be found.

The energy shift of the exciton can be written in a linear expansion as:

$$\Delta E = -\vec{p}\cdot\vec{F_1} + \vec{p}\cdot\vec{F_2} + \vec{p}\cdot\vec{F_3} + \beta(\Delta F)^2 \tag{5.7}$$

$\vec{p}$ is the dipole moment of the exciton which is basically oriented along the external field $\vec{F}_{ext}$, β is the polarizability of the quantum dot and $\vec{F_i}$ are the electric fields of the impurity charge and its mirror charges at the location of the quantum dot. Since the orientation of the exciton dipole is fixed and perpendicular to the electric field of a charge laterally displaced in the InGaAs layer the first term $\vec{p}\cdot\vec{F_1}$ is 0. The second and third term for the mirror charges are non-zero but their contribution is below 0.4 μeV (see red curve in Fig. 5.6(b)). The polarizability of the quantum dot arises from the fact that an electric field pulls apart the electron and hole in z-direction as the electric field of the dipole has only a z-component in the quantum dot plane. Therefore the polarizability in x-y-plane is neglected. The polarizability of the quantum dots investigated here is $\beta = 0.25\,\frac{\mu\mathrm{eV}}{(\mathrm{kV/cm^2})^2}$ which gives the black curve in Fig. 5.6(b). This implies that the polarization part is dominating and only needs to be considered for lateral charging effects. In Fig. 5.6 (b) the energy shift for lateral distances between 0 nm and 30 nm are computed. Energy shifts down to 5 μeV can be detected with the quantum dot investigated and therefore one can extract that the distance between the charge and the quantum dot needs to be less than 11 nm. From this it can be concluded that it is rather unlikely that the jumps in the exciton dispersion originate from charging events in the quantum dot layer.

5.4 Charge sensing in a modulation doped sample

As a proof of principle another dot in sample 2 (MCV13-2) with a different field effect structure is presented and it is demonstrated that charging events are a general phenomena in self-assembled InGaAs quantum dots. In the previous chapters it is shown that several quantum dots in sample 1 are affected by charging events in their vicinity. The typical charging gate voltages and energy shifts are determined by the composition of the heterostructure itself and the spatial position of quantum dots relative to the impurities. Without loss of generality the electrostatic model can be applied on any other sample with different structure by adapting the sizes of the capacitor to the present sample. In sample 2 the commonly used type of back contact (i.e. a bulk doped quantum well) is substituted with a triangular quantum well grown by δ-doping. A very thin layer is highly doped with silicon. The excess charges migrate to the triangular well with low energy. It hosts the donator electrons and serves as the back contact 25 nm from the quantum dot layer. The distance between the δ-doping and the triangular quantum well is 10 nm. The thickness of the superlattice, which prevents a vertical current through the heterostructure, is changed to 246 nm. This leads to new gate voltage regions in which the neutral and charged excitons live. The capping layers around the quantum dots are identical to

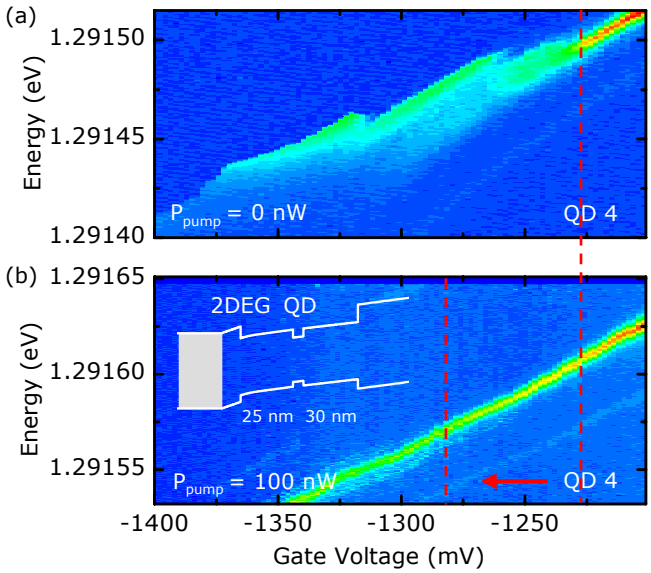

Figure 5.7: *Neutral exciton dispersion of QD4 on MCV13-2 (with modulation doped back contact). (a) A region of the neutral exciton dispersion is displayed which is close to the tunneling regime. The three discontinuities attributed to charging events close to the quantum dot have energy jumps between* $8\,\mu$eV *and* $12\,\mu$eV*. (b) A non-resonant laser with a power of* $P_{nr} = 2\,$nW *is focused onto the sample in addition to the resonant laser. The impurities which are responsible for the jumps in the exciton dispersion are fully saturated by the photo-induced charges. The red dashed line indicates the gate voltage shift due to hole accumulation.*

sample 1 (inset in Fig. 5.7(b)).
In Fig. 5.7 the left edge of the neutral exciton of a quantum dot in sample 2 is shown. 5.7(a) depicts the neutral exciton measured without non-resonant laser excitation. Three charging events shift the resonance energies by $8\,\mu$eV, $12\,\mu$eV and $12\,\mu$eV at $-1237\,$mV, $-1262\,$mV and $-1316\,$mV respectively. As it is already known from QD1 in sample 1 with a non-resonant laser ($\lambda_{nr} = 850\,$nm, $P_{nr} = 2\,$nW) charging events are switched off as the impurities are saturated with photo-generated holes. Moreover holes accumulate in the 2D hole gas at the superlattice and evolve into a metallic layer. Therefore the 2D hole gas acts as an opposite electric field diminishing the overall field which results in a shift in gate voltage of the exciton dispersion curve (indicated by the red dashed lines and the arrow). So far the results on this dot are consistent with the previous dots.
The investigated quantum dot has a dipole moment of $-e\times 0.241\,$nm. The conditions for carbon in the host material are examined. The results are shown in table 5.2. It turns out that carbon can fully explain the observed jumps in the exciton dispersion. For charging of carbon acceptors the range of z is around $45.5\,$nm.

V_c	ΔE	z	ρ
$-1237\,\mathrm{mV}$	$8\,\mu\mathrm{eV}$	$45.4\,\mathrm{nm}$	$29\,\mathrm{nm}$
$-1262\,\mathrm{mV}$	$12\,\mu\mathrm{eV}$	$45.5\,\mathrm{nm}$	$25\,\mathrm{nm}$
$-1316\,\mathrm{mV}$	$12\,\mu\mathrm{eV}$	$45.7\,\mathrm{nm}$	$25\,\mathrm{nm}$

Table 5.2: *z- and ρ-values calculated assuming carbon impurities to be responsible for the jumps.*

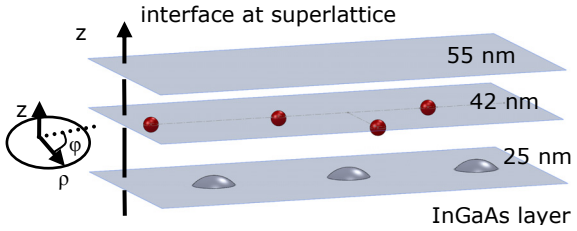

Figure 5.8: *3D-model of the three quantum dots with corresponding impurities assuming that only carbon states participate. This is one possible configuration as the angles φ between the quantum dots and impurity cannot be determined. Impurities are red and the quantum dots are grey.*

5.5 Conclusion

In this chapter charging events and its implications on the quantum dot energy dispersion were investigated. The exciton energy dispersion exhibits discontinuities at distinct gate voltages with energy shifts of several tens of μeV. The discontinuities are caused by charging of an impurity which modifies the local electric field at the quantum dot. Two candidates for the impurities were taken into account: Carbon atoms always exist as a background doping in MBE-grown semiconductor materials and silicon atoms are intentionally introduced into the back contact to form a two-dimensional electron gas. By means of an electrostatic model and models for the charging mechanisms of the impurities relative spatial positions of quantum dot and impurity could be calculated. Therefore in Fig. 5.8 one possible spatial configuration of carbon impurities is depicted (the only free parameter is the angle Φ).
From our models it can be concluded that bulk impurites are the source for the jumps in the exciton energy dispersion. This contradicts the results of Houel et al. which located the trapping sites at the interface to the superlattice. However in our experiments which use an almost identical sample as Houel et al. jumps with energies shifts were observed which require distances smaller than the distance quantum dot layer to superlattice.
The charge sensing mechanism presented in this chapter offers the opportunity to use a quantum dot as a detector for single charges in GaAs-based semiconductor systems. The sensitivity is limited by the linewidth of the resonance (energy shifts below the linewidth are hidden) and depends strongly on the relative position of

quantum dot and charge. In principle every excitonic transition in a quantum dot is sensitive to electric field fluctuations and should be suitable as a detector so that the gate voltage range in which it can be used encompasses several 100 mV.

Chapter 6

Tunnel coupling to an electron continuum of states

In chapter 4 optical transitions in a quantum dot from the ground state to the excited state are explained by a two-level model. This implies that only one excitation and relaxation channel exist. It requires that the quantum dot is isolated from its semiconductor environment which is not true for a real dot system. There are always coupling mechanisms to the solid state matrix in which the quantum dot is embedded - such couplings have been reported with for example nuclear spins [88], phonons [89] or with a Fermi sea [35].
In this chapter a case is shown in which the approximation of an isolated two-level system fails. In the back contact of the samples a Fermi sea of electrons is established. That means a bath of quasi-free electrons is nearby the quantum dot and can interact with it. The coupling is mediated by tunneling of electrons between electron bath and quantum dot states and is modeled as hybridized state consisting of the quantum dot state and the reservoir states.
The coupling of a Fermi reservoir to a quantum dot has already been studied in photoluminescence on a negatively charged exciton by Dalgarno et al. [30]. In this work the focus lies on the neutral exciton which is probed with differential transmission spectroscopy.

6.1 The energy dispersion relation of the exciton

The sample which is used in the experiments here is of the standard composition as it is presented in chapter 2.2. The tunneling barrier, consisting of GaAs, between the back contact and the quantum dot layer is nominally 25 nm. Due to the thicknesses of the barrier in this case the coupling between the quantum dots and the Fermi reservoir is rather weak [35]. The dots are in the weak coupling regime [31]

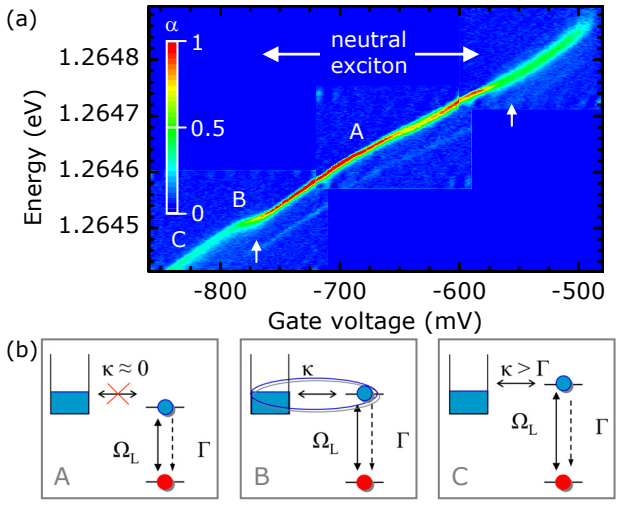

Figure 6.1: *(a) Plateau of the neutral exciton measured in DT. The stable exciton regime is between* −780 mV *and* −580 mV *(labeled A). Beyond this region tunneling of electrons reduces the contrast and causes a broadening of the linewidth (label C). B is the hybridization region where the tunneling sets in and a red-shift in energy is present. (b) Schematics corresponding to the labels in (a). In the stable exciton regime the quantum dot transition can be treated as an isolated two-level system. In the hybridization regime the final state is a superposition of continuum states and the quantum dot state and in the tunneling regime the resonance is dominated by the tunnel broadening.*

and the effects on the optical response due to the tunneling can be expected to be not very pronounced.

A single quantum dot with an exciton resonance of the X^0 at about 980 nm and of the X^- at about 985 nm is chosen for the following experiments (same quantum dot as in chapter 4.1/ Fig. 4.1). In photoluminescence experiments no signs of hybridization could be demonstrated in contradiction to what was demonstrated in reference [30] on the X^-. This is not surprising since the quantum dots used in [30] are blue dots at around 908 nm. A large transition energy of the exciton means that the electron confinement is much shallower than for the low-energy (red) quantum dots and therefore the tunnel coupling to the electron reservoir is much stronger in blue quantum dots. This can be directly rendered into stronger hybridization signatures for blue dots. Likewise on the charged exciton no asymmetries and broadening of the linewidth is observed in non-resonant PL measurements.

In Fig. 6.1(a) the neutral exciton plateau of the quantum dot at 980 nm is shown. Single spectra are recorded in differential transmission by tuning the laser energy at a fixed gate voltage. The spectra corresponding to a series of voltages from −480 mV to −600 mV, −590 mV to −720 mV and −710 mV to −860 mV are each put together

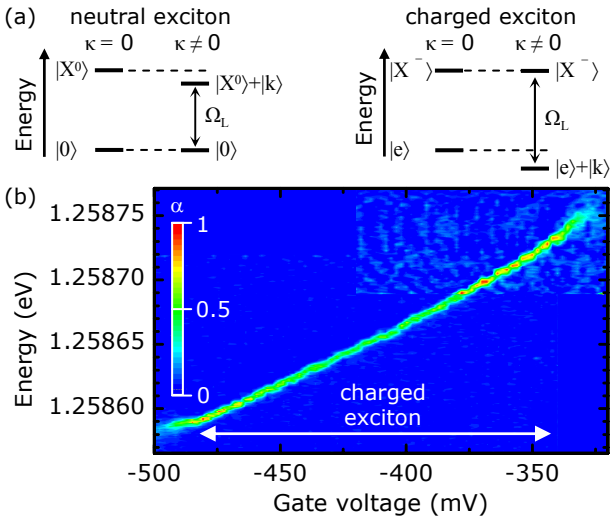

Figure 6.2: *(a) Difference of the energy shifts for the neutral and charged exciton. Due to the hybridization of states the energies of the final state (X^0) or the initial state (X^-) are reduced causing a red or blue shift, respectively. (b) Hybridization effect at the charged exciton. On both edges a blue shift appears.*

into a 2D-colorplot with color-coded absorption contrast. The plateau exhibits the well-known linear Stark effect with $\Delta E/\Delta V = 1.26\,\mu\text{eV/mV}$. On both edges of the exciton plateau a significant decrease of absorption strength, an increase in linewidth and a kink in the resonance energy are visible. The decrease of the absorption and the linewidth broadening are caused by the tunneling of electrons into the electron bath which sets in at the Fermi energy on the left side of the plateau. On the right side of the plateau an electron starts to tunnel into the quantum dot in the ground state and leads to a change in absorption. In both cases the tunneling dominates over the spontaneous recombination. The kinks observed at $U_g = -780\,\text{mV}$ and $U_g = -550\,\text{mV}$ are signatures of hybridization due to tunneling. They introduce a red-shift (i.e. shifted to lower energies) close to the tunneling regime (left edge) or the X^--regime (right edge), respectively. From the kinks an approximate red shift of $13\,\mu\text{eV}$ ($20\,\mu\text{eV}$) on the left edge (right edge) of the plateau can be extracted.
For each of the three regimes stable exciton, hybridization and tunneling a simple picture. The physical mechanisms are identical for both the region where the transition from the neutral exciton to the tunneling regime occurs and the region where X^0 and the negatively charged exciton X^- coexist. Here the left edge is analyzed exemplarily. In the regime of a stable neutral exciton interactions between the Fermi sea and the quantum dot are negligible (Fig. 6.1(b) picture A). The initial state for absorption is an empty quantum dot which can be written as the quantum dot ground state $|0\rangle$. A laser photon, which is resonant with the lowest optical transition, is scattered at the quantum dot and creates with the Rabi frequency Ω_L an

electron-hole pair. As the state of the electron is substantially below the Fermi energy no tunnel coupling is present resulting in a coupling constant $\kappa \approx 0$. Therefore the exciton is localized in the quantum dot potential and the linewidth is dominated by the decay rate Γ (equation 4.25). By tuning the quantum dot towards the Fermi energy the exciton dispersion undergoes a transition from the purely localized exciton to the hybridization regime which is depicted in Fig. 6.1(b) picture B. Here the electron in the $|\mathrm{X}^0\rangle$-state is coupled to the electron reservoir via tunneling with rate κ and a new hybrid state forms. The transition takes place when the occupied electron level of the quantum dot comes into resonance with the Fermi energy. A consequence of the tunneling is an energy renormalization of the electron state to lower energies as is shown in Fig. 6.2(a). This is only the case for the excited state $|X^0\rangle$ as there is a single electron in the quantum dot. The ground state $|0\rangle$ is unchanged so that the exciton resonance is red-shifted when tunneling processes come into play. In the tunneling regime (Fig. 6.1(b) picture C) at high electric fields the electronic state of the quantum dot is clearly above the Fermi level. Therefore the tunneling of the electron out of the quantum dot in the Fermi sea after absorption of a photon dominates the behavior of the system and strongly affects its optical response. As the coupling constant κ is larger than the natural linewidth Γ of the single quantum dot transition the linewidth of the optical resonance is mainly determined by the tunnel broadening.
In [30] hybridization is shown on the negatively charged exciton. Nonetheless on the quantum dot investigated here no signature of hybridization can be found in photoluminescence. However in differential transmission this changes. Fig. 6.2(b) depicts the X^--plateau. A kink can be clearly recognized at $-490\,\mathrm{mV}$ which is blue-shifted by about $12\,\mu\mathrm{eV}$. The shift arises also from hybridization in this case of the electron ground state $|\mathrm{e}\rangle$. On the right edge of the charged exciton plateau there is also a blue-shifted kink caused by hybridization.
Fig. 6.2(a) explains the difference between the X^0-case and the X^--case and why there is a red-shift for the X^0 and a blue-shift for the X^-. In the neutral exciton case only the excited state has an electron which can interact with the continuum of states $\sum_k |\mathrm{k}\rangle$ in the Fermi sea. The hybridized state experiences always an energy normalization to lower energies so that the overall transition energy becomes smaller because the upper state is changed. The charged exciton undergoes a blue-shift as only the lower state is hybridized which is the single electron state. The upper state $|\mathrm{X}^-\rangle$ has two electrons nevertheless there is no hybridization because the exciton energy is far below the Fermi edge and therefore tunneling is weak [35].

6.2 The Anderson model

The Anderson model describes the interaction between a many-body system and few localized states. One example of a physical problem to which it applies is the Kondo

effect [32, 90]. In this chapter the Anderson hamiltonian is only presented and its different parts are explained. It is given without derivation and follows reference [91].
Here the hamiltonian is considered for the classic Kondo system: a metal with magnetic impurities. Nonetheless this does not limit the generality of the hamiltonian and can be extended to similar systems. The Anderson hamiltonian consists of four terms with three of them giving the independent energies of the conduction band and the localized states. The fourth term describes the interaction between impurity and conduction electrons. The hamiltonian appears as follows:

$$H_{Anderson} = H_{Fermi-sea} + H_{impurity} + H_{on-site} + H_{tunneling} \tag{6.1}$$

The first term in equation 6.1 represents the Fermi sea of electrons in the conduction band of the metal and the second term is identified as the energy of the impurity states. Term number three in 6.1 refers to the on-site interaction between the states in the impurity which is basically given by Coulomb and Pauli repulsion of the electrons. The interaction between the electronic states in the Fermi sea and the impurity states (term four) is modeled as a tunneling mechanism. So the exchange of spin is mediated by an electron hopping on or off the impurity site. This fourth part of the Anderson hamiltonian is also called hybridization term as it couples the two independent systems and is the source of many-body effects in the composite system.
For the case of a single impurity which constitutes a spin-1/2 system the Anderson hamiltonian simplifies as the on-site interaction is zero.

6.2.1 Hybridization of a quantum dot with the Fermi reservoir

In this chapter a model for hybridization is derived based on the assumption that the tunnel coupling modifies ground or excited state of the optical transition. The tunnel coupling is treated quantum mechanically in form of the Anderson hamiltonian introduced in chapter 6.2. For simplicity the Fermi sea is supposed to be frozen meaning that excitations do not play a role. Here only the case of the neutral exciton is discussed, however the model also applies without limitations for the charged exciton. The derivation follows the work of Dalgarno et al. [30].
The unperturbed neutral exciton system consists of the empty ground state $|0\rangle$ and of the exciton state $|X^0\rangle$ which is given by an electron in the conduction band and an hole in the valence band. The two charges are Coulomb-bound i.e. there is an attractive interaction between the opposite charges.
Hybridization can be modeled as a two-level transition with a modified final state $|f\rangle$ instead of the pure quantum dot state $|X^0\rangle$. In the model for the absorption experiments a photon drives the optical transition from the ground state $|0\rangle$ into the

modified final state $|\mathrm{f}\rangle = \mathrm{A_X}|\mathrm{X}^0\rangle + \sum_\mathrm{k} \mathrm{A_k}|\mathrm{k}\rangle$ with $|\mathrm{k}\rangle$ being continuum states of the Fermi reservoir (A_X and A_k are the coefficients). The operator of the optical transition (i.e. the dipole operator) can be written as $D = dc_X^\dagger c_p$ where $c_X^\dagger$ is the exciton creation operator and c_p is the photon annihilation operator. The transition matrix elements take the form $|\langle 0|D|\mathrm{X}^0\rangle|^2 = |\mathrm{D}|^2$ and $|\langle 0|D|\mathrm{k}\rangle|^2 \approx 0$. The second matrix element is vanishingly small as the direct transition into the electron continuum is very weak. Otherwise Fano resonances would appear in the transmission signal [92] which could not be observed. The energy of the initial state $|0\rangle$ is E_i, of the exciton state $|\mathrm{X}^0\rangle$ it is E_X, the energy E_k corresponds to the continuum states $|\mathrm{k}\rangle$ and the final state $|\mathrm{f}\rangle$ has the energy E_f. It is related to the Anderson hamiltonian H_f via the Schrödinger equation $H_f|\mathrm{f}\rangle = \mathrm{E_f}|\mathrm{f}\rangle$. The Anderson hamiltonian for this system is given by

$$H_f = E_X c_X^\dagger c_e + \sum_k E_k c_k^\dagger c_k + \sum_k \left(V_k c_k^\dagger c_e + V_k^* c_e^\dagger c_k \right) \tag{6.2}$$

It uses the single impurity version of the Anderson hamiltonian (equation **??**). The electron acts as the single impurity which interacts with the many-body system Fermi sea. As there is only one electron in the quantum dot no on-site interaction exists. The first two terms describe the unperturbed quantum dot and electron continuum. The $c_X^\dagger$ and c_X are the electron creation and annihilation operator for the quantum dot and $c_k^\dagger$ and c_k are the creation and annihilation operator for the continuum of states. The tunnel interaction is described by the third term with the tunneling operator V_k.
The optical response $\alpha = \Delta T/T$ of the quantum dot is calculated by starting with Fermi's golden rule:

$$\alpha = \sum_f |\langle f|D|0\rangle|^2 \delta\left(E_i - E_f - \hbar\delta\omega\right) \tag{6.3}$$

A laser detuning $\delta\omega$ is introduced in the Dirac δ-function. In ideal systems the transition linewidth is infinitely small but in real system like the quantum dot it has a finite width Γ. Therefore the δ-function is substituted with the Fourier transform of a Lorentzian function $\frac{1}{\Pi}\mathrm{Re}[\int_0^\infty \exp(\mathrm{i}(\mathrm{E_i} - \mathrm{E_f} - \hbar\delta\omega)\mathrm{t} - \Gamma\mathrm{t})\mathrm{dt}]$ to account for the real lineshape in DT. Equation 6.3 transforms then into:

$$\alpha = \frac{|D|^2}{\Pi}\mathrm{Re}\left[\frac{\mathrm{i}}{\mathrm{E_i} - \mathrm{E_f} + \hbar\delta\omega + \mathrm{i}\Gamma}\right] \tag{6.4}$$

If the quantum dot behaves like an isolated system, meaning there is no tunnel coupling present, the final state is the neutral exciton with the energy E_X. Therefore the contrast acquires the same form as can be calculated from the optical Bloch equations for a two-level system (chapter 4.2).

$$\alpha = \alpha_0 \,\mathrm{Im}\left[\frac{1}{-\hbar\delta\omega + \sigma\Delta\mathrm{V_g} - \mathrm{i}\Gamma}\right] \tag{6.5}$$

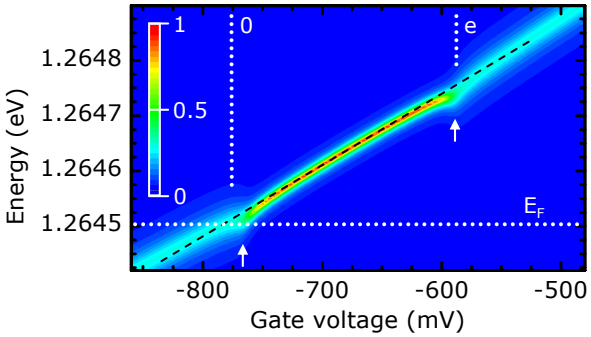

Figure 6.3: *Simulation of the hybridization effect for the neutral exciton from Fig. 6.1(a). A red-shift in the hybridization region can be reproduced with the model using equation 6.7. From the calculation a tunneling rate* $\kappa = 20\,\mu\mathrm{eV}$ *can be extracted.*

σ is the Stark shift and ΔV_g is the voltage detuning relative to the Fermi level. In case of a coupling to the Fermi reservoir the energy E_f is defined by the Schrödinger equation with the Anderson hamiltonian (equation 6.2). E_f is modified and can be written as $E_X + E_t$ with

$$E_t = \sum_k \frac{|V_k|^2}{\hbar\delta\omega + E_i - E_k - i\Gamma_0} \tag{6.6}$$

The modified contrast for the hybridization case has only an additional energy term κA_1 (derived from E_t) in the denominator which shifts the resonance energy:

$$\alpha = \alpha_0 \,\mathrm{Im}\left[\frac{1}{-\hbar\delta\omega + \sigma\Delta\mathrm{V_g} - \mathrm{i}\Gamma + \kappa\mathrm{A_1}}\right] \tag{6.7}$$

The tunneling energy is $\kappa \propto |V_k|^2$ and $A_1(\delta\omega, \Delta V_g)$ is the coupling function. A number of approximations and assumptions are made to be able to evaluate the function $A_1(\delta\omega, \Delta V_g)$. All measurements are carried out at finite temperatures so the interaction range in energy between the Fermi sea and the electron state of the exciton is determined by a bandwidth $W = 60\,\mathrm{meV}$. Over this bandwidth the coupling $|V_k|^2$ is assumed to be constant. This implies that $\sum_k$ can be substituted by an integral $\int_{-E_f}^{-E_f+W} d\epsilon$. Thus the Fermi sea can be interpreted as a frozen electron reservoir. The energy of the initial state in A_1 is set in relation to the Fermi energy therefore it can be written as $e\Delta V_g/\lambda$ in equation 6.6. The occupation of the Fermi sea is given by the Fermi-Dirac distribution $f_F(E) = (exp(E/k_BT) + 1)^{-1}$.

$$\begin{aligned} A_1(\delta\omega, \Delta V_g) = \frac{1}{\Pi}\int_{-E_f}^{-E_f+W} \{&\frac{\hbar\delta\omega - \Delta V_g/\lambda - \epsilon - i\Gamma_0}{(\hbar\delta\omega - \Delta V_g/\lambda - \epsilon)^2 + \Gamma_0^2}(1 - f_F(\epsilon)) \\ &+ \frac{\hbar\delta\omega + \Delta V_g/\lambda + \epsilon - E_{ee} - i\Gamma_0}{(\hbar\delta\omega + \Delta V_g/\lambda + \epsilon - E_{ee})^2 + \Gamma_0^2} f_F(\epsilon)\} d\epsilon \end{aligned} \tag{6.8}$$

The first term in the coupling function 6.8 accounts for the hybridization on the left edge of the X^0 where the electron can tunnel out of the dot and a single hole resides confined in the valence band. The second term treats the case on the right edge of X^0. An electron tunneling into the quantum dot transforms the original exciton state in singly negatively charged exciton.
Fig. 6.3 shows the calculated plateau of a neutral exciton. The parameters for the experimentally investigated quantum dot from Fig. 6.1(a) were used. The Fermi energy is at about $-780\,\mathrm{meV}$, the Stark shift is $\Delta E/\Delta V = 1.26\,\mu\mathrm{eV/mV}$, $E_{ee} = 29\,\mathrm{meV}$ (from chapter 4.1) and $\Gamma = 7\,\mu\mathrm{eV}$. The only parameters which are varied are the tunneling energy κ and the electron relaxation in the Fermi reservoir Γ_0. They are found to be $\kappa = 20\,\mu\mathrm{eV}$ and $\Gamma_0 = 300\,\mu\mathrm{eV}$ (which fits well with the thermal energy at $4.2\,\mathrm{K} \approx 360\,\mu\mathrm{eV}$). A comparison of Fig. 6.3 and 6.1 shows that the alteration of the absorption beyond the neutral exciton plateau is nicely reproduced. Likewise a red-shift on both sides belonging to hybridization can be simulated. In the calculation only a linear Stark effect is considered. In the experiment there seems to be a slight additional bending which could be attributed to the quadratic Stark effect. The theory also assumes a symmetric distribution of κ around the Fermi energy (or the transition point to the X^-) of the coupling function. This doesn't seem to be the case in this quantum dot as the interaction region to higher energies is larger than to lower energies. Besides this a fairly good agreement between theory and experiment can be achieved.

6.3 Hole tunneling and suppressed hole tunneling

If the quantum dot is probed in the tunneling regime it cannot be expected to observe absorption. Due to fast tunneling of electrons out of the quantum dot no optical recombination of the electron and the hole can occur any more. Furthermore the resident hole in the quantum dot prevents any subsequent resonant excitation as the transition energy is Coulomb-shifted.
The sample presented here uses a structure which allows the remaining hole to leave the quantum dot and to allow further excitations of the system. A layer of GaAs (thickness 30 nm) is located between the quantum dot layer and the superlattice (chapter 2.2). Due to the bias applied at the sample a quantum well with a delta potential forms at the interface between the GaAs and the superlattice which hosts a two-dimensional hole gas. Consequently the remanent hole in the quantum dot has a finite probability to tunnel into the 2DHG. This gives rise to a recovery of the resonantly driven optical transition into the excited state of the quantum dot. The existence of the two-dimensional hole gas in our samples is confirmed by the observation of oscillations in the linewidth of the excitonic dispersion curve in the tunneling regime as reported previously [79].
In Fig. 6.4(a) the schematic illustrates the processes involved. A photon creates an

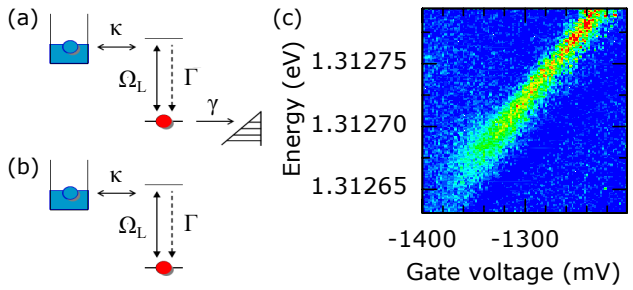

Figure 6.4: *Schematics for the processes involved in the tunneling regime for a sample with (a) and without 2D hole gas (b). In (a) the remanent hole tunnels out and allows subsequent optical excitation. As no 2DHG exists the hole remains in the quantum dot and blocks optical excitation. (c) Example of a neutral exciton from a sample without 2DHG.*

electron-hole pair in the quantum dot. As the electron level is substantially above the Fermi level the electron tunnels out of the quantum dot and it is now in the $|h\rangle$-state (chapter 4.1). From the diagram in Fig. 4.1(b) one can see that the energy of the hole state is shifted to lower energies compared to the X^0. So the laser is not resonant with the quantum dot any more and no absorption of photons takes place. The energy difference is given by $\Delta E(\mathrm{X^0 - h}) = \mathrm{E_\lambda(V_g) + E_C + E_m + E_{eh}}$ (from equations 4.1). The triangular potential at the interface of the superlattice gives rise to a discrete level structure with a finite density of states at approximate energies $E_V - E(2DHG) = E_V - c_n[(e\hbar)^2/(2m)F_{SL}^2]^{1/3}$ with the Airy coefficient c_n and $F_{SL} = (V - V_S)/175\,\mathrm{nm}$ being the electric field at the quantum well [93]. Hole tunneling is partially suppressed as long as the hole state of the quantum dot is not resonant with an hole gas level. If $E(2DHG)$ is resonant with $E(h)$ the tunneling rate reaches its maximum. So the holes can tunnel out of the quantum dot and allow reexcitation. A consequence of the selectivity of the hole tunneling on the resonance condition is that on resonance the overall tunneling rate $\kappa + \gamma$ (κ/ γ account for the electron/ hole tunneling rate) is increased. Since the tunneling dominates over the spontaneous emission the linewidth of the DT shows oscillations with maxima on resonance. A calculation of the 2DHG-levels and the hole energies of the quantum dot confirms this correlation.

In Fig. 6.4(c) the left edge of a neutral exciton is shown. Below $V_g = -1360\,\mathrm{mV}$ no absorption can be found any more and Fig. 6.4(b) describes the situation. This quantum dot is measured in a sample with a slightly changed heterostructure which is identical to the sample presented previously except that the layer between the quantum dots and the superlattice is 10 nm. That means that the triangular potential well at the interface is too shallow to form a two-dimensional hole gas. Therefore there are no states to tunnel into so that the resonant excitation is blocked due to the resident hole in the quantum dot.

6.4 Conclusion

In this chapter hybridization effects on the neutral and singly charged exciton were demonstrated for a weakly coupled quantum dot. The typically linearly Stark shifted exciton plateau experiences at the edges an energy shift due to a modification of one contributing state. For the X^0 the final state and for the X^- the initial state consist of a superposition of the electronic quantum dot state with the continuum of states in the back contact.
The hybridization can be simulated by the using the Anderson hamiltonian describing tunneling effects between impurity states and a many-body system. The tunneling is relatively weak and therefore it can be treated as a modification of the optical response of a unperturbed quantum dot system. The experimentally obtained data can be reproduced with the hybridization model.
The hybridization is an interaction between a single two-level system (quantum dot) and a many-body system (Fermi sea of electrons). The experiments shown here are carried out at 4.2 K. According to the theory [94] hybridization is a high temperature analogue of the Fermi-edge singularity which has been demonstrated in quantum wells [34]. Recently Haupt et al. [33] have published the observation of this phenomena in a strongly coupled quantum dot. In their sample they have a strong competition between two transition paths which leads to a Fano interference.

Chapter 7

Cotunneling with the electron spin reservoir

During the past years the negatively charged exciton X^- in self-assembled InGaAs quantum dots has evolved into a standard system for spin preparation and manipulation in low-dimensional semiconductor structures [95, 23]. The charged exciton can be obtained if a single electron is trapped in the quantum dot. The singly charged quantum dot represents the ground state and the excited state is the charged quantum dot exciton. Therefore the excited state consists of two electrons and one hole. According to the fermionic character of electrons and holes in semiconductors the ground state has spin $\pm\frac{1}{2}$ and the excited state has spin $\pm\frac{3}{2}$. A profound knowledge about the optical and non-radiative transitions and about their corresponding rates in the X^--system is available [28].
One approach to investigate populations of the dot states is to apply a magnetic field at temperatures below 1.5 K leading to a spin splitting. By measuring the absorption contrast α at different magnetic fields and temperatures one can gain information about transition rates. If the rates are known it is possible to determine the temperature of the electron bath. The bath temperature is of interest for instance for the Kondo effect [35].
In this chapter the optical Bloch equations are derived and solved for a 4-level system. With the resulting density matrix elements detailed predictions about the absorption properties (measured as contrast α) in magnetic fields can be given. Experiments at mK-temperatures are of special interest in the context of electron spin populations as the contrast of the high-energetic branch should dominate significantly compared to the low-energy branch. Therefore calculations at 4.2 K, 1.5 K and 250 mK are performed to check the temperature dependance of the quantum dot contrast. It is also necessary to distinguish between the spin-pumping regime and the cotunneling-limited regime governed by the ratio of transition rates between the exciton states and the electron states, respectively. In chapter 7.2 the theoretical

predictions are tested on a single quantum dot in the cotunneling-limited regime.

7.1 Optical Bloch equations for a four-level system

For the mathematical description of the X^- a four-level system is taken into account consisting of two electron states $|\uparrow\rangle$ and $|\downarrow\rangle$ and two exciton states $|\uparrow\downarrow,\Uparrow\rangle$ and $|\uparrow\downarrow,\Downarrow\rangle$. At a magnetic field $B = 0\,\mathrm{T}$ the electron and the exciton states are degenerate. Nonetheless they can be addressed individually by choosing circularly polarized light. For the optical transition from $|\uparrow\rangle$ to $|\uparrow\downarrow,\Uparrow\rangle$ ($|\downarrow\rangle$ to $|\uparrow\downarrow,\Downarrow\rangle$) a σ^+ (σ^-) photon is necessary since the change of total angular momentum is $\Delta j = 1$ ($\Delta j = -1$).
At finite magnetic fields the degeneracy is lifted and both the electron and the exciton states split up which leads to four energetically distinct states. The splitting is given by the Zeeman energy $E_Z^{e/h} = g_{e/h}\mu_B B$ where $g_{e/h}$ is the electron or hole g-factor and μ_B is Bohr's magneton. The resulting level scheme is shown in Fig. 7.1.
In principle one could only consider a three-level system to get a full description of the physical processes. However in the experiments presented here, linearly polarized light is used which requires to incorporate both σ^+ and σ^- components of the light at the same time.
In this subchapter only general couplings and transition rates are considered. The underlying physical processes are treated in the following subchapters. For simplicity the levels are renamed: $|1\rangle = |\uparrow\rangle$, $|2\rangle = |\downarrow\rangle$, $|3\rangle = |\uparrow\downarrow,\Downarrow\rangle$ and $|4\rangle = |\uparrow\downarrow,\Uparrow\rangle$ As Fig. 7.1 depicts, the states $|1\rangle$ ($|2\rangle$) and $|4\rangle$ ($|3\rangle$) are coherently coupled by an externally applied laser field with the Rabi frequency Ω_+ (Ω_-) corresponding to σ_+ (σ_-) light. The spontaneous relaxation of $|4\rangle$ and $|3\rangle$ are given by $\Gamma_{41} = \Gamma_{32} = \Gamma_0$ with the natural linewidth Γ_0 of the decay. The natural linewidth is linked to the lifetime τ_X of the exciton by $\Gamma_0 = 1/\tau_X$. Additionally the electron states are coupled by the Fermi contact hyperfine interaction represented by the hamiltonian [96, 97]

$$\hat{H}_{hf} = \frac{\nu_0}{2}\sum_j A^j |\Psi(\mathbf{r}_j)|^2 \left(2\hat{I}_z^j\hat{S}_z^e + \hat{I}_+^j\hat{S}_-^e + \hat{I}_-^j\hat{S}_+^e\right) \tag{7.1}$$

ν_0 is the volume of one unit cell, A^j is the hyperfine constant, Ψ is the electron wave function, $\hat{I}^j$ and $\hat{S}$ are the spins of the jth nucleus and electron spin, respectively. In a quantum dot there are about 10^4 - 10^5 nuclei contributing to the hyperfine interaction with one electron. Due to fluctuations of the nuclear spins a total magnetic polarization emerges which is treated as an effective magnetic field B_N (Overhauser field). In this mean-field approximation in $\hat{H}_{hf}$, only the $\hat{I}_z^j\hat{S}_z$ term is left over which corresponds to the fluctuation part of the hyperfine interaction. The magnetic field can be written as $B_N \propto \frac{\bar{A}}{g_e\mu_B}\langle\hat{I}_z\rangle$ and $\hbar\Omega_N = g_e\mu_B B_N$ [29, 28]. As the fluctuations vanish in the time average there is no effective electron spin flip and therefore this contribution leads to population oscillations between $|1\rangle$ and $|2\rangle$ similar to the effect of an optical field Ω_N. Besides the coherent hyperfine coupling between $|1\rangle$ and $|2\rangle$

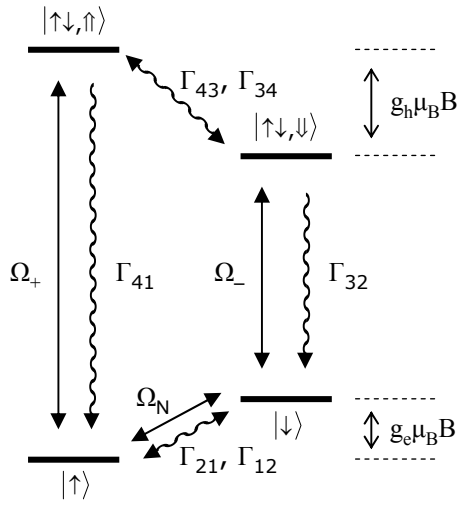

Figure 7.1: *Level scheme of the X^--system. It can be modeled by an 4-level system with spontaneous relaxation rates $\Gamma_{41} = \Gamma_{32}$. The laser couples $|\uparrow\rangle$ and $|\uparrow\downarrow, \Uparrow\rangle$ with Rabi freqency Ω_+ and $|\downarrow\rangle$ and $|\uparrow\downarrow, \Downarrow\rangle$ with Rabi freqency Ω_-. Ω_N represents the hyperfine-induced mixing of $\uparrow$ and $\downarrow$ and $\Gamma_{21/12}$/ $\Gamma_{43/34}$ are incoherent relaxation rates. The energy splitting between the electron and exciton states is given by the Zeeman energies.*

there are incoherent mechanisms with rates Γ_{21} and Γ_{12} between the two electron states. Accordingly rates Γ_{43} and Γ_{34} connect the exciton levels $|3\rangle$ and $|4\rangle$. Both Γ_{12} and Γ_{34} are the reverse transition rates of Γ_{21} and Γ_{43} so that their relative values are determined by the Boltzmann factor [98]:

$$\Gamma_{12} = \Gamma_{21} exp\left(\frac{g_e \mu_B B}{k_B T}\right), \Gamma_{34} = \Gamma_{43} exp\left(\frac{g_h \mu_B B}{k_B T}\right) \tag{7.2}$$

with the Boltzmann constant k_B and temperature T. The X^--system from Fig. 7.1 is modeled with the semi-classical optical Bloch equations taking into account the four quantum dot states introduced above and a coherent optical field with energy $\hbar\omega_0$. The derivation of the Bloch equations follows mainly [98, 80] and is demonstrated for a two-level system in chapter 4.2. The Schrödinger equation in rotating wave approximation and in the rotating frame has the form:

$$\hat{H}\tilde{\mathbf{c}} = i\hbar\frac{d}{dt}\tilde{\mathbf{c}} \tag{7.3}$$

with the Hamiltonian

$$\hat{H} = \hbar \begin{pmatrix} 0 & \frac{1}{2}\Omega_N & 0 & \frac{1}{2}\Omega_+ \\ \frac{1}{2}\Omega_N & \delta_2 & \frac{1}{2}\Omega_- & 0 \\ 0 & \frac{1}{2}\Omega_- & \delta_3 & 0 \\ \frac{1}{2}\Omega_+ & 0 & 0 & \delta_4 \end{pmatrix} \tag{7.4}$$

The detunings δ_i are

$$\begin{aligned} \hbar\delta_2 &= \hbar\omega_{12} \\ \hbar\delta_3 &= \hbar\omega_{13} - \hbar\omega_0 \\ \hbar\delta_4 &= \hbar\omega_{14} - \hbar\omega_0 \end{aligned} \tag{7.5}$$

$\hbar\omega_{1i}$ is the energy difference between the states $|1\rangle$ and $|i\rangle$. This implies that $\hbar\omega_{12} = E_Z^e$ and $\hbar\omega_{14} - \hbar\omega_{13} = E_Z^h$. By using the density operator $\tilde{\rho}$ the incoherent relaxation rates Γ can be written in the Lindblad form [99] connecting the relevant levels:

$$\begin{aligned} L\hat{\tilde{\rho}} = &\sum_{i,j} \frac{1}{2}\Gamma_{ij} \left[2|j\rangle\langle i|\tilde{\rho}|i\rangle\langle j| - (|i\rangle\langle i|\tilde{\rho} + \tilde{\rho}|i\rangle\langle i|)\right] \\ =&\frac{1}{2}\Gamma_0 \left(2|1\rangle\langle 4|\tilde{\rho}|4\rangle\langle 1| - |4\rangle\langle 4|\tilde{\rho} + \tilde{\rho}|4\rangle\langle 4|\right) \\ +&\frac{1}{2}\Gamma_0 \left(2|2\rangle\langle 3|\tilde{\rho}|3\rangle\langle 2| - |3\rangle\langle 3|\tilde{\rho} + \tilde{\rho}|3\rangle\langle 3|\right) \\ +&\frac{1}{2}\Gamma_{21} \left(2|1\rangle\langle 2|\tilde{\rho}|2\rangle\langle 1| - |2\rangle\langle 2|\tilde{\rho} + \tilde{\rho}|2\rangle\langle 2|\right) \\ +&\frac{1}{2}\Gamma_{12} \left(2|2\rangle\langle 1|\tilde{\rho}|1\rangle\langle 2| - |1\rangle\langle 1|\tilde{\rho} + \tilde{\rho}|1\rangle\langle 1|\right) \\ +&\frac{1}{2}\Gamma_{43} \left(2|3\rangle\langle 4|\tilde{\rho}|4\rangle\langle 3| - |4\rangle\langle 4|\tilde{\rho} + \tilde{\rho}|4\rangle\langle 4|\right) \\ +&\frac{1}{2}\Gamma_{34} \left(2|4\rangle\langle 3|\tilde{\rho}|3\rangle\langle 4| - |3\rangle\langle 3|\tilde{\rho} + \tilde{\rho}|3\rangle\langle 3|\right) \end{aligned} \tag{7.6}$$

The optical Bloch equations are extracted from the master equation of the total system:

$$i\frac{d\tilde{\rho}_{ij}}{dt} = \frac{1}{\hbar}\sum_{k=1}^{4} \left(H_{ik}\tilde{\rho}_{kj} - \tilde{\rho}_{ik}H_{kj}\right) + i(L\tilde{\rho})_{ij} \tag{7.7}$$

Equation 7.7 defines a set of equations which can be solved including the condition $\rho_{11} + \rho_{22} + \rho_{33} + \rho_{44} = 1$. A steady state solution with $\frac{d\tilde{\rho}}{dt} = 0$ is sufficient to fully describe the X^- as the equilibration time scales of the quantum dot system are much shorter than the measurement time scales. In this context the $\tilde{\rho}_{ii}$ represent the occupation of the corresponding quantum dot state $|i\rangle$ and the off-diagonal elements $\tilde{\rho}_{ij}$ represent the coherence terms.

Differential transmission

All experiments shown here are carried out with differential transmission spectroscopy. To be able to compare theory and experiment it is required to link the measured absorption $\Delta T/T$ with the calculated density matrix elements ρ_{ij}. The derivation follows again the approach in chapter 4.2 leading to [98]:

$$\alpha = \frac{\Delta T}{T} \approx \alpha_0 \Gamma_0 \frac{\Omega_+ \mathrm{Im}[\tilde{\rho}_{14}] + \Omega_- \mathrm{Im}[\tilde{\rho}_{23}]}{\Omega_+^2 + \Omega_-^2} \tag{7.8}$$

If a linearly polarized laser is used both the blue (higher energy) and the red (lower energy) transition contribute to the absorption signal. This fact is reflected by $\tilde{\rho}_{14}$ and $\tilde{\rho}_{23}$ in equation 7.8.

7.1.1 Spin-pumping and cotunneling-limited regime

As it is already mentioned in chapter 7 there are two different regimes in which the X^- can be measured: the spin-pumping and cotunneling-limited regime. Whether the charged exciton is in the spin-pumping regime or not depends primarily on the ratio Γ_{43} to Γ_{21}. If $\Gamma_{43} > \Gamma_{21}$ spin shelving occurs since the accumulation of population in $|2\rangle$ is faster than the relaxation from $|2\rangle$ to $|1\rangle$. This means that the system is prepared in the $|2\rangle = |\downarrow\rangle$-state. On the other hand if $\Gamma_{43} \leq \Gamma_{21}$ the charged exciton is in the cotunneling-limited regime. In that case both state $|1\rangle$ and $|2\rangle$ are partially populated.
Γ_{21} and Γ_{43} are total transition rates between the corresponding levels. They all consist of several rates based on different physical mechanisms coupling the states to each other. There are four contributions to the overall rates:

$$\Gamma_{21} = \kappa_{ct} + \kappa_{hf} + \kappa_{SO} \tag{7.9}$$

$$\Gamma_{43} = \kappa_{hh-lh} + \kappa_{hf} + \kappa_{SO} \tag{7.10}$$

κ_{ct} refers to the cotunneling rate, κ_{hf} results from hyperfine-induced spin-flip-flop processes and κ_{SO} is the contribution of phonon-assisted spin-orbit interaction [28, 100]. κ_{hh-lh} only couples the exciton states due to mixing of heavy-hole and light-hole states.
Cotunneling is inherent in quantum dots separated by a thin barrier from an electron reservoir. It can induce a spin-flip between the electron states mediated by tunneling in and out of a Fermi sea. In Fig. 7.2(b) the three subsequent steps necessary for a cotunneling event are depicted. There are two paths how the spin state can flip due to cotunneling: (1) The electron tunnels out of the quantum dot into the reservoir which creates a virtually empty state and thereafter an electron with opposite spin tunnels into the lower state. (2) One electron from the Fermi sea tunnels in the quantum dot and forms a virtual spin singlet with the resident

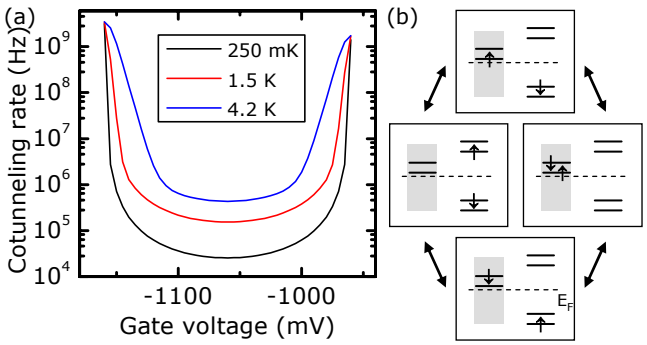

Figure 7.2: *(a) Simulation of the cotunneling rates at different temperatures over the whole plateau of a charged exciton. A tunneling rate of* $\Gamma_t = 14 * 10^9\,\mathrm{s}^{-1}$ *is used. (b) Cotunneling is mediated via an intermediate state. There are two possible processes causing the cotunneling.*

electron and afterwards the originally resident electron is absorbed in the electron bath. This process is bidirectional and can also take place from the lower- to the higher-energetic state. If $|\uparrow\rangle$ and $|\downarrow\rangle$ are degenerate there is also cotunneling present. According to [101] the cotunneling rate κ_{ct} can be numerically calculated with:

$$\kappa_{ct} = \frac{\hbar\Gamma_{tun}^2}{2\pi}\int_{\epsilon}\left|\frac{1}{\frac{e(V_g-V_A)}{\lambda}+\epsilon+\frac{i}{2}\hbar\Gamma_{tun}}+\frac{1}{\frac{e(V_B-V_g)}{\lambda}-\epsilon+\frac{i}{2}\hbar\Gamma_{tun}}\right|^2 f_F(\epsilon)[1-f_F(\epsilon)]d\epsilon \tag{7.11}$$

Γ_{tun} is the tunneling rate through the barrier, V_A and V_B are the voltages at which the exciton plateau starts and ends and V_g is the gate voltage. The Fermi-Dirac distribution $f_F(E) = (exp(E/k_BT)+1)^{-1}$ determines the occupation in the Fermi sea. The cotunneling depends critically on the tunnel coupling between quantum dot and Fermi sea. So the thickness of the tunnel barrier defines the tunneling rate. The hyperfine part of the relaxation rates Γ originates from the flip-flop term in equation 7.1. A relaxation from $|2\rangle$ to $|1\rangle$ or vice versa occurs via a simultaneous spin-flip of electron and nucleus [102]. In this process the total angular momentum is conserved but the energy splittings of electron spins and nuclear spins are very different in finite magnetic fields so that energy conservation cannot be taken for granted. Therefore the hyperfine relaxation rate κ_{hf} has a strong dependence on the external magnetic field. The model for the magnetic field behavior of the dynamic spin-flip part of the hyperfine interaction is based on the assumption that an overlap between the electron wave functions of $\uparrow$- and $\downarrow$-state in the energy domain is necessary for an electron spin flip [29]. The strength of the hyperfine interaction can be estimated as $\bar{A}/N$ with the averaged hyperfine constant $\bar{A}$ and the number of the contributing nuclear spins N. The hole-spin nuclear-spin interaction can be neglected as the hole hyperfine constant is one order of magnitude smaller than $\bar{A}$ [103, 104].

Transitions between $|\downarrow\rangle$ and $|\uparrow\rangle$ can also occur due to phonon-assisted spin-orbit interaction in the quantum dot [105]. The spin-orbit effect links the momentum of the electron with its spin state which leads to a slight admixture of the $\uparrow$- and $\downarrow$-states. In principle such a coupling of two levels can be taken as a transition rate. However the energy mismatch between the Zeeman-levels prevents a direct relaxation via spin-orbit effects. Acoustic phonons can provide the energies necessary for this process so that the rate κ_{SO} needs to be considered in the overall transition rate Γ_{21}. The phonon-assisted spin-orbit relaxation depends to the fifth power on the magnetic field which implies that it becomes dominant at high magnetic fields (typically above 5 T) [106].
The spin of the exciton states is dictated by the hole spins as the two electron spins cancel out. In InGaAs quantum dots a weak valence-band mixing is present so that light-hole states weakly contribute to the exciton states. The optical selection rules are relaxed and transitions from $|4\rangle$ to $|2\rangle$ or from $|3\rangle$ to $|1\rangle$ are not forbidden anymore. The admixture is in the low percent range and is included in the calculation as an additional rate κ_{hh-lh} [107, 28].

Spin-pumping in the charged exciton

The X^- in InGaAs quantum dots offers an intrinsic method to prepare the system in a defined electron spin state [23]. As long as no magnetic field is applied to the sample $|1\rangle$ and $|2\rangle$ are degenerate. Excitation of the quantum dot with a resonant laser creates an exciton which can decay into the $|\uparrow\rangle$- or in the $|\downarrow\rangle$-state (inset Fig. 7.3(a)). The plateau of the charged exciton shows the well-known Stark shift. In Fig. 7.3(a) one half of a plateau is depicted in a grey-scale plot at $B = 0\,\mathrm{T}$. The color-scale corresponds to the absorption contrast and the variation in the strength of contrast over the plateau stems from the power variation with laser detuning. Basically absorption is observed over the whole gate voltage range measured. If the magnetic field is switched on the situation changes dramatically. Due to the Zeeman splitting two lines corresponding to the two exciton states $|\uparrow\downarrow, \Uparrow\rangle$ and $|\uparrow\downarrow, \Downarrow\rangle$ are observable under excitation with linearly polarized light. At 300 mT the absorption at the center of the plateau is quenched as the population is pumped in the $|\downarrow\rangle$-state while the absorption accesses the depopulated $|\uparrow\rangle$-state. Due to the heavy-hole-light-hole mixing in the valence band the originally forbidden transition from $|4\rangle$ to $|2\rangle$ is transformed into a weak transition. This means that a certain percentage of the population of the exciton level relaxes in level $|2\rangle$ where it is trapped. So within one cycle the whole population is transferred in $|2\rangle$ and as $|1\rangle$ is unoccupied no photons can be scattered anymore. The appearance of the spin-pumping effect depends on the ratio of rates Γ_{42} and Γ_{21} with $\Gamma_{21} < \Gamma_{42}$. In Fig. 7.3(b) absorption is observed in the range of $-670\,\mathrm{mV}$ to $-590\,\mathrm{mV}$ which is the edge of the X^- where tunneling of the resident electron sets in. Above $-590\,\mathrm{mV}$ spin-pumping dominates and absorption is quenched. At the edge of the plateau the cotunneling rate is

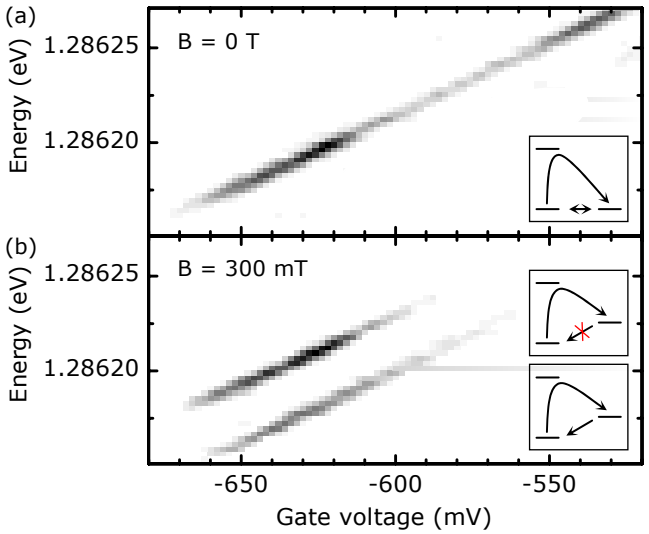

Figure 7.3: *Spin pumping on a negatively charged exciton. (a) At zero magnetic field the ground state and the exciton state are degenerate. One resonance is detected in DT and forms the plateau. Here only the left half of the plateau is shown with a finite transmission signal over the whole gate voltage range. (b) A magnetic field of* 300 mT *lifts the degeneracy. On the plateau ($V_g > -580\,\mathrm{mV}$) the spin population accumulates in the $\downarrow$-state (upper inset). At the edge cotunneling is strong and prevents spin-pumping (lower inset).*

increased and therefore spin-flips take place which recovers the absorption signal. The cotunneling rate κ_{ct} is increased at the edges of the plateau as shown in Fig. 7.2(a) and therefore is $\Gamma_{21} > \Gamma_{42}$ so that spin-pumping is not possible any more.

Spin population and contrast at 4.2 K

Now the occupation and normalized contrast at 4.2 K are calculated using the Bloch equations introduced in chapter 7.1. For the solution of the system of linear equations and its evaluation only Γ_0, $\Omega_\pm$, Ω_N, $\Gamma_{43/34}$ and $\Gamma_{21/12}$ are considered. The set of typical parameters for self-assembled InGaAs quantum dots are: $\Gamma_0 = 1\,\mu\mathrm{eV}$, $\Omega_\pm = 0.5\,\mu\mathrm{eV}$, $\Omega_N = 0.7\,\mu\mathrm{eV}$ and $\Gamma_{43} = 4 * 10^{-6}\,\mu\mathrm{eV}$ [98]. The detunings are for resonant excitation of the blue ($\omega_{14} - \omega_0 = 0$) transition $\delta_2 = E_Z^e/\hbar = 40\,\mu\mathrm{eV/T} * \mathrm{B}$, $\delta_3 = -E_Z^h/\hbar = -47\,\mu\mathrm{eV/T} * \mathrm{B}$ and $\delta_4 = 0$ with magnetic field B. $\Omega_+ = \Omega_- = 1/2\Gamma_0$ holds as the quantum dot in the experiment (chapter 7.2) is in saturation and the laser is linearly polarized which means that Ω_+ and Ω_- are identical. With magnetic field the electron and exciton states split up and the overall rates between $|1\rangle$ and $|2\rangle$ ($|3\rangle$ and $|4\rangle$) change. The modification of the transition rates Γ_{ij} due to a magnetic field is taken into account in form of the Boltzmann factor $exp(E_Z^{e/h}/k_BT)$ and in the

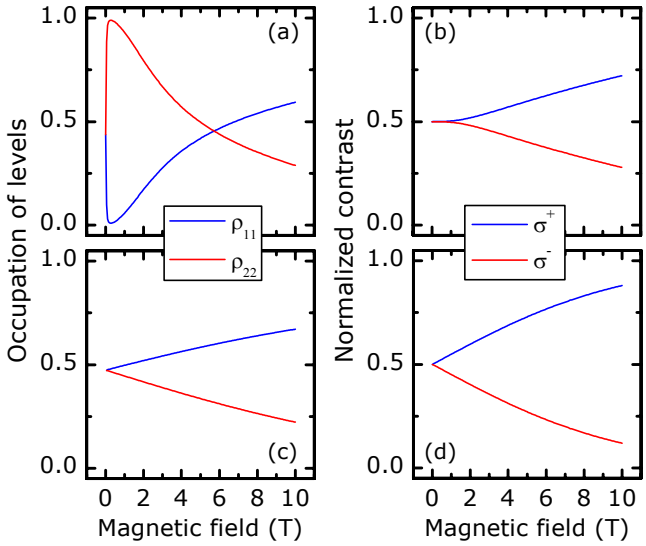

Figure 7.4: *Simulation of the populations of* $|1\rangle$ *(*ρ_{11}*) and* $|2\rangle$ *(*ρ_{22}*)and normalized contrast for excitation with light polarization* σ^+ *and* σ^- *at* 4.2 K *by means of a four-level system. (a) and (b) are calculated for the spin-pumping regime with* $\kappa = 10^{-12}$*. (c) and (d) show the cotunneling-limited regime using* $\kappa = 10^{-6}$*.*

detunings δ the Zeeman energies are also included. The density matrix elements ρ_{ii} correspond to the population of state $|i\rangle$. The absorption of photons by the quantum dot is dictated by the population of the ground states $|1\rangle$ and $|2\rangle$. If for example the state $|1\rangle$ is not populated no absorption can be observed. The occupation of levels is depicted for the spin-pumping (Fig. 7.4(a)) and the cotunneling-limited regime (Fig. 7.4(c)). The cotunneling rate for the spin-pumping case is chosen to be $\kappa_{ct} = 10^{-6}\,\mu$eV and for the cotunneling-limited case $\kappa_{ct} = 1\,\mu$eV. For this case κ_{hf} and κ_{SO} are neglected so that $\Gamma_{21} = \kappa_{ct}$. The model considers all four states of the X^- causing a very low occupation of the exciton states, increasing slightly with magnetic field. Both figures display resonant excitation of $|1\rangle$ to $|4\rangle$ (blue transition) and non-resonant excitation (detuned by $E_Z^e + E_Z^h$) of $|2\rangle$ to $|3\rangle$ with the one laser. In the spin-pumping regime the populations ρ_{11} and ρ_{22} have one crossing point. At zero magnetic field the populations are equal. The electron states are degenerate and therefore both have an occupation of 0.5. At low magnetic fields the occupation of $|2\rangle$ is higher than $|1\rangle$ which means the spin is prepared in $|2\rangle$. Not only Γ_{43} needs to be larger than Γ_{21} but also the coherent hyperfine coupling Ω_N participates in this process. With increasing magnetic field the electron Zeeman energy becomes larger than Γ_0 and therefore the occupation of ρ_{22} diminishes, as is pointed out in [28]. For the parameters used in the simulation the second crossing occurs at about 6 T. So for magnetic fields larger than the crossing no spin-pumping takes place any more. If $\kappa_{ct} = 1\,\mu$eV, the curves in Fig. 7.4(c) are obtained. The relaxation rate

Γ_{21} dominates over Γ_{43} so that the response of the system is entirely determined by Γ_{21}. Population which is transferred to $|3\rangle$ and decays into $|2\rangle$ relaxes by cotunneling with a rate of about $10^8\,\mathrm{s}^{-1}$ back into $|1\rangle$. The occupation starts at 50% for both electron levels and ρ_{11} increases almost linearly with magnetic field while ρ_{22} decreases accordingly. The overall rate from $|2\rangle$ to $|1\rangle$ increases as it is governed by the Boltzmann factor which means that $\Gamma_{12}/\Gamma_{21} \propto exp(E_Z^e/k_BT)$.
The normalized absorption α_n is directly calculated from the off-diagonal density matrix elements ρ_{14} and ρ_{23}. The normalized absorption for σ^+- and σ^--light are:

$$\alpha_n(\sigma^+) = \frac{\alpha(\text{blue})}{\alpha(\text{blue}) + \alpha(\text{red})}$$
$$\alpha_n(\sigma^-) = \frac{\alpha(\text{red})}{\alpha(\text{blue}) + \alpha(\text{red})} \tag{7.12}$$

while α(blue) and α(red) refer to equation 7.8 for the blue and red resonance conditions. In the simulation it was tested how the linear polarization affects the results for the normalized contrast compared to circular excitation of only one transition with $\Omega_\pm = \Gamma_0$ and the corresponding other frequency $\Omega_\mp \approx 0$. Over the range from 0 to 10 T the difference between the contrasts can add up to a deviation of 5%. The reason for this low contribution of the second transition is that it is far detuned from resonance.
The overall absorption in the case of optical spin-pumping is lowered. As the absorption is normalized the regions of spin-pumping appear as if contrast does not change though the magnetic field is tuned. This behavior is shown in Fig. 7.4(b). The spin-pumping decreases with magnetic field as the energy difference between $|1\rangle$ and $|2\rangle$ increases. Therefore the spin-flip does not conserve energy any more and the absorption approaches to the behavior of a system without spin-pumping effect. At large magnetic fields the values of the contrast are dominated by the Boltzmann factors again. In the cotunneling-limited regime (Fig. 7.4(d)) the normalized contrast under resonant excitation is determined by the relative occupation of $|1\rangle$ and $|2\rangle$ and therefore directly correlated to the Boltzmann factor. Due to the small ratio of Zeeman energy and thermal energy the contrast has an almost linear characteristics. The splitting reaches about 90% at 10 T for the blue transition.

7.1.2 Temperature calibration with a quantum dot

An important parameter in the optical Bloch equations is the temperature of the system. The sample used in this work was mounted in a ^{3}He-cryostat (compare chapter 3.1.2) in which the temperature can be tuned from 250 mK to about 10 K. The base temperature (minimum temperature) is obtained at the ^{3}He-pot. The sample is fixed with a thermally conducting glue on a gold-coated chip carrier which is thermally coupled to the ^{3}He-pot via a copper tube. Nevertheless the temperature of the ^{3}He-pot and the bath temperature of the electrons are not identical if the

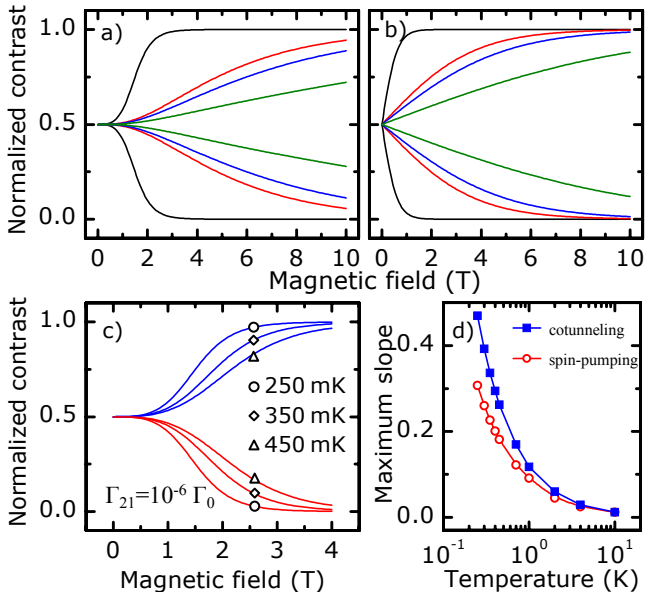

Figure 7.5: *Normalized contrast at different temperatures for the spin-pumping regime (a) and the cotunneling-limited regime (b). The curves for the temperatures are color-coded: green = 4.2 K, blue = 2 K, red = 1.5 K and black = 250 mK. For the spin-pumping case (c) shows the magnetic field behavior at 250 mK, 350 mK and 450 mK. (d) The slope of the calculated curves can be used as a measure for the temperature. Exemplary slopes for spin-pumping and cotunneling regime.*

sample is cooled down to 250 mK. The electron bath temperature is of interest especially for many-body phenomena like the Kondo effect [35] or Fermi-edge singularity [33]. The calculation of the normalized contrast using the optical Bloch equations offers the opportunity to deduce the electron bath temperature of the sample. The prerequisite for this method is that the Rabi frequencies $\Omega_{\pm/N}$, the spontaneous rate Γ_0 and the different transition rates Γ_{ij} are known. The g-factors for electron and hole are also necessary. The normalized contrast calculated for the charged exciton system is depicted for different temperatures in Fig. 7.5(a) and (b). 7.5(a) shows the quantum dot in the spin-pumping regime and (b) is in the cotunneling-limited regime. All parameters are identical for (a) and (b) except Γ_{21}. It is $10^{-6}\,\mu$eV for spin-pumping and $1\,\mu$eV for the cotunneling-limited regime. The absorption contrasts are calculated for bath temperatures 250 mK, 1.5 K, 2 K and the temperature of liquid helium 4.2 K. In Fig. 7.5(a) the spin-pumping signature (contrast on both blue and red transition are 0.5) is present at low magnetic fields. The critical magnetic field at which the contrasts start to split up depend on the temperature. This implies that there is a competition between the spin-pumping effect and the contrast splitting due to the with magnetic field increasing Boltzmann factor. Spin-pumping can only take place as long as the thermal energy is larger than the Zeeman energy,

which increases with magnetic field. So eventually spin-pumping is suppressed in an increasing magnetic field as the thermal energy constant with magnetic field. In the cotunneling-limited regime in Fig. 7.5(b) only the influence of the Boltzmann factor can be observed. At 4.2 K k_BT exceeds the Zeeman energy up to 9.2 T and therefore the curves are almost linear in the range 0 - 10 T. A comparison of the two regimes shows that the contrast for the spin-pumping evolves into the contrast for the cotunneling-limited case. Basically both cases lead to identical normalized contrasts with the difference that in the spin-pumping regime there is an additional effect only contributing at low magnetic fields. The range of magnetic field in which this happens is defined by the ratio of Zeeman energy and thermal energy. This can be understood, as the spin pumping can only take place at low magnetic fields. It is strongly suppressed with increasing magnetic field as the energy mismatch between $|1\rangle$ and $|2\rangle$ grows. Then the rate $\Gamma_{21} \gg \Gamma_{12}$ and $\Gamma_{21} - \Gamma_{12} \approx \Gamma_{21} > \Omega_N$ so that the condition for the cotunneling-limited regime is reached.
In both cases the temperature appears in the Boltzmann factor which determines the slope of the contrast. The bath temperature can be deduced by fitting the normalized contrast α_n to the measured data. In 7.5(c) three curves are shown for temperatures in the range of 250 mK to 450 mK which point out the change of slope with temperature. The sensitivity S can be defined as the maximum of the derivative of the normalized contrast:

$$S = max\left[\frac{d\alpha_n}{dB}\right] \tag{7.13}$$

In Fig. 7.5(d) the sensitivity is illustrated for the two examples discussed in Figs. 7.5(a) and (b). Both functions are nonlinear with temperature and the sensitivity is higher for the cotunneling-limited regime. Therefore the accuracy of the temperature analysis is in general better for this case.

7.2 Electron population in magnetic fields

In the present chapter the predictions of chapter 7.1.2 are experimentally tested on an InGaAs quantum dot and the electron bath temperature is measured. The experimental data discussed in this chapter were obtained with differential transmission spectroscopy on a sample in which the quantum dot layer is 25 nm apart from the back contact and 10 nm apart from the superlattice, respectively. This implies that there is no hole accumulation at the interface to the superlattice. The X^- resonance was roughly at 951.4 nm. The quantum confined Stark effect for the X^- is with 0.42 μeV/mV rather low for that type of quantum dots and typical linewidths are 5 μeV. All measurements were performed in the middle of the X^--plateau at $V_g = -1050$ mV where cotunneling should have the least contribution. As excitation laser power 10 nW were chosen which is the saturation power for the quantum

dot. If a magnetic field is applied to the quantum dot in Faraday geometry the electron and exciton states split up into two resonances. The parabolic behavior in energy of the two resonances as a funciton of magnetic field is described as the linear Zeeman shift and the quadratic diamagnetic shift. For this model quantum dot an exciton g-factor $g_X = 1.5$ according to $E_Z^X = g_X \mu_B B = 87\,\mu\text{eV/T}$ is extracted from the experiment. Likewise the diamagnetic shift was found to be $8.5\,\mu\text{eV/T}^2$. The electron and hole g-factor follow the formula $g_X = g_e + g_h$ and the electron g-factor was determined by means of two-color spectroscopy [29]. The electron g-factor is derived to be 0.69 and the hole g-factor amounts to 0.81.
For a comparison of the experiment with the theoretical predictions derived from the optical Bloch equations it is necessary to measure the contrast at different magnetic fields. Ideally the measured contrasts at $B = 0\,\text{T}$ are 50% of the overall contrast under excitation with linear polarization. The blue and red Zeeman branches can be spectrally resolved at an external magnetic field of about 0.2 - 0.3 T. For the quantum dot both the Zeeman shift and the diamagnetic shift of the resonance energy are considered. The magnetic field was tuned to different values and the differential transmission signal of the quantum dot for both the blue and red branch were obtained by applying linearly polarized light. The linear polarization of the laser light was set by measuring one fine structure component of the neutral exciton. The polarization adjustment is only accurate within 3% [98].
The blue and red resonances were measured at different magnetic fields and a Lorentzian function was fitted to the peaks. The experimental contrast is given by the fit values of the area underneath the Lorentzian curve A and the linewidth of the peak Γ_{exp}: $\alpha_{exp} = A/\Gamma_{exp}$. For the comparison with the theory, the measured data are normalized relative to the overall contrast of the blue and red transition. This approach allows a direct observation whether spin-pumping is present in the system and how strong the spin (Pauli) blockade is. The data in Fig. 7.6 and 7.7 were derived according to equation 7.12 with α(blue) and α(red) being experimentally obtained contrasts.

7.2.1 Spin splitting and temperature dependence

The normalized contrast of the transitions of the negatively charged exciton are given in Fig. 7.6 for magnetic fields between 0 and 6 T at temperatures 4 K, 2 K, 1.5 K and 250 mK. In all four diagrams the experimental data are depicted as blue squares (resonant with blue transition) and red circles (resonant with red transition). The corresponding simulations appear as color-coded lines. For Fig. 7.6(a), (b) and (c) the nominal base temperatures of the ^{3}He-pot are used in the calculations. In Fig. 7.6(d) the best-fit value for the electron bath temperature of 380 mK is employed. From equation 7.11 it is known that the cotunneling rate also depends on the temperature. This is taken into account for the simulations by using $\kappa_{ct}(4\,\text{K}) = 0.08\,\mu\text{eV}$, $\kappa_{ct}(2\,\text{K}) = 0.004\,\mu\text{eV}$, $\kappa_{ct}(1.5\,\text{K}) = 0.003\,\mu\text{eV}$ and $\kappa_{ct}(250\,\text{mK}) = 0.0005\,\mu\text{eV}$. These

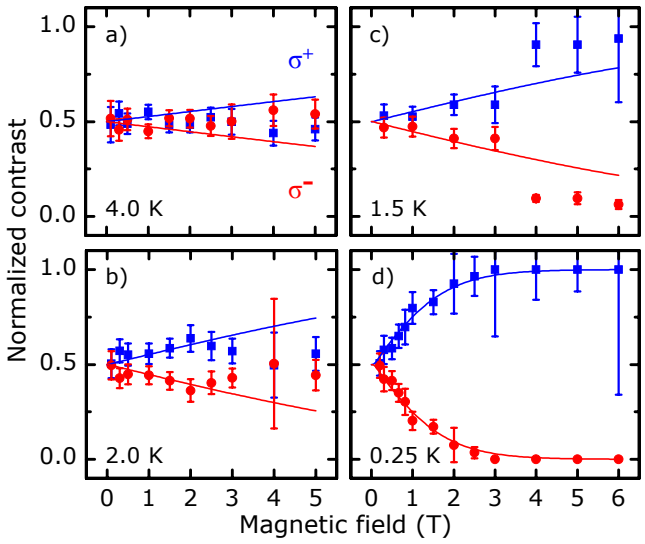

Figure 7.6: *Normalized contrasts extracted from measurements in the ^{3}He-system (data points with error bars). The lines are calculated using the optical Bloch equations taking into account a 4-level system. Blue data points and lines represent resonant excitations with σ^+-light and red refers to σ^--excitation. For all graphs (a)-(d) the input parameters for the simulation are identical except the temperature. The base temperatures are (a)* 4 K*, (b)* 2 K*, (c)* 1.5 K *and (d)* 250 mK*.*

values are calculated using equation 7.11 and $\Gamma_t = 0.02\,\text{meV}$ from chapter 6.2.1.
In Fig. 7.6(a) the normalized contrast at a temperature of 4 K for magnetic fields up to 5 T is shown. All data points are spread around 0.5 and the fit errors of the data amount to a maximum of 0.09. 0.5 is within the error bars of all data points. Above 1 T the contrast of the red branch is higher than the blue branch. So there is no indication of a difference. The rates between $|1\rangle$ and $|2\rangle$ and vice versa are approximately the same, as the ratio between Zeeman energy and thermal energy is very low. This implies that $\Gamma_{21} \approx \Gamma_{12}$ as the ratio of them is governed by $\exp(E_Z/k_BT)$. From the experiment one cannot conclude that there is a contrast splitting between the blue and the red branch at 4 K.
At $T = 2\,\text{K}$ (Fig. 7.6(b)) one observes already a small tendency for a contrast splitting. At low magnetic fields experimental and theoretical values show reasonable agreement with each other. Above 3 T the theory curves are not within the error bars of the measured data, which is similar to the 4 K-case. The magnetic field dependence of the calculated curve is still linear.
In Fig. 7.6(c) which is measured at 1.5 K a clear spin selectivity of the absorption contrast is present. Especially at higher magnetic fields the difference between the blue and red transition strength is significant despite the increased errors. The contrasts calculated from the Bloch equations become now slightly nonlinear and follow

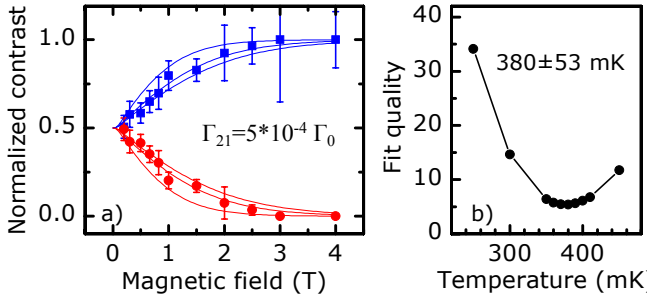

Figure 7.7: *(a) Normalized contrast at base temperature* 250 mK. *The lines show the calculated absorption contrasts at* 250 mK, 350 mK *and* 450 mK *(from left to right). (b) In (a) the temperature is the fit parameter in the evaluation of the Bloch equations. The minimum of the fit quality* χ^2 *as a function of the temperature determines the real temperature of the electron bath. A bath temperature of* 380 ± 53 mK *is found in the investigated sample.*

the expected exponential behavior of the Boltzmann factor. At low magnetic fields the splitting grows slowly accordingly to the calculation. From 3 T to 4 T an abrupt change of the normalized contrasts occur. From 4 T to 6 T a very weak increase of the splitting can be seen. From 1 T to 3 T the calculated normalized contrast shows a good agreement with the experimental data. The jump in contrast splitting cannot be explained by the model. The error bars of the blue transition become very large which is caused by the line shape of the resonances. They do not have a Lorentzian lineshape any more. They rather look like two merged Lorentzian peaks. As the contrast is normalized this inaccuracy in the fit also affects the red branch. The unusual lineshape might be caused by a second quantum dot resonance from a different quantum dot or might be a signature of dynamic nuclear spin polarization [20].

The diagram in Fig. 7.6(d) is measured at a base temperature of the ^{3}He-pot of 250 mK. A clear difference between the populations in $|1\rangle$ and $|2\rangle$ can be seen. The experimental curves follow the Boltzmann statistics which is governed by $exp(E_Z/k_BT)$. Up to 3 T the population of $|1\rangle$ increases and the population of $|2\rangle$ decreases with magnetic field. At 3 T a comprehensive spin blockade is achieved within the maximum errors ± 0.09. On the red transition no absorption can be detected and therefore the signal can only be as large as the noise background or below. This means that $|2\rangle$ is not occupied and almost all the population is in $|1\rangle$. The simulation curve depicted in 7.6(d) is calculated assuming a bath temperature of 380 mK which is obtained as a best fit value for the experimental data.

7.2.2 Temperature of the electron spin bath

The base temperature T_{base} of the ^{3}He-system which is reached according to the thermometer at the ^{3}He-pot is 250 mK. Nevertheless the electron bath temperature T_{bath} of the sample is higher since the wires and the gold-coating by which the sample is coupled to the ^{3}He-pot have a thermal resistance.
In order to determine the temperature of the electron bath the parameters specified in chapters 7.1.1 and 7.2.1 are used for the simulation. All parameters are fixed except the temperature T. In Fig. 7.7(a) the experimentally obtained normalized contrast is depicted as blue and red data points. The three lines for each branch correspond to three temperatures which are from left to right: 250 mK, 350 mK and 450 mK. 250 mK is the base temperature of the setup and defines the lowest possible temperature. The second curve gives the best fit.
The least-square-method was used to find the best fit for T to the data. χ^2 is used as a measure for the fit quality and is calculated according to [108]:

$$\chi^2 = \sum_{B_i} \left(\frac{\alpha_{exp,n}(B_i) - \alpha_n(B_i)}{\delta\alpha_{exp,n}(B_i)} \right)^2 \tag{7.14}$$

with the experimentally obtained normalized contrast $\alpha_{exp,n}(B_i)$ and its error $\delta\alpha_{exp,n}(B_i)$. B_i are the magnetic fields at which differential transmission spectra are recorded. The error $\delta\chi^2$ follows from:

$$\delta\chi^2 = \sqrt{\sum_{B_i} \left(2\, \frac{\alpha_{exp,n}(B_i) - \alpha_n(B_i)}{(\delta\alpha_{exp,n}(B_i))^2}\, \delta\alpha_{exp,n}(B_i) \right)^2} \tag{7.15}$$

Fig. 7.7(b) shows the χ^2 for different temperatures. The electron bath temperature is deduced to be 380 ± 53 mK.

7.3 Conclusion

In this chapter it is demonstrated that the negatively charged exciton X^- of a self-assembled InGaAs quantum dot can be modeled by solving the optical Bloch equations for a 4-level system. The density matrix elements $\tilde{\rho}_{ij}$ are linked to the absorption contrast α which is the experimentally obtained contrast. By means of analytical calculations the spin-pumping and the cotunneling-limited regime are simulated at temperatures between 4.2 K and 250 mK. In both cases the slope of the normalized contrast α_n is dominated by the Boltzmann factor determining the relative transition rates between the states $|1\rangle$ and $|2\rangle$ or $|3\rangle$ and $|4\rangle$, respectively. The calculation also shows that the occupation of the electron ground states $|1\rangle$ and $|2\rangle$ basically defines the optical response of the system in magnetic fields and that

there is hardly any occupation in $|3\rangle$ and $|4\rangle$ involved.
For the quantum dot investigated here one can deduce that in the limit of $\kappa_{ct} > \kappa_{hf}, \kappa_{SO}$ a good fit quality at the lowest base temperature can be achieved. The cotunneling rate is temperature sensitive as it is known from the theory and therefore κ_{ct} can be modified with the temperature. In principle it should be possible to bring the quantum dot into the spin-pumping regime if one has control over the temperature in the experiment and κ_{ct} is close to the spin-pumping regime.
The electron bath temperature of the quantum dot at a base temperature of 250 mK is determined to be 380 ± 53 mK. For the derivation of the electron bath temperature it is necessary to measure a power series of the quantum dot from which one can determine (by fitting) the Rabi frequencies Ω_+ and Ω_- and the spontaneous recombination rate Γ_0. The exciton, electron and hole g-factors are obtained with two-color spectroscopy. By means of solving the Bloch equations and by fitting the experimental data the temperature can be extracted.

Chapter 8

Summary and perspectives

Self-assembled quantum dots are nanostructures embedded in a solid-state matrix. They consist typically of 10^4 atoms and form a trapping potential for charges. Due to the strong confinement they feature a quantized energy spectrum which is similar to that of atoms. This work focuses on the interaction of localized quantum dot states with nearby electron and spin reservoirs such as impurities and a Fermi sea of electrons.

In the framework of this thesis a new setup for resonant laser spectroscopy on self-assembled quantum dots was built up. InGaAs quantum dots have been investigated with resonant laser spectroscopy at temperatures between 4.2 k and 250 mK. The quantum dots were embedded in a field effect structure consisting of a top gate and a back contact. The optical response of single quantum dot states has been measured in electric and magnetic fields.

One major goal in quantum dot research is to use single quantum dots that have a lifetime-limited linewidth in the sub-μeV regime [21, 16]. For quite some time the usual linewidths had been around $2\,\mu eV$ [15]. Spectral fluctuations of the quantum dot resonance caused by charging events in the vicinity of the quantum dot have been made responsible for this [85, 86, 109]. If a charging events occurs at a site which is close to the quantum dot the change in electric field induces a shift in the resonance energy of the quantum dot. Houel et al. has studied these jumps and concluded that the charging sites reside at the interface between GaAs and a superlattice separated from the quantum dots by 10 - 20 nm in conventional field effect structures [21]. The solid-state matrix surrounding a quantum dot consists of GaAs which can have different impurity atoms [41]. In chapter 6 a capacitor model is developed which simulates the change of electric field due to charging. From our model we find distances between impurity and quantum dot which clearly contradict the findings of Houel et al. [21]. From our calculations we concluded that charging of bulk impurities are responsible for the observed features. The model allowed also to obtain a 3D picture of how quantum dots and impurities

are positioned relative to each other. The high sensitivity for electric fields makes possible to utilize a quantum dot as a sensor for charges [26]. One application could be to design a hybrid system consisting of a self-assembled quantum dot and an electrostatically defined quantum dot. In electrostatically defined quantum dots the charging state is usually measured by means of a quantum point contact [110]. However the back-action between the quantum point contact and the quantum dot gives rise to a perturbation of the quantum dot system. As interaction between the exciton dipole in a self-assembled quantum dot and the charge in the electrostatically defined quantum dot is considerably smaller this would offer a more efficient method to measure charging states.

In the samples which are typically used for quantum dot experiments a Fermi sea of electrons acts as a back contact and therefore is close to the quantum dots. Electron tunneling through the barrier can mediate a coupling between a localized state in the quantum dot and the continuum of states in the back contact. Recently many-body signatures in optical transitions of self-assembled quantum dots have been discussed [36, 94]. If a localized spin state of the quantum dot acts as a local scattering potential for the spin reservoir in the back contact the Kondo effect would govern the optical signal [36, 37]. Kondo correlations have been found in 2011 [35] and confirm the theoretical predictions. Another many-body effect is the Fermi edge singularity [94] which is known from quantum wells [34]. In our experiments a quantum dot with a weak coupling between quantum dot and Fermi sea had been investigated. Close to the tunneling regime the originally isolated quantum dot state transforms in a superposition state between the continuum and the quantum dot. This effect manifests experimentally in an energy renormalization (i.e. an energy shift of the optical resonance of the quantum dot). This had been shown in photoluminescence on a negatively charged exciton by Dalgarno et al. [30]. As the quantum dot investigated in chapter 5 is weakly tunnel-coupled to the reservoir the hybridization signature is small and the photoluminescence does not have sufficient resolution to observe the effect. In this work the first investigation of the hybridization effect on the neutral and charged exciton by means of resonant laser spectroscopy is presented. This technique offers a considerably higher spectral resolution and therefore allows to measure the coupling strength with improved accuracy compared to photoluminescence. The coupling strength is an important parameter for many-body effects in quantum dots as it defines in which coupling regime system is. It also turns out that the energy shifts for the neutral and the charged exciton are opposite to each other which can be understood by a comparison of the level diagrams. The hybridization effect is the high temperature analogue of the Fermi edge singularity as at 4.2 K any many-body effect is masked by thermal fluctuations. Therefore the goal would be now to cool down this quantum dot sample down to mK-temperatures to check the theoretical predictions [94]. Most recently Haupt et al. has demonstrated optical signatures of the Fermi edge singularity in combination with a Fano interference on a sample with strong coupling [33].

The charged exciton in quantum dots is a two-level system which splits up into

a four-level system with well-defined spin states in magnetic fields [28, 29]. In chapter 7 this property was exploited to measure the electron bath temperature of the sample. Excitations of $|\uparrow\rangle$ and $|\downarrow\rangle$ are possible. If $|\uparrow\rangle$ is addressed the absorption contrast increases with magnetic field and in case of $|\downarrow\rangle$ it decreases [111]. This behavior in the Pauli-blockade regime reflects the occupation of the electron (ground) states which are determined by the transition rates between the electron and exciton states. The spin-flip between the electron states is mediated by cotunneling. The optical Bloch equations for the system have been derived to model the absorption contrast as a function of magnetic field for different temperatures. By fitting the results to the experimental data the temperature of the electron bath could be deduced. A temperature of $380 \pm 53\,\mathrm{mK}$ at a nominal base temperature of $250\,\mathrm{mK}$ was found. This is a very useful tool to determine temperatures for quantum dot samples. Especially for the observation of many-body effects this technique is very convenient as it operates down to mK.

Bibliography

[1] Arakawa, Y. and Sakaki, H. *Appl. Phys. Lett.* **40**(11), 939–941 (1982).

[2] Leonard, D., Krishnamurthy, M., Reaves, C. M., Denbaars, S. P., and Petroff, P. M. *Appl. Phys. Lett.* **63**(23), 3203–3205 (1993).

[3] Drexler, H., Leonard, D., Hansen, W., Kotthaus, J. P., and Petroff, P. M. *Phys. Rev. Lett.* **73**(16), 2252–2255 Oct (1994).

[4] Garcia, J. M., Medeiros-Ribeiro, G., Schmidt, K., Ngo, T., Feng, J. L., Lorke, A., Kotthaus, J., and Petroff, P. M. *Appl. Phys. Lett.* **71**(14), 2014–2016 (1997).

[5] Jöns, K. D., Atkinson, P., Müller, M., Heldmaier, M., Ulrich, S. M., Schmidt, O. G., and Michler, P. *Nano Lett.* **13**(1), 126–130 (2013).

[6] Kirstaedter, N., Ledentsov, N., Grundmann, M., Bimberg, D., Ustinov, V., Ruvimov, S., Maximov, M., Kop'ev, P., Alferov, Z., Richter, U., Werner, P., Gosele, U., and Heydenreich, J. *Electronics Letters* **30**(17), 1416–1417 (1994).

[7] Bimberg, D., Kirstaedter, N., Ledentsov, N., Alferov, Z. I., Kop'ev, P. S., and Ustinov, V. *Selected Topics in Quantum Electronics, IEEE Journal of* **3**(2), 196–205 (1997).

[8] Vallaitis, T., Koos, C., Bonk, R., Freude, W., Laemmlin, M., Meuer, C., Bimberg, D., and Leuthold, J. *Opt. Express* **16**(1), 170–178 Jan (2008).

[9] Michler, P., Kiraz, A., Becher, C., Schoenfeld, W. V., Petroff, P. M., Zhang, L., Hu, E., and Imamoğlu, A. *Science* **290**, 2282–2285 December (2000).

[10] Yuan, Z., Kardynal, B. E., Stevenson, R. M., Shields, A. J., Lobo, C. J., Cooper, K., Beattie, N. S., Ritchie, D. A., and Pepper, M. *Science* **295**(5552), 102–105 (2002).

[11] Bimberg, D. and Pohl, U. W. *Materials Today* **14**, 388 (2011).

[12] Martin, G., Mitonneau, A., and Mircea, A. *Electronics Letters* **13**(7), 191–193 (1977).

[13] Kaminska, M., Weber, E., Liliental?Weber, Z., Leon, R., and Rek, Z. *Journal of Vacuum Science Technology B: Microelectronics and Nanometer Structures* **7**(4), 710–713 (1989).

[14] Miller, R. C., Gossard, A. C., Tsang, W. T., and Munteanu, O. *Phys. Rev. B* **25**, 3871–3877 Mar (1982).

[15] Hoegele, A., Seidl, S., Kroner, M., Karrai, K., Warburton, R. J., Gerardot, B. D., and Petroff, P. M. *Phys. Rev. Lett.* **93**, 217401 Nov (2004).

[16] Vamivakas, A. N., Lu, C.-Y., Matthiesen, C., Zhao, Y., Falt, S., Badolato, A., and Atature, M. *Nature* **467**(7313), 297–300 September (2010).

[17] Sallen, G., Tribu, A., Aichele, T., Andre, R., Besombes, L., Bougerol, C., Richard, M., Tatarenko, S., Kheng, K., and Poizat, J.-P. *Nature Photon.* **4**(10), 696–699 October (2010).

[18] Nirmal, M., Dabbousi, B. O., Bawendi, M. G., Macklin, J. J., Trautman, J. K., Harris, T. D., and Brus, L. E. *Nature* **383**(6603), 802–804 October (1996).

[19] Vamivakas, A. N., Zhao, Y., Lu, C.-Y., and Atatüre, M. *Nature Phys.* **5**, 925–+ December (2009).

[20] Latta, C., Högele, A., Zhao, Y., Vamivakas, A. N., Maletinsky, P., Kroner, M., Dreiser, J., Carusotto, I., Badolato, A., Schuh, D., Wegscheider, W., Atature, M., and Imamoglu, A. *Nature Phys.* **5**, 758–763 October (2009).

[21] Houel, J., Kuhlmann, A. V., Greuter, L., Xue, F., Poggio, M., Gerardot, B. D., Dalgarno, P. A., Badolato, A., Petroff, P. M., Ludwig, A., Reuter, D., Wieck, A. D., and Warburton, R. J. *Phys. Rev. Lett.* **108**, 107401 Mar (2012).

[22] Berthelot, A., Favero, I., Cassabois, G., Voisin, C., Delalande, C., Roussignol, P., Ferreira, R., and Gérard, J. M. *Nature Phys.* **2**, 759–764 November (2006).

[23] Atature, M., Dreiser, J., Badolato, A., Hogele, A., Karrai, K., and Imamoglu, A. *Science* **312**(5773), 551–553 (2006).

[24] Hanson, R. and Awschalom, D. D. *Nature* **453**(7198), 1043–1049 June (2008).

[25] Berezovsky, J., Mikkelsen, M. H., Stoltz, N. G., Coldren, L. A., and Awschalom, D. D. *Science* **320**, 349– April (2008).

[26] Vamivakas, A. N., Zhao, Y., Fält, S., Badolato, A., Taylor, J. M., and Atatüre, M. *Phys. Rev. Lett.* **107**, 166802 Oct (2011).

[27] Robledo, L., Elzerman, J., Jundt, G., Atatüre, M., Högele, A., Fält, S., and Imamoglu, A. *Science* **320**(5877), 772–775 (2008).

[28] Dreiser, J., Atatüre, M., Galland, C., Müller, T., Badolato, A., and Imamoglu, A. *Phys. Rev. B* **77**(7), 075317 Feb (2008).

[29] Kroner, M., Weiss, K. M., Biedermann, B., Seidl, S., Holleitner, A. W., Badolato, A., Petroff, P. M., Öhberg, P., Warburton, R. J., and Karrai, K. *Phys. Rev. B* **78**(7), 075429 Aug (2008).

[30] Dalgarno, P. A., Ediger, M., Gerardot, B. D., Smith, J. M., Seidl, S., Kroner, M., Karrai, K., Petroff, P. M., Govorov, A. O., and Warburton, R. J. *Phys. Rev. Lett.* **100**(17), 176801 Apr (2008).

[31] Kleemans, N. A. J. M., van Bree, J., Govorov, A. O., Keizer, J. G., Hamhuis, G. J., Nötzel, R., Silov, A. Y., and Koenraad, P. M. *Nature Phys.* **6**, 534–538 July (2010).

[32] Kondo, J. *Progress of Theoretical Physics* **32**, 37–49 July (1964).

[33] Haupt, F., Smolka, S., Hanl, M., Wüster, W., Miguel-Sanchez, J., Weichselbaum, A., von Delft, J., and Imamoglu, A. *ArXiv e-prints* April (2013).

[34] Skolnick, M. S., Rorison, J. M., Nash, K. J., Mowbray, D. J., Tapster, P. R., Bass, S. J., and Pitt, A. D. *Phys. Rev. Lett.* **58**, 2130–2133 May (1987).

[35] Latta, C., Haupt, F., Hanl, M., Weichselbaum, A., Claassen, M., Wuester, W., Fallahi, P., Faelt, S., Glazman, L., von Delft, J., Tureci, H. E., and Imamoglu, A. *Nature* **474**(7353), 627–630 June (2011).

[36] Tureci, H. E., Hanl, M., Claassen, M., Weichselbaum, A., Hecht, T., Braunecker, B., Govorov, A., Glazman, L., Imamoglu, A., and von Delft, J. *Phys. Rev. Lett.* **106**(10), 107402 March (2011).

[37] Govorov, A. O., Karrai, K., and Warburton, R. J. *Phys. Rev. B* **67**(24), 241307 Jun (2003).

[38] Kloper, V., Osovsky, R., Kolny-Olesiak, J., Sashchiuk, A., and Lifshitz, E. *J. Phys. Chem. C* **111**(28), 10336–10341 (2007).

[39] Petroff, P. and DenBaars, S. *Superlattices Microstruct.* **15**(1), 15 – (1994).

[40] Bauer, E. *Zeitschrift fur Kristallographie* **110**, 372–394 January (1958).

[41] Sze, S. M. *Physics of Semiconductor Devices*. John Wiley & Sons, (1981).

[42] Leonard, D., Pond, K., and Petroff, P. M. *Phys. Rev. B* **50**, 11687–11692 Oct (1994).

[43] Offermans, P., Koenraad, P. M., Wolter, J. H., Granados, D., García, J. M., Fomin, V. M., Gladilin, V. N., and Devreese, J. T. *Appl. Phys. Lett.* **87**(13), 131902 (2005).

[44] Warburton, R. J., Schäflein, C., Haft, D., Bickel, F., Lorke, A., Karrai, K., Garcia, J. M., Schoenfeld, W., and Petroff, P. M. *Nature* **405**, 926–929 June (2000).

[45] Warburton, R. J., Schulhauser, C., Haft, D., Schäflein, C., Karrai, K., Garcia, J. M., Schoenfeld, W., and Petroff, P. M. *Phys. Rev. B* **65**, 113303 Feb (2002).

[46] Schulhauser, C. *Elektronische Quantenpunktzustände induziert durch Photonemission*. PhD thesis, Ludwig-Maximilians-Universität München, (2004).

[47] Warburton, R. J., Miller, B. T., Dürr, C. S., Bödefeld, C., Karrai, K., Kotthaus, J. P., Medeiros-Ribeiro, G., Petroff, P. M., and Huant, S. *Phys. Rev. B* **58**, 16221–16231 (1998).

[48] Raymond, S., Fafard, S., Poole, P. J., Wojs, A., Hawrylak, P., Charbonneau, S., Leonard, D., Leon, R., Petroff, P. M., and Merz, J. L. *Phys. Rev. B* **54**, 11548–11554 Oct (1996).

[49] Bayer, M., Stern, O., Hawrylak, P., Fafard, S., and Forchel, A. *Nature* **405**, 923–926 June (2000).

[50] Singh, J. *Semiconductor Optoelectronics*. McGraw-Hill, (1995).

[51] Bulaev, D. V. and Loss, D. *Phys. Rev. Lett.* **98**, 097202 Feb (2007).

[52] Bayer, M., Kuther, A., Forchel, A., Gorbunov, A., Timofeev, V. B., Schäfer, F., Reithmaier, J. P., Reinecke, T. L., and Walck, S. N. *Phys. Rev. Lett.* **82**, 1748–1751 Feb (1999).

[53] Hoegele, A., Alen, B., Bickel, F., Warburton, R. J., Petroff, P. M., and Karrai, K. *Physica E* **21**(2-4), 175 – 179 (2004). Proceedings of the Eleventh International Conference on Modulated Semiconductor Structures.

[54] Seidl, S., Gerardot, B. D., Dalgarno, P. A., Kowalik, K., Holleitner, A. W., Petroff, P. M., Karrai, K., and Warburton, R. J. *Physica E* **40**, 2153–2155 April (2008).

[55] Urbaszek, B., Warburton, R. J., Karrai, K., Gerardot, B. D., Petroff, P. M., and Garcia, J. M. *Phys. Rev. Lett.* **90**, 247403 Jun (2003).

[56] Bayer, M., Ortner, G., Stern, O., Kuther, A., Gorbunov, A. A., Forchel, A., Hawrylak, P., Fafard, S., Hinzer, K., Reinecke, T. L., Walck, S. N., Reithmaier, J. P., Klopf, F., and Schäfer, F. *Phys. Rev. B* **65**, 195315 May (2002).

[57] Schulhauser, C., Haft, D., Warburton, R. J., Karrai, K., Govorov, A. O., Kalameitsev, A. V., Chaplik, A., Schoenfeld, W., Garcia, J. M., and Petroff, P. M. *Phys. Rev. B* **66**, 193303 Nov (2002).

[58] Schinner, G. J., Repp, J., Schubert, E., Rai, A. K., Reuter, D., Wieck, A. D., Govorov, A. O., Holleitner, A. W., and Kotthaus, J. P. *ArXiv e-prints* November (2011).

[59] Alen, B., Bickel, F., Karrai, K., Warburton, R. J., and Petroff, P. M. *Appl. Phys. Lett.* **83**(11), 2235–2237 (2003).

[60] Demtröder, W. *Experimentalphysik 2: Elektrizität und Optik*. Springer-Verlag, (1999).

[61] Minsky, M. *Scanning* **10**, 128 (1987).

[62] Yariv, A. *Quantum Electronics*. John Wiley & Sons, (1989).

[63] Kasap, S. O. *Optoelectronics and Photonics*. Prentice Hall, (2001).

[64] Hecht, E. *Optik*. Oldenbourg, (2001).

[65] Kroner, M. *Resonant photon-exciton interaction in semiconductor quantum dots*. PhD thesis, Ludwig-Maximilians-Universität München, (2008).

[66] Hoegele, A., Seidl, S., Kroner, M., Karrai, K., Schulhauser, C., Sqalli, O., Scrimgeour, J., and Warburton, R. J. *Rev. Sci. Inst.* **79**(2), 023709 (2008).

[67] Seidl, S. *Resonant interband transmission spectroscopy on single charge-tunable quantum dots*. PhD thesis, Ludwig-Maximilians-Universität München, (2007).

[68] Meyer, C., Sqalli, O., Lorenz, H., and Karrai, K. *Rev. Sci. Inst.* **76**(6), 063706 (2005).

[69] Balshaw, N. H. Technical report, Oxford Instruments Ltd., (2001).

[70] Kroner, M., Weiss, K. M., Seidl, S., Warburton, R. J., Badolato, A., Petroff, P. M., and Karrai, K. *Phys. Stat. Sol.* **246**(4), 795–798 (2009).

[71] Maletinsky, P. *Polarization and manipulation of a mesoscopic nuclear spin ensemble using a single confined electron spin*. PhD thesis, Swiss Federal Institute of Technology Zurich, (2008).

[72] Miller, B. T., Hansen, W., Manus, S., Luyken, R. J., Lorke, A., Kotthaus, J. P., Huant, S., Medeiros-Ribeiro, G., and Petroff, P. M. *Phys. Rev. B* **56**(11), 6764–6769 Sep (1997).

[73] Fricke, M., Lorke, A., Kotthaus, J. P., Medeiros-Ribeiro, G., and Petroff, P. M. *Europhys. Lett.* **36**(3), 197 (1996).

[74] Marzin, J. Y., Gérard, J. M., Izraël, A., Barrier, D., and Bastard, G. *Phys. Rev. Lett.* **73**, 716–719 Aug (1994).

[75] Trumm, S., Wesseli, M., Krenner, H. J., Schuh, D., Bichler, M., Finley, J. J., and Betz, M. *Appl. Phys. Lett.* **87**(15), 153113 (2005).

[76] Kroner, M., Lux, C., Seidl, S., Holleitner, A. W., Karrai, K., Badolato, A., Petroff, P. M., and Warburton, R. J. *Appl. Phys. Lett.* **92**(3), 031108 (2008).

[77] Xu, X., Sun, B., Berman, P. R., Steel, D. G., Bracker, A. S., Gammon, D., and Sham, L. J. *Science* **317**(5840), 929–932 (2007).

[78] Karrai, K. and Warburton, R. J. *Superlattices Microstruct.* **33**(5-6), 311 – 337 (2003). Special issue dedicated to Professor Jorg Kotthaus on the occasion of his 60th Birthday, 29th May 2004.

[79] Seidl, S., Kroner, M., Dalgarno, P. A., Högele, A., Smith, J. M., Ediger, M., Gerardot, B. D., Garcia, J. M., Petroff, P. M., Karrai, K., and Warburton, R. J. *Phys. Rev. B* **72**(19), 195339 Nov (2005).

[80] Loudon, R. *The Quantum Theory of Light.* Oxford University Press, (2006).

[81] Kroner, M., Rémi, S., Högele, A., Seidl, S., Holleitner, A., Warburton, R., Gerardot, B., Petroff, P., and Karrai, K. *Physica E* **40**(6), 1994 – 1996 (2008). 13th International Conference on Modulated Semiconductor Structures.

[82] Dalgarno, P. A., Smith, J. M., McFarlane, J., Gerardot, B. D., Karrai, K., Badolato, A., Petroff, P. M., and Warburton, R. J. *Phys. Rev. B* **77**, 245311 Jun (2008).

[83] Fox, M. *Quantum Optics: An introduction.* Oxford University Press, (2007).

[84] Xu, X., Yao, W., Sun, B., Steel, D. G., Bracker, A. S., Gammon, D., and Sham, L. J. *Nature* **459**, 1105 – 1109 (2009).

[85] Bak, W., Noh, H., Stambaugh, C., Arakawa, Y., and Jhe, W. *Appl. Phys. Lett.* **100**(2), 022105 (2012).

[86] Robinson, H. D. and Goldberg, B. B. *Phys. Rev. B* **61**, R5086–R5089 Feb (2000).

[87] Kleemans, N. A. J. M., Bominaar-Silkens, I. M. A., Fomin, V. M., Gladilin, V. N., Granados, D., Taboada, A. G., García, J. M., Offermans, P., Zeitler, U., Christianen, P. C. M., Maan, J. C., Devreese, J. T., and Koenraad, P. M. *Phys. Rev. Lett.* **99**(14), 146808 (2007).

[88] Maletinsky, P., Badolato, A., and Imamoglu, A. *Phys. Rev. Lett.* **99**(5), 056804 (2007).

[89] Krummheuer, B., Axt, V. M., and Kuhn, T. *Phys. Rev. B* **65**, 195313 May (2002).

[90] Schrieffer, J. R. and Wolff, P. A. *Phys. Rev.* **149**, 491–492 Sep (1966).

[91] Taylor, P. L. and Heinonen, O. *A Quantum Approach to Condensed Matter Physics.* Cambridge University Press, (2002).

[92] Kroner, M., Govorov, A. O., Remi, S., Biedermann, B., Seidl, S., Badolato, A., Petroff, P. M., Zhang, W., Barbour, R., Gerardot, B. D., Warburton, R. J., and Karrai, K. *Nature* **451**, 311–314 (2008).

[93] Davies, J. D. *The Physics of Low-Dimensional Semiconductors*. Cambridge University Press, (1998).

[94] Heyl, M. and Kehrein, S. *Phys. Rev. B* **85**, 155413 Apr (2012).

[95] Press, D., Ladd, T., Zhang, B., and Yamamoto, Y. *Nature* **456**, 218 March (2008).

[96] Gammon, D., Efros, A. L., Kennedy, T. A., Rosen, M., Katzer, D. S., Park, D., Brown, S. W., Korenev, V. L., and Merkulov, I. A. *Phys. Rev. Lett.* **86**, 5176–5179 May (2001).

[97] Urbaszek, B., Marie, X., Amand, T., Krebs, O., Voisin, P., Maletinsky, P., Hogele, A., and Imamoglu, A. *ArXiv e-prints* **1202.4637** February (2012).

[98] Gerardot, B., Brunner, D., Dalgarno, P., Ohberg, P., Seidl, S., Kroner, M., Karrai, K., Stoltz, N. G., Petroff, P. M., and Warburton, R. J. *Nature* **451**, 441–444 (2008).

[99] Mandel, L. and Wolf, E. *Optical Coherence and Quantum Optics*. Cambridge University Press, (1995).

[100] Khaetskii, A. V. and Nazarov, Y. V. *Phys. Rev. B* **61**, 12639–12642 May (2000).

[101] Smith, J. M., Dalgarno, P. A., Warburton, R. J., Govorov, A. O., Karrai, K., Gerardot, B. D., and Petroff, P. M. *Phys. Rev. Lett.* **94**(19), 197402 May (2005).

[102] Overhauser, A. W. *Phys. Rev.* **92**, 411–415 October (1953).

[103] Fallahi, P., Yilmaz, S. T., and Imamoglu, A. *Phys. Rev. Lett.* **105**, 257402 Dec (2010).

[104] Chekhovich, E. A., Krysa, A. B., Skolnick, M. S., and Tartakovskii, A. I. *Phys. Rev. Lett.* **106**, 027402 Jan (2011).

[105] Khaetskii, A. V. and Nazarov, Y. V. *Phys. Rev. B* **64**, 125316 Sep (2001).

[106] Kroutvar, M., Ducommun, Y., Heiss, D., Bichler, M., Schuh, D., Abstreiter, G., and Finley, J. J. *Nature* **432**, 81–84 November (2004).

[107] Calarco, T., Datta, A., Fedichev, P., Pazy, E., and Zoller, P. *Phys. Rev. A* **68**, 012310 Jul (2003).

[108] Demtröder, W. *Experimentalphysik 1: Mechanik und Wärme*. Springer-Verlag, (2004).

[109] Rice, J. H., Robinson, J. W., Jarjour, A., Taylor, R. A., Oliver, R. A., Briggs, G. A. D., Kappers, M. J., and Humphreys, C. J. *Appl. Phys. Lett.* **84**(20), 4110–4112 (2004).

[110] Elzerman, J. M., Hanson, R., Willems van Beveren, L. H., Witkamp, B., Vandersypen, L. M. K., and Kouwenhoven, L. P. *Nature* **430**(6998), 431–435 July (2004).

[111] Hoegele, A., Kroner, M., Seidl, S., Karrai, K., Atatüre, M., Dreiser, J., Imamoğlu, A., Warburton, R. J., Badolato, A., Gerardot, B. D., and Petroff, P. M. *Appl. Phys. Lett.* **86**(22), 221905 (2005).

Danksagung

Abschließend möchte ich noch denjenigen danken, die zum Gelingen dieser Arbeit beigetragen und mich während der letzten Jahre begleitet haben:

- Prof. Alex Högele danke ich für die Möglichkeit in seiner Gruppe das Quantenpunktexperiment aufbauen zu können. Ich durfte mit viel Freiheit spannende Experimente durchführen. Außerdem danke ich für die gute Betreuung sowie die Diskussionen und Denkanstöße, die zu einem besseren Verständnis der Messergebnisse beigetragen haben.
- Prof. Jörg Kotthaus danke ich für die tolle Atmosphäre an seinem Lehrstuhl und dass er bei Fragen immer gerne mit Rat zur Seite stand.
- Meinem Masterstudenten und Nachfolger Matthias Hauck danke ich für die hervorragende Zusammenarbeit und das Korrigieren meiner Arbeit.
- Max Freiermuth hat seine Bachelorarbeit und Praktikum bei uns gemacht. Danke für die lustigen und ergebnissreichen Mess-Sessions und das *ein* oder andere Bier.
- I thank Sasha Govorov for his theory for the hybridization effect, all the discussions, his advices and for introducing me to the Pizza Bismarck.
- Georg Schinner und Enrico Schubert für den Aufbau beziehungsweise ihre Unterstützung mit dem Helium-3 System.
- Meinen Bürokollegen Darren Southworth, Sebastian Stapfner, Jan Glückert, Onur Basirir und Andre Neumann für die gute Atmosphäre und die interessanten Diskussionen.
- Martina Jüttner, Bert Lorenz, Anton Heindl und Wolfgang Kurpas, ohne die der Lehrstuhl nicht annähernd so reibungsfrei funktionieren würde, danke ich ebenfalls.
- Der "'Reinraum-Crew"' Philipp Altpeter und Reinhold Rath danke ich dafür, dass der Reinraum perfekt funktioniert und bei Fragen und Problemen kann man immer auf sie zählen.

- Stephan Manus danke ich für die Elektronikunterstützung.
- Den "üblichen Verdächtigen" Jens Repp, Gunnar Petersen, Darren Southworth, Thomas Faust, Johannes Rieger und Matthias Hofmann, die immer gerne dabei waren, wenn es darum ging eine gute Zeit zu haben.
- Der Spezies "Homo sapiens MENSArii", die jeden Mittag pünktlich zwischen 11:45 und 11:50 abmarschiert. Ich habe euch nur selten betrogen!
- Ich danke unserem Fußballteam; war immer ein schöne Ausgleich.
- Meinen Eltern danke ich für die stete Unterstützung in allem was ich tue.
- Karin Rosenits Danke, dass du immer für mich da warst, dass du mich auch manchmal gedrängt und motiviert hast und dass du Verständnis hattest, wenn ich mal wieder im Labor oder zum Schreiben verschwunden bin.

Schee war's, g'lacht hama, guad is ganga!
Nein! Doch!